3-16-2018

A Study of the Hexakis Icosahedron Vacuum Lighter Than Air Vehicle and the Effects of Air Evacuation on the Structural Integrity

Anthony A. Castello

A STUDY OF THE HEXAKIS ICOSAHEDRON VACUUM LIGHTER THAN AIR VEHICLE AND THE EFFECTS OF AIR EVACUATION ON THE STRUCTURAL INTEGRITY

THESIS

Anthony A. Castello, Captain, USAF

AFIT-ENY-MS-18-M-246

DEPARTMENT OF THE AIR FORCE
AIR UNIVERSITY

AIR FORCE INSTITUTE OF TECHNOLOGY

Wright-Patterson Air Force Base, Ohio

AFIT-ENY-MS-18-M-246

A STUDY OF THE HEXAKIS ICOSAHEDRON VACUUM LIGHTER THAN AIR VEHICLE AND THE EFFECTS OF AIR EVACUATION ON THE STRUCTURAL INTEGRITY

THESIS

Presented to the Faculty

Department of Aeronautical Engineering

Graduate School of Engineering and Management

Air Force Institute of Technology

Air University

Air Education and Training Command

in Partial Fulfillment of the Requirements for the

Degree of Master of Science in Aeronautical Engineering

Anthony A. Castello, B.S. M.E. & M.S. BM.E.

Captain, USAF

March 16, 2018

AFIT-ENY-MS-18-M-246

A STUDY OF THE HEXAKIS ICOSAHEDRON VACUUM LIGHTER THAN AIR VEHICLE AND THE EFFECTS OF AIR EVACUATION ON THE STRUCTURAL INTEGRITY

Anthony A. Castello, B.S. M.E. & M.S. BM.E.
Captain, USAF

Committee Membership:

Dr. Anthony Palazotto, PhD
Chair

Dr. Jamie Tiley, PhD
Member

Dr. William Baker, PhD
Member

AFIT-ENY-MS-18-M-246

Abstract

The research this paper focuses on is comparing the structural differences between the icosahedron and hexakis icosahedron frame and skin for use as a vacuum lighter than air vehicle (VLTAV), analyzing the stress concentrations in the hexakis icosahedron both with and without the skin, and finding the optimal location and size of the air evacuation method for creating the internal vacuum. Previous research to date has identified dynamic loading on the structure and optimization of the structure, but this will be the first research to analyze the manufacturing of the structure through the development of the air evacuation design. Findings demonstrated that the hexakis icosahedron was significantly stiffer when compared to the icosahedron, and the W/B ratio of the hexakis icosahedron was smaller for the same structural and material characterizations. The hexakis-icosahedron came the closest to the yield stress of the material in the frame by its self, consisting of the Carbon Nano-Tube (CNT)/Bismaleimide (BMI) composite at 3.38 GPa, with the yield stress being 3.8 GPa. The near zero stress in the frame considering individual beams was found to lie at approximately 20% and 66% of the beam length. Placing small holes for air evacuation resulted in minimal stress changes for the entrance to the evacuation system, but created failure points at the positions of the structure where the exit to the air evacuation system was located. Adding material to the exit system solved the failure point and kept the stress levels below yielding. Further research into the geometry of the vertex revealed interactions between the 10 beams conjoining on a single location and led to the development of a second air evacuation design and analysis. Analyzing the simplified model of the air evacuation resulted in a maximum stress of 3.484 GPa, which again is below the yield limit of the material and gave the structure an overall

safety of factor of 1.09.

Acknowledgments

I would like to thank Dr. Palazotto, my thesis advisor, for his mentorship and help. He was continuously available to help me learn and apply various methods to my research. Without him this would not have been possible. I would also, like to thank the Air Force Office of Scientific Research (AFOSR) for their financial support. My parents for their advice and support during my childhood and academic career. Thank you to my beautiful wife for always motivating and pushing me to achieve more in my studies and personal life and for your unconditional love.

Anthony A. Castello

Table of Contents

Page

List of Figures

List of Tables

List of Acronyms

AFIT Air Force Institute of Technology

BCs Boundary Conditions

BMI Bismaleimide

CAD Computer Aided Drafting

CFD Computational Fluid Dynamics

CNT Carbon Nano-Tube

CNTs Carbon Nanotubes

COTS Commercial off the Shelf

DOF Degree of Freedom

FEA Finite Element Analysis

FEM Finite Element Model

ISR Intelligence, Surveillance, and Reconnaissance

LTAV Lighter Than Air Vehicle

LTAVs Lighter Than Air Vehicles

MUAVs Miniature Unmanned Aerial Vehicles

UAVs Unmanned Aerial Vehicles

VLTAV Vacuum Lighter Than Air Vehicle

W/B Weight-Buoyancy Ratio

List of Symbols

$\dot{\mathbf{m}}$	Mass Flow
λ	Eigenvalue or Lyapunov Value
μ	Viscosity
ρ	Density
$\mathbf{P_{cr}}$	Critical Load
$\mathbf{v_n}$	Velocity normal
A	Cross Sectional Area
a	Acceleration or Length of Pipe
D	Displacement Coordinates
E	Young's Modulus of Elasticity
F	Force
I	Moment of Inertia
k	Spring Stiffness Coefficient
L	Length or Loading per Unit Length
m	Mass or Volumetric Flow Rate
P	Pressure or Load
Re	Reynold's Number
R	Radius or Force Components
S	Surface Area
t	Time
U	Velocity or Displacement
u	Displacement
v	Velocity
w	Transverse Deflection of the Pipe
x	axial coordinate or unknown

A STUDY OF THE HEXAKIS ICOSAHEDRON VACUUM LIGHTER THAN AIR VEHICLE AND THE EFFECTS OF AIR EVACUATION ON THE STRUCTURAL INTEGRITY

I. Introduction

1.1 Chapter Overview

Lighter Than Air Vehicles (LTAVs) have been used throughout history, from 220 A.D. China as Zhuge Liang's military signal flairs, to 1852 with Henri Giffard's steam powered airship, to present day rigid and non rigid airships which have operated on the same principles since the beginning [12],[13]. While these LTAVs have propelled mankind into the aeronautical domain, they have several issues which have led to other research areas such as fixed wing and rotary aircraft. The Vacuum Lighter Than Air Vehicle (VLTAV) has the potential to address several of the issues with current LTAVs by utilizing Archimedes Principle with the absence of air instead of the traditional lifting gases.

This thesis looks at the hexakis icosahedron as a feasible VLTAV and the stresses undergone due to the pressure difference. Previous research has looked into the dynamic loading, and frequency modes of the structure, however this research focuses on developing an air evacuation system that can handle the static loads imposed by the pressure difference caused by the vacuum in an attempt to develop production methods of the hexakis icosahedron.

This chapter will investigate the background of LTAVs, the motivation for a VLTAV design, the objectives of the current research, and the generalized methodology

used to meet the objectives.

1.2 Background

Mankind has had their eyes on flight even since 43 B.C.-18 A.D. with Ovid's story of Daedalus and Icarus, but LTAVs were not recorded until 220 A.D. with Zhuge Liang's military signal flairs [12]. It was not until the mid 17th century that Francesco Lana de Terzi measured the pressure at sea level and proposed the first credible Lighter Than Air Vehicle (LTAV) [14]. The first manned flight took place in 1783 with the Montgolfier brother's paper hot air balloon. During this time helium was also found and started being used in balloons. Both of these methods rely on the Archimedes' Principle, which dictates that buoyancy is created by the displaced volume of fluid weighing less than the fluid which it is in [15]. Figure 1.1 depicts the forces described by Archimedes' Principle that allows the hot air balloon to float by changing the density of the internal air with temperature, and the helium balloon to float by using an internal gas with a much smaller density than air.

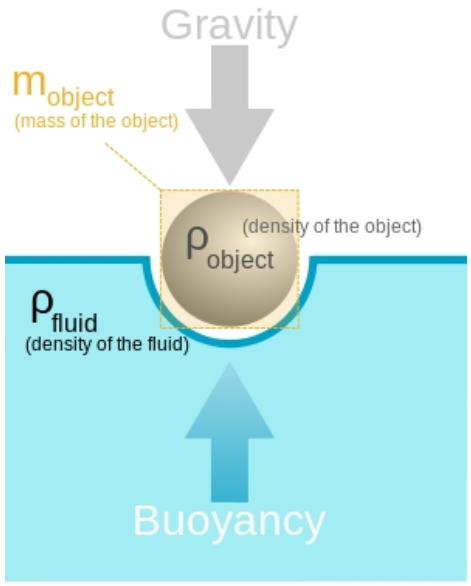

Figure 1.1. Buoyant forces on a LTAV [1]

The different methods for creating lift in a LTAV have their benefits and faults. Present day LTAV use the hot air technique or lighter than air gases to achieve lift. Hot air is a technique primarily used by smaller hot air balloons to change the density of the air on the inside of the balloon to be less than that of the colder air on the outside. This method is fairly easy to use due to the simple structure of the balloon and heater. The downsides to this method comes mainly with the limitations on the size of the balloon and the need for constant heating and fuel. The larger the payload the larger the balloon and heating supply will have to be. Typically hot air balloons will fly early in the morning when the outside temperature is colder in order to achieve the best lift possible.

Lighter than air gases, such as helium or hydrogen began being used in dirigibles or airships in order to steer the balloon. While hydrogen is the lightest lifting gas used, it is also extremely flammable and led to the end of airships with the Hindenburg's crash in 1937 [16]. Helium is the second lightest lifting gas with 92.7% buoyancy of hydrogen, and is non-flammable. While helium requires slightly more volume to achieve the same lift as hydrogen, it is also a lot more scarce.

The primary goal for a LTAV is to achieve a Weight-Buoyancy Ratio (W/B) of less than one. This will allow a LTAV to rise until its buoyant forces or W/B is greater than one. As altitude increases the density of the air gets smaller, eventually there will be a limit where the LTAV will no longer be lighter than air. This is the maximum operating condition based on the designed W/B [8].

The VLTAV was first described mathematically by Francesco Lana de Terzi in the mid 17th century. This concept included copper spheres in which the air was evacuated to create a vacuum. This model would have failed due to the compressive forces and the material suggested, however the idea of using a vacuum instead of a lighter than air gas is still plausible. The main problem has been creating a structure

that can withstand buckling caused by the compressive loads due to the vacuum. Akhmeteli and Gavrilin demonstrated that no material can be used in a sphere shape and withstand buckling due to the pressure caused by a vacuum [17]. A geometric structure would be needed to combat this issue of buckling, which led to T. Metlen's research at Air Force Institute of Technology (AFIT) on the icosahedron and hexakis icosahedron designs, and Cranston's work on the celestial design [2], [18], [19]. The designs in figure 1.2 represent Metlen and Cranston's work.

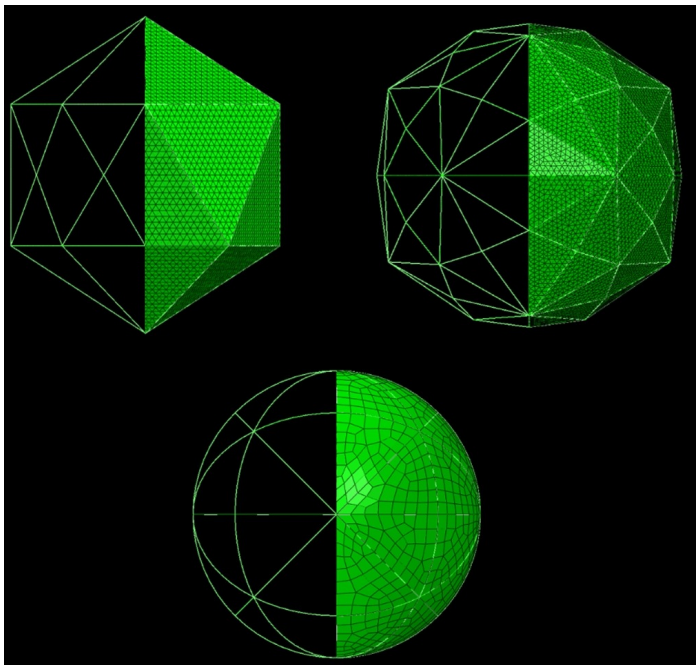

Figure 1.2. Icosahedron (top left), hexakis icosahedron (top right), celestial (bottom), (Frame-membrane half covered) [2]

The icosahedron design was created with 12 vertices and 20 equilateral triangles while the hexakis icosahedron design consisted of 62 vertices and 120 identical triangles. J. Schwemmer worked on optimizing the hexakis icosahedron to obtain a potential model with a W/B less than one that could survive the stresses induced by the pressure at sea level. His results showed that a four foot diameter hexakis icosahedron, with a Carbon Nano-Tube (CNT)/Bismaleimide (BMI) composite frame, and a thin membrane made of graphene could potentially survive and float at sea-level

with a 200g payload [9].

1.3 Motivation

Unmanned Aerial Vehicles (UAVs) have become the predominate surveillance tool for both military and civilian applications. The UAVs have given the military 24 hour surveillance with aircraft that can stay aloft for 32+ hours at a time [20]. The main issue that arises is the cost of flight due to personnel, fuel, maintenance, and logistics. These types of UAVs are also limited to locations that have acceptable runways. Urban surveillance is another domain that is limited with typical UAVs. This has led to the need and development of smaller scale UAVs or Miniature Unmanned Aerial Vehicles (MUAVs). These are portable UAVs that can be carried in a backpack, deployed, and operated by a single person. While LTAVs could produce longer endurance times, weigh less, and make less noise than other types of common UAVs using electric or gas engines, the LTAVs using lifting gases such as helium are prone to leaking and still require fuel. This requires extra stores of gas on board to maintain lift, and also require storage/transportation of the gas. A VLTAV has the potential to stay aloft almost indefinitely. Relying only on the electronic vacuum pump used to remove the air, which can be kept running with solar panels. This would eliminate the need for any type of fuel, be extremely light weight and compact, and allow for constant surveillance with weather being the only or major issue with operation.

Previous research has looked at the dynamic analysis of the hexakis icosahedron and optimization of the hexakis design [8],[9] as well as analyses of the icosahedron design, which has higher overall stresses. There has not been an in-depth analysis of the stresses and deformations of the optimized hexakis icosahedron, and the potential impacts of the air evacuation on the VLTAV. Evacuating the air will require a vacuum pump which is designed to suck air at a constant mass flow rate and pump it out the

other end. Chaotic behavior in the frame has been seen when applying a load rate on the hexakis icosahedron at 4 $MPa * s^{-}1$, which is the limiting factor for evacuating the air [6],[8].

1.4 Objective

Previous research at AFIT has focused on the icosahedron, and the dynamic responses of a one-foot diameter hexakis icosahedron. The focus of this research is to analyze the hexakis icosahedron with the parameters found by J. Schwemmer in his research on the optimization of the hexakis icosahedron, and analyze the stresses caused by the air evacuation to ensure the feasibility of the design. Specifically, the objectives being investigated are:

- To compare the icosahedron identified by R. Adorno-Rodriquez to an equivalent hexakis icosahedron.
- Model a 1.2192 m (4 ft) diameter hexakis icosahedron in Finite Element Analysis (FEA) software with beam, skin, and material properties found by J. Schwemmer.
- Identify and characterize the non-linear stresses imposed quasi-statically on the hexakis icosahedron at sea level with out the skin.
- Identify and characterize non-linear stresses imposed quasi-statically on the hexakis icosahedron at sea level with the thin membrane skin.
- Analyze the stresses at the joints and mid-length of beam near supports.
- Determine the structural integrity of the hexakis icosahedron with the air evacuation method.

1.5 Methodology

Two 1.2192 m (4 ft) diameter hexakis icosahedron models were created in Abaqus FEA software [21]. The first model consisted only of the frame with no skin attached. This was created for two reasons. The frame by its self contains many of the details necessary for the air evacuation system, but the frame also can be studied by its self to determine whether or not the frame is strong enough to support the membrane without any unnecessary displacement. The second model consisted of the frame and thin membrane skin attached. The models were analyzed in Abaqus to determine the stress fields of the model under sea level conditions, looking at the joints and mid-beams specifically for potential failure points to identify the optimal location of the air evacuation system.

Long hand calculations were utilized to identify the mass flow rate, velocity, and pressure head in order to identify the system's air flow due to the air evacuation system. The limiting factor in evacuating the air was to avoid velocities that would produce chaotic behavior or collapse of the pipe. Luke Just found in his research at AFIT that the icosahedron began depicting chaotic behavior at a load rate of about 4 MPa/s [6]. This was verified by Jordan Snyder in his research for the hexakis icosahedron as well [8].

In order to analyze the air evacuation system, a simplified or reduced model had to be created in order to accurately depict the effects of the 3 dimensional system on the hexakis. The main models are produced using wire beams, and are given a profile, however when modeling the air evacuation which utilizes exhaust holes in the pipes, a 3 dimensional model was needed. The simplified model consisted of a single beam or multiple beams under similar loading conditions to give an accurate representation of the system on the overall model. This allowed for relatively quick computation of whether or not an air evacuation system would cause the model to fail or survive the

loading conditions.

1.6 Overview

- Chapter I: Thesis overview, background, motivation, objective, and high level methodology
- Chapter II: Theory and previous research on the hexakis-icosahedron
- Chapter III: Detailed methodology, including FEA and reduced model creation.
- Chapter IV: Finite Element Model (FEM) and computational results.
- Chapter V: Results summary, conclusion, and future research needed.

II. Background

2.1 Chapter Overview

Quasi static loading is the typical method for analyzing structures. This method requires the load to be applied very slowly as to not create any dynamic forces. Increasing the load rate will create dynamic forces and require a dynamic analysis instead of a static analysis. Evacuating the air from the hexakis icosahedron will cause dynamic loading, however the dynamic response can be mitigated by keeping the load rate less than 4 MPa/s [6], [8].Previous research at Air Force Institute of Technology (AFIT) by Cranston, Snyder, and Schwemmer have looked at the hexakis icosahedron and identified its structural capabilities, material properties, and chaotic behavior, which will be used as a frame work for this thesis and the study of the optimized hexakis icosahedron with structural modifications for air evacuation and potential manufacturing capabilities.

Chapter II will give the background and results of previous research on the hexakis icosahedron Vacuum Lighter Than Air Vehicle (VLTAV) design, and give a basic understanding of the fundamental principles required in the analysis of the air evacuation effects on the structural integrity, specifically the basic concepts of Finite Element Analysis (FEA), fluid dynamics, including conservation of mass and basic mass flow equations, as well as flow through an orifice.

2.2 Fluid Dynamics

In fluid dynamics, where aerodynamics is a sub discipline, there are two governing equations that need to be understood in order to properly analyze the air evacuation of the hexakis icosahedron. The first deals with the conservation of mass, while the second deals with the conservation of momentum. There is a third law that deals with

the conservation of energy, and while it is important as a law, it does not specifically need to be explained for this research. These three laws are the fundamental principles of fluid and aerodynamics. These laws give a set of equations which were used in analyzing the load rate on the system, and the velocity impact of the exhaust which can be seen in figure 2.1.

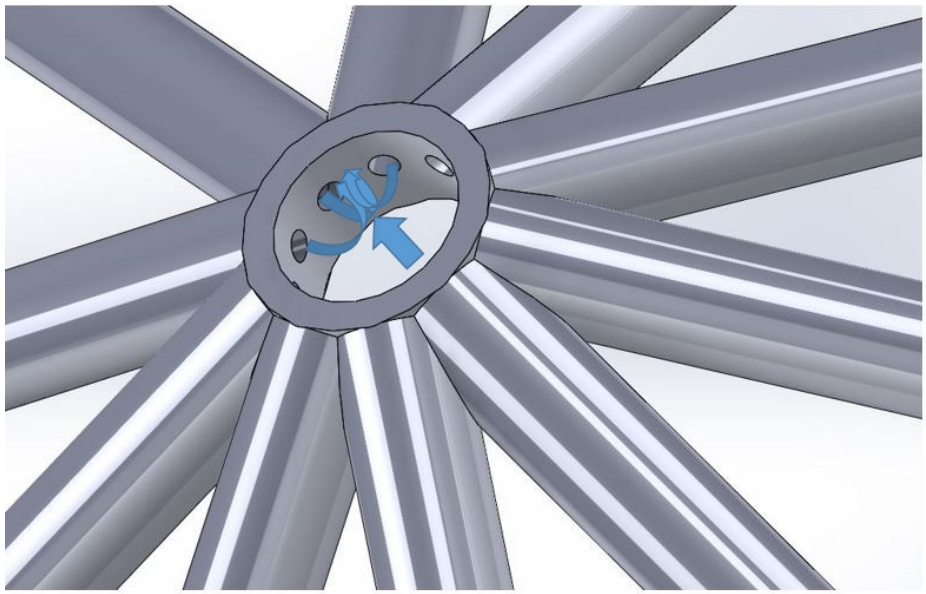

Figure 2.1. Air flow through the vertex of the hexakis icosahedron.

2.2.1 Governing Equations

The continuity equation, also known as the conservation of mass utilizes the concept of mass flow. Through this equation, the mass flow of the fluid is related to the density of the fluid, ρ, the velocity of the fluid normal to the cross sectional area, V_n, and the area the fluid is passing through, A. The definition of mass flow through A is the mass passing through A per second as shown in equation (2.1). Equation (2.1) can be rewritten in the form of equation (2.2). Using the mass flow equation and applying the principle of conservation of mass, a relation can be created between two points in a finite control volume.

Physical principle: Mass can be neither created nor destroyed [22].

This means that the net mass flow, ($\dot{m}$), out of control volume through surface S is equal to the time rate of mass inside control volume V [22]. With this relation, one can set the in flow and out flow equal to each other as shown in equation (2.3).

$$\dot{m} = \frac{\rho V_n dt A}{dt} \tag{2.1}$$

$$\dot{m} = \rho(V_n)A \tag{2.2}$$

$$\rho V_n dS = \rho V \cdot dS \tag{2.3}$$

Using equation (2.3) and modifying it for the net mass flow out of the entire control surface, one obtains the final form of the continuity equation shown in equation (2.4). If we limit the system to steady flow, which means that the density does not change for a fixed point, equation (2.4) can simplify to equation (2.5).

$$\frac{\partial}{\partial t}\int_V \rho dV + \int_S \rho V \cdot dS = 0 \tag{2.4}$$

$$\int_S \rho V \cdot dS = 0 \tag{2.5}$$

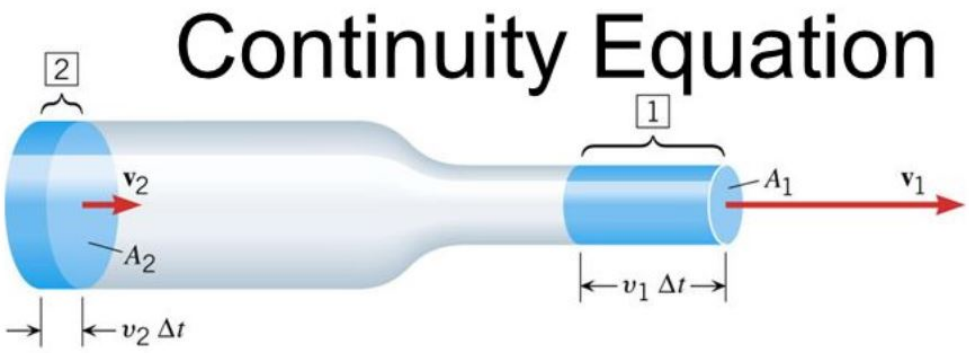

Figure 2.2. Visualization of the continuity equation [3].

The next governing equation of concern is the momentum equation. This equation is based on Newton's second law.

Physical principle: Force = time rate of change of momentum [22]

This law states that the force, F, is a body of mass, m, times the acceleration, a, equation (2.6).

$$F = ma \tag{2.6}$$

Solving both sides of the equation for steady and non-viscous flow, which is a common assumption for an ideal fluid having zero viscosity, one obtains equation (2.7)

$$\int_S (\rho V \cdot dS)V = -\int_S p dS \tag{2.7}$$

This equation can be represented in differential form as well by the Euler equations for non-viscous flow or by the Navier-Stokes equations for viscous flow.

2.2.2 Flow

There are many different characteristics flow can have that greatly change the calculations needed or the results obtained. To simplify most aerodynamic problems, the flow is assumed to be steady, non-viscous, and laminar. Applying this assumption removes the dependence on time and simplifies most of the equations needed. To maintain laminar flow, it is generally accepted that the Reynolds number needs to be below 2300 or 2040 as found by Avila for pipe flow [23]. The Reynolds number can be found using equation (2.8) where ρ is the density of the fluid, V is the velocity of the fluid, L is the characteristic linear dimension, and μ is the viscosity of the fluid. It is a dimensionless quantity used to predict the flow characteristics in fluid mechanics.

$$Re = \frac{\rho V L}{\mu} \tag{2.8}$$

Turbulent flow is drastically different than laminar flow in that it consists of chaotic changes in pressure and velocity, which requires different variances of the previously mentioned fluid dynamic equations. The flow through the air evacuation system will be analyzed at a worst case scenario, but realistically would be kept low enough to avoid turbulent flow during evacuation.

2.3 Finite Element Analysis (FEA)

Abaqus, the FEA software uses implicit integration to solve the linear equation (2.9). By assigning a stiffness matrix and the forces acting on the structure, the displacements can be calculated and from there the stresses, strains, and many other useful characteristics. The stiffness matrix, K, will change depending on what type of element is being used to simulate the model [24]. There is a plethora of elements that can be utilized for any scenario, from a 1 Degree of Freedom (DOF) all the way

to a 6 DOF structure. Figure 2.3 gives an example of an FEA analysis.

$$\{R\} = \{K\}\{D\} \tag{2.9}$$

where,

$\mathbf{R}$ = Force Components

$\mathbf{K}$ = Global Stiffness Matrix

$\mathbf{D}$ = Displacement Components

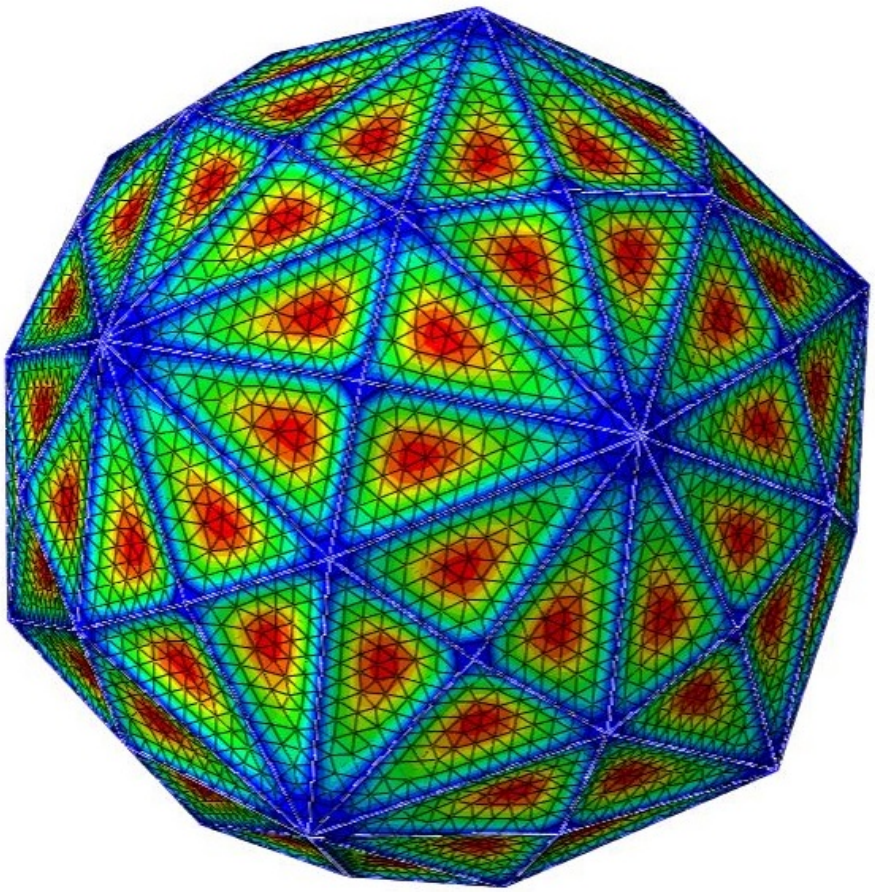

Figure 2.3. FEA example of a structure under quasi static loading [4].

In FEA there is a distinction between linear and non-linear systems. The linear system is solved with equation (2.9) for the system independent of time as the stiffness matrix and load vector are known. The non-linear system can be solved using

the Newton-Raphson technique. This technique takes into consideration that the displacement changes with each iteration, requiring a new stiffness matrix and load vector calculation before the next iteration. An example of this is given by Cook, with a simple non-linear spring using the spring stiffness coefficient, k, displacement, u, and load, P shown in equation (2.10).

$$ku = P \tag{2.10}$$

The spring starts with an initial displacement $u_0 = 0$, spring stiffness coefficient k_1, and a pressure P_1 being applied. From here, Δu is calculated for the current displacement increment and used to update the solution, u_1. Following equations (2.11) to (2.13), u_A gives the current estimate of the desired result u_1.

$$k_0 \Delta u = \Delta P_1 \tag{2.11}$$

$$\Delta u = k_0^{-1} \Delta P_1 \tag{2.12}$$

$$\Delta u_A = 0 + \Delta u \tag{2.13}$$

The displacement estimate is not exact due to the force error. This is a result of the spring force not being in equilibrium with the load P_1. To account for this load error, the term $\boldsymbol{e}_{PA}$ is introduced.

$$e_{PA} = P_1 - ku_A \tag{2.14}$$

where ku_A is the resisting force provided by the structure in its current deformation state [24]. Steps are taking iteratively until the imbalance becomes zero.

2.4 Mechanical Systems Behavior

Mechanical systems including structures and structural elements are subject to being either stable or unstable. This is dependent on the structures geometry which, defines its capability to withstand loading. Buckling is a common failure mode of many structures due to the load and shape of the object. Collapse is another failure mode which is also dependent on geometry, but at the global level. It all comes down to the structures stiffness, which is dependent on the materials and geometry used for the structure. The loading characteristics can play a vital role as well for geometries that may be stable in one axis with an axial loading, but unstable with a biaxial or loading in a different axis the geometry cannot handle.

2.4.1 Instability and Buckling

Buckling is a form of instability where the object undergoes a large displacement when subjected to a perturbation, and cannot regain its original state of equilibrium. A simple example of this is shown by a fixed column subjected to a load. The load is applied at the top of the column which is away from the centroid causing a moment. As the load is applied and the moment is formed, the elastic forces innate to the stiffness of the column will counteract the load and moment to maintain equilibrium. Gradually increasing the load will generate a larger moment until the stiffness of the column can no longer maintain the stability, at which point buckling occurs. This load is referred to as the critical load and can be calculated with equation (2.15) [25]. Saada shows that the critical load for buckling is approached as the numerical value of $KL/2$ approaches $\pi/2$, where $K^2 = P/EI_3$. This can be checked by simply taking the values from one of the beams in chapter IV and plugging into the equation for K.

Chapter IV will cover the buckling analysis.

$$P_{cr} = \frac{\pi^2 EI}{4L^2} \tag{2.15}$$

where,

$\mathbf{P_{cr}}$ = Critical Load

$\mathbf{E}$ = Young's Modulus

$\mathbf{I}$ = Moment of Inertia

$\mathbf{L}$ = Column Length

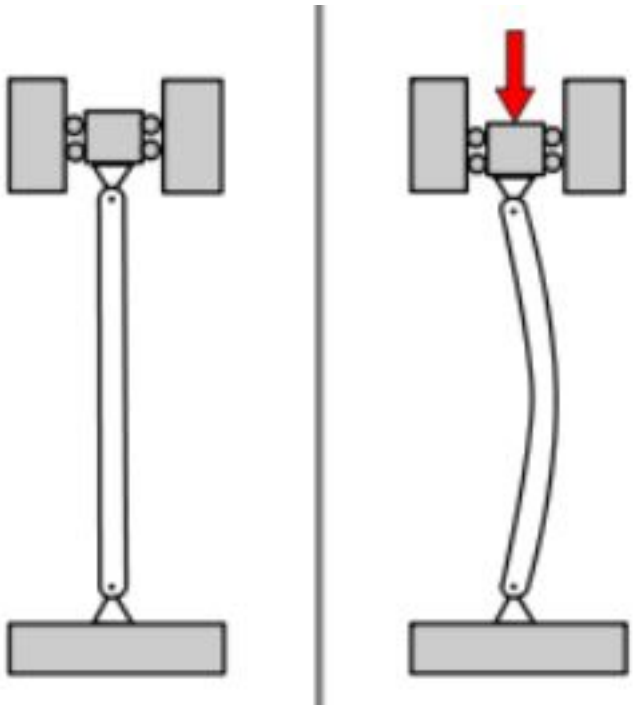

Figure 2.4. Fixed column subjected to a load and buckling

During buckling, the stiffness of the structure changes resulting in a nonlinear response. This phase is known as post-buckling and continues until the structure can no longer carry a load, which is considered the collapse point. Dowell proposed another method for identifying buckling, but in the case of a pipe under fluid flow. This is shown by Dowell where he derives equation (2.22) through the correlation and

development of equations (2.16) through (2.21) [26].

2.4.2 Dowell's derivation for fluid flow through a flexible pipe

The final form of Dowell's equation was developed through the aerodynamic loading per unit length of a pipe as shown in equation (2.16).The velocity of the fluid is related to the material properties and characteristics of the pipe in order to identify the point at which buckling will occur. This equation is useful to get a baseline velocity which would act as the maximum velocity the air could be evacuated. Utilizing any air evacuation method that reaches velocities close to this value would result in failure due to buckling. Chapter IV will go over this equation and its results with respect to the air flow through the hexakis icosahedron, but the development of the equation is shown below.

$$-L = \rho A[\frac{\partial}{\partial t} + U\frac{\partial}{\partial x}]^2 w = \rho A[\frac{\partial^2 w}{\partial t^2} + 2U\frac{\partial^2 w}{\partial x \partial t} + U^2\frac{\partial^2 w}{\partial x^2}] \tag{2.16}$$

where,

$\mathbf{L}$ = loading per unit length

$\mathbf{A} = \pi R^2$ open area for circular pipe

$\rho, \mathbf{U}$ = fluid density, axial velocity

$\mathbf{w}$ = transverse deflection of the pipe

$\mathbf{x}$ = axial coordinate

$\mathbf{t}$ = time

The equation of motion for the thin beam is:

$$EI\frac{\partial^4 w}{\partial x^4} + m_p\frac{\partial^2 w}{\partial t^2} = L \tag{2.17}$$

where,

$\mathbf{m_p} = \rho_p 2\pi Rh$ for thin hollow circular pipe of thickness h, per unit length

EI = beam bending stifness

There is a dynamic and static solution possible for this beam, however looking at the static portion of the equation, by dropping the time derivative, and by simply supporting the beam which sets $EI\frac{\partial^2 w}{\partial x^2} = 0$ at x = 0, and substituting equation (2.16) into (2.17), yields the following:

$$EI\frac{\partial^4 w}{\partial x^4} + \rho AU^2\frac{\partial^2 w}{\partial x^2} = 0 \tag{2.18}$$

Applying boundary conditions w = 0 at x = 0, and correlating the previous equation to the buckling equation of a beam under a compressive load, gives:

$$P = \rho U^2 A \tag{2.19}$$

Looking at the divergence dynamic pressure also known as the buckling pressure gives:

$$EIp^4 + \rho U^2 Ap^2 = 0 \tag{2.20}$$

The four roots associated with the characteristic equation can then be applied, with the first two essentially being zero. Therefore, the equation can be shown as:

$$\lambda^2 = (\frac{\rho U^2 A}{EI})a^2 \tag{2.21}$$

The smallest non trivial eigenvalue, which is $\lambda = \pi$, then leads to the final equa-

tion:

$$\rho * U^2 = \frac{E * I}{A * a^2} * \pi^2 \tag{2.22}$$

where,

U = Velocity of the fluid

E = Young's Modulus

I = Moment of Inertia

A = Cross sectional area of the pipe

a = Length of the pipe

λ is the ratio of aerodynamic to elastic stiffness and is a non-dimensional parameter. This equation now gives the buckling pressure also known as the divergence pressure for the beam with a give fluid flow.

2.5 Previous Research

2.5.1 Background

The VLTAV is not a new idea, with its conception back in 17th century with Francesco Lana de Terzi, however the concept has not actually been studied in detail until recent years. Metlen researched the structural solutions to the VLTAV, which led to the development of the icosahedron and the hexakis icosahedron as pictured in figure 1.2. His research mainly focused on the feasibility of the two internal frame structures, with an emphasis on the icosahedron. Metlen's findings demonstrated that the icosahedron frame due to its geodesic structure was capable using strong enough materials. His research also postulated that the hexakis icosahedron would work as well [18]. There have been 4 other AFIT students that have analyzed the icosahedron under static and dynamic loading. There were three AFIT students that analyzed

the hexakis icosahedron specifically under static and dynamic loading. The following subsections gives a brief overview of their research and the significant findings.

2.5.1.1 Nonlinear Structural Analysis Of An Icosahedron And Its Application To Lighter Than Air Vehicles Under A Vacuum

Adorno-Rodriguez conducted static analysis on the icosahedron frame, focusing on identifying the optimal beam size, skin thickness and material properties that could be used. Adorno-Rodriquez began by developing an equation to calculate the Weight-Buoyancy Ratio (W/B) ratio of the skin and frame as shown in equation (2.23) [5]. The W/B ratio is a critical parameter for studying the VLTAV, as it dictates whether or not the structure has enough buoyancy to float. The W/B ratio is essentially the weight of the structure, divided by the weight of the displaced fluid.

$$\frac{W}{B} = \frac{V_s\rho_s + V_f\rho_f + (V_i - V_r)\rho_{air,i}}{(V_i - V_r)\rho_{air,o}} \tag{2.23}$$

where,

$\mathbf{W}$ = weight of the structure

$\mathbf{B}$ = buoyancy of the structure

$\mathbf{V_s}$ = volume of the skin

$\rho_\mathbf{s}$ = density of the skin

$\mathbf{V_f}$ = volume of the frame

$\rho_\mathbf{f}$ = density of the frame

$\mathbf{V_i}$ = internal volume of the icosahedron before deformation

$\mathbf{V_r}$ = internal volume of the icosahedron after deformation

$\rho_{\mathbf{air,i}}$ = internal air density

$\rho_{\mathbf{air,o}}$ = external air density

From this equation, the frame and skin can be separated in order to calculate a separate W/B for each. This led to two equations for the optimal skin thickness and frame radius for a given icosahedron radius. These equations became very useful for optimizing the structure and for use in developing a set of equations for the hexakis icosahedron as well. Adorno-Rodriquez also looked into three potential materials that would maximize the strength of the structure while keeping the weight to a minimum. There were seven different combinations analyzed and the results are shown in figures 2.5 and 2.6. These models utilized Spectra, Beryllium, and Carbon Nanotubes (CNTs) in different combinations. The plots show the applied pressure versus the Von Mises stress for the different materials, where the horizontal solid lines show the positive buoyancy for the different materials and the dashed lines show the yield strength for each material. As the pressure applied was increased, the von Mises stress of the structure was recorded for the frame and skin respectively, and the point where the W/B ratio was equal to or less to one, as well as the max von Mises stress was less than the yield limit was recorded. Adorno-Rodriguez determined two models which showed the best results in terms of positive buoyancy and resistance to fracture. Models M3 and M7 consisted of Nanocyl NC7000 Thin Multi-wall CNTs, which are created by a Catalytic Chemical Vapor Deposition (CCVD) process, but have not matured enough for manufacturing purposes. Models M3 and M7 will be compared against the hexakis icosahedron to identify the main differences between the two structures.

Adorno-Rodriguez performed one other analysis of note for this research and that was on the Boundary Conditions (BCs) used in constraining the icosahedron for FEA [27]. Figure 2.7 depicts the locations of the BCs with figure 2.7-a or BC1, having the bottom node completely constrained meaning all 6 of theDOF were fixed and the top node was left free. BC2 shown in 2.7-b, had all 6 of the DOF in the bottom node

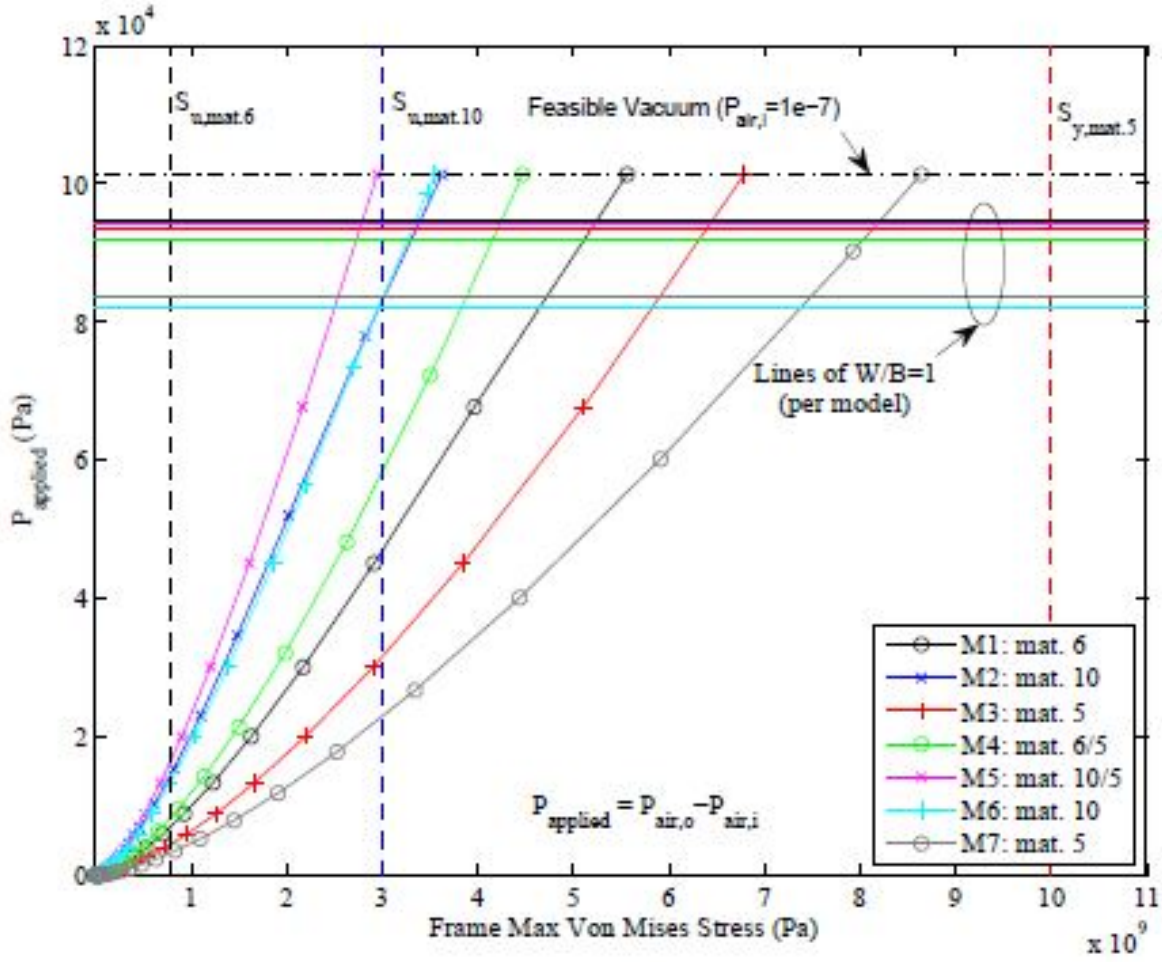

Figure 2.5. Icosahedron: Applied Pressure versus Frame Maximum von Mises Stress [5]

constrained and translational freedom in the 1 and 2 direction constrained. BC3 shown in 2.7-c, had symmetrical BCs with the translational DOF in the 1 and 2 directions constrained both in the top and bottom nodes.

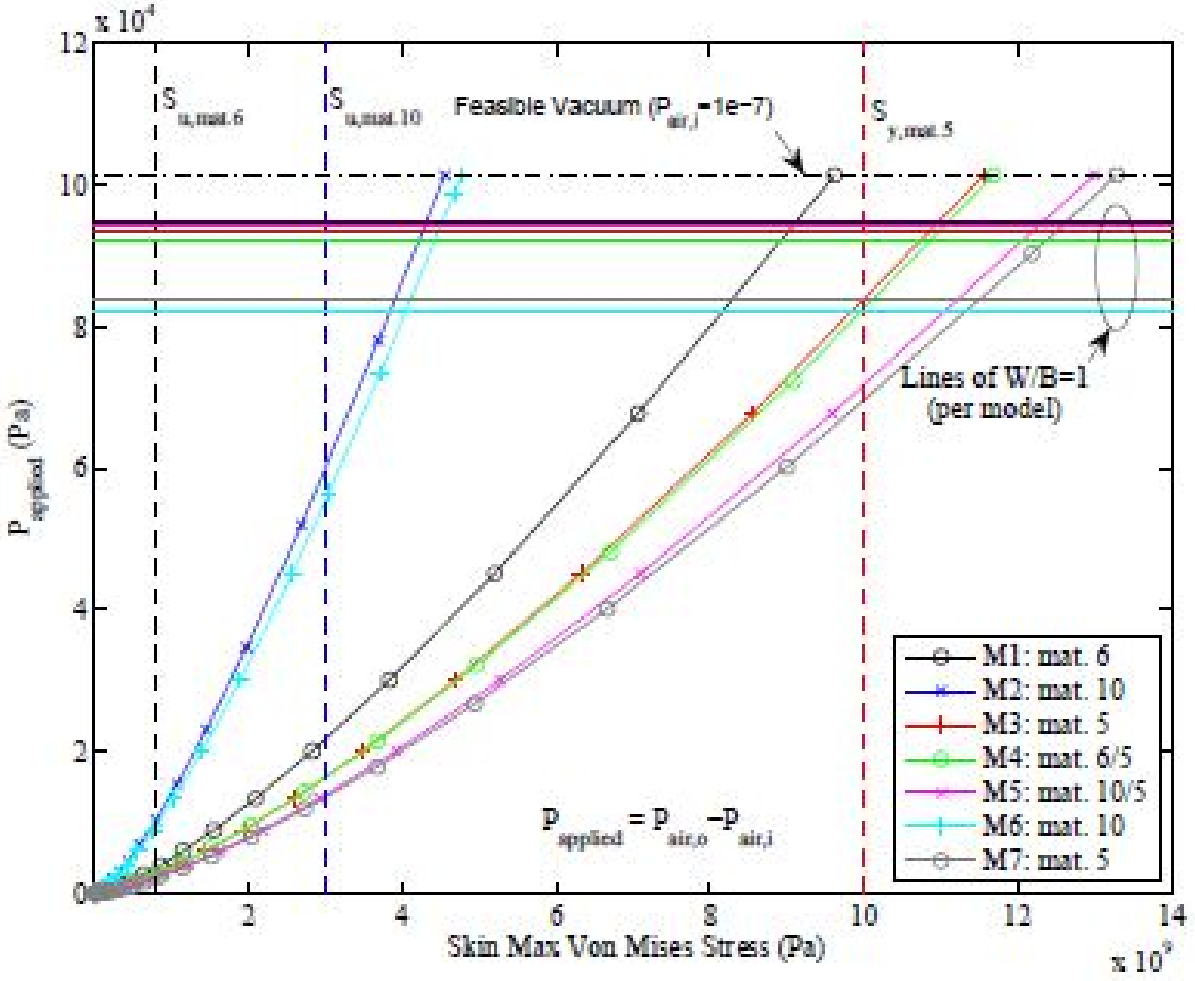

Figure 2.6. Icosahedron: Applied Pressure versus Skin Maximum von Mises Stress (with singularities) [5]

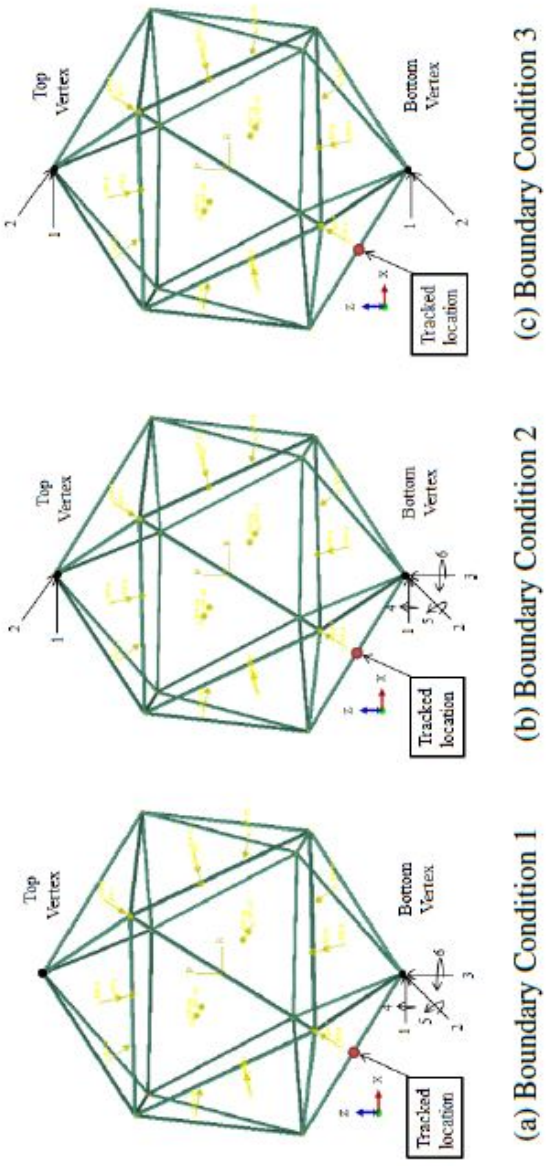

Figure 2.7. Icosahedron: Frame Boundary Conditions [5]

The BCs were analyzed by a non-linear analysis of the structure and looking at the deformations of the frame. The first BC showed non-symmetry significantly near the bottom vertex. BC 2, showed improved symmetry, but still remained non-symmetric near the bottom vertex. This indicated issues with constraining the bottom vertex from rotating. BC 3 showed symmetrical results for the entirety of the structure. This led to an analyses of the mid point on the edge near the bottom vertex by applying a load rate to the frame, probing a single location on the frame near the bottom vertex, and plotting the pressure versus displacement. The pressure versus displacement plots are shown in figure 2.8, where the pressure, in Pascals, is on the vertical axis and the deformation of the mid point near the vertex divided by the thickness of the beam is on the horizontal axis. These plots were done for all three BCs and showed an interesting phenomena called snapback behavior, occurring in BC1 and BC2 at 45% sea level pressure, while BC3 had no snapback behavior even at 100% sea level pressure. This is shown in the plots, as the deformation continues until it reaches a point at which it regains its deformation and then continues deforming again at the same load. This meant that the BCs had an impact on the symmetry and linearity of the model and when this symmetry was not met, chaotic behavior formed, which ultimately led to failure at much smaller load rates as shown by Just [6]. This led to further models utilizing BC3 to avoid running into any singularities during computation of the FEA. Two of the models in this research will be analyzed for the use of no BCs. The hexakis icosahedron is significantly more symmetrical, potentially alleviating the need for BCs. The other models will run BC3, in a similar manner to Ruben's, and the same plots for all the hexakis models will be generated to identify the pressure applied versus displacement for a given point along the edge of the model. These will be used to identify where non-linearity occurs and if there is any snapback behavior.

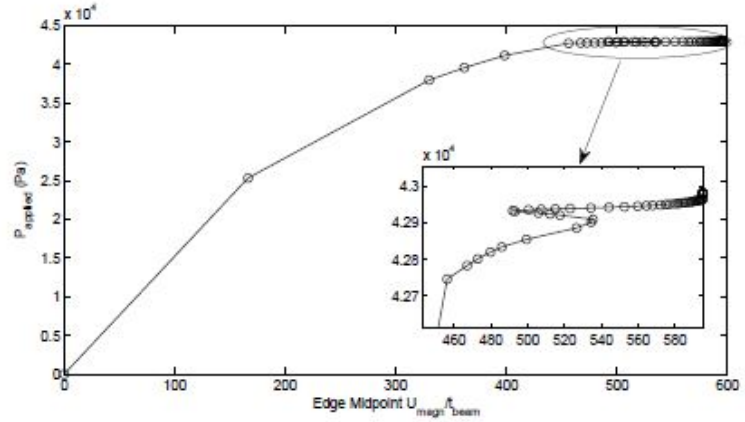

(a) Boundary Condition 1

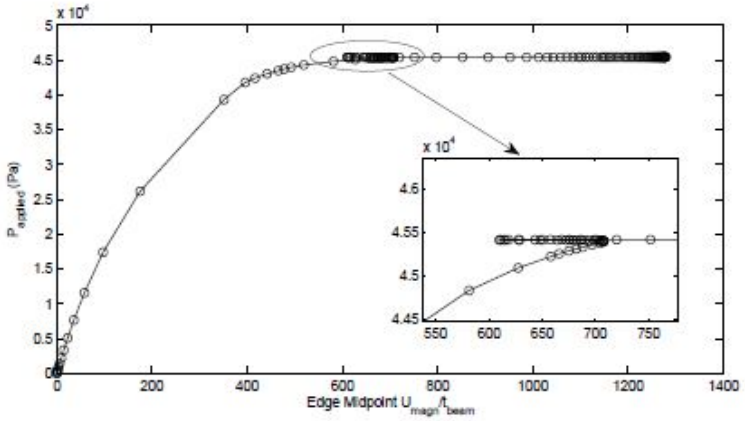

(b) Boundary Condition 2

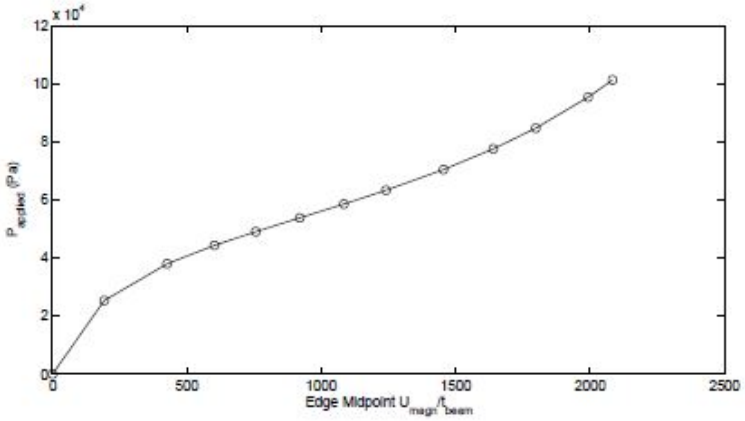

(c) Boundary Condition 3

Figure 2.8. Icosahedron: Frame Boundary Conditions Comparison - Edge Midpoint vs Equivalent Pressure [5]

2.5.1.2 Dynamic Response Analysis Of An Icosahedron Shaped Lighter Than Air Vehicle

Lucas Just took the icosahedron and performed a dynamic analysis, beginning with a quasi-static step and applying five different loads at varying ramp inputs [6], [28]. The main take away from Just's research was the load rates at which snapback occurs. Adorno-Rodriguez postulated that snapback would not occur with BC3 with the skin placed on the frame due to its symmetrical response. Just proved, with his research, that snapback occurred in the first two BCs with approximately 35% sea level pressure applied at a rate of 4.053 $MPa - s^{-}1$. Furthermore, the snapping load occurred around 45% sea level pressure for the quasi-statically applied load, only for BC1 and BC2 [28]. BC3 did not depict the snapback phenomena even at 100% sea level pressure, when the load was applied quasi-statically; however, it did show snapback behavior under dynamic loading. Furthermore, the structure did not present any snapback behavior what so ever, when the skin was applied. Figure 2.9 depicts the loads analyzed and the snapping load level as seen by the horizontal limit. Figure 2.10 shows the displacement versus time curves for the structure once the load exceeds the snapping load. This shows how the displacement grows wildly and dangerously for the structure. The worst case scenario of 4.053 $MPa - s^{-}1$ will be applied to this research during the air evacuation calculations in order to avoid snapback behavior, even though it was shown that this does not occur when the skin is applied. This will give the most conservative analysis.

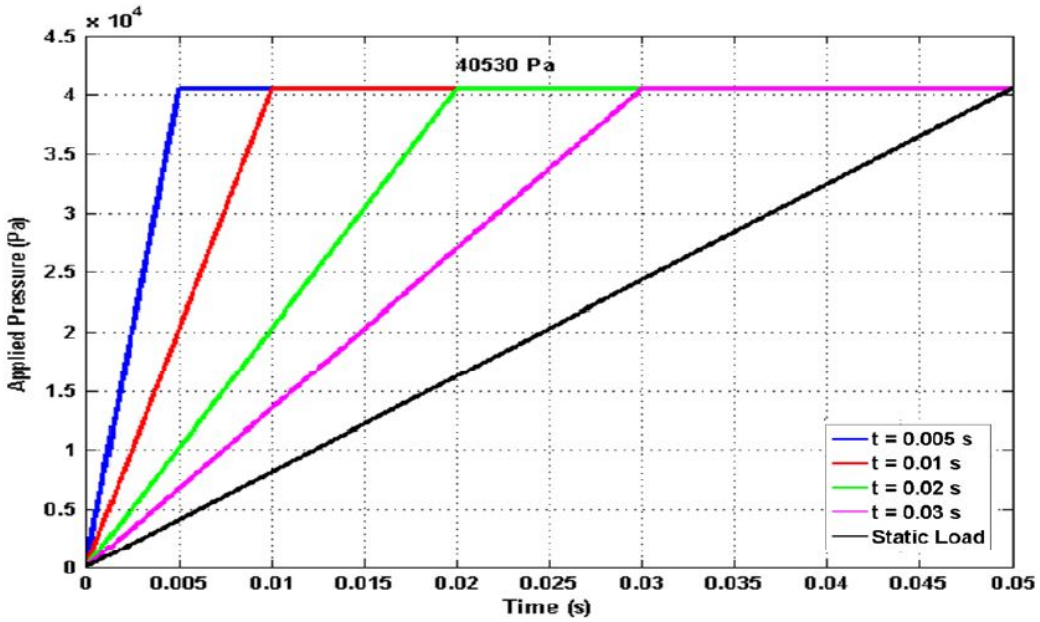

Figure 2.9. Icosahedron: Loads above snapping load [6]

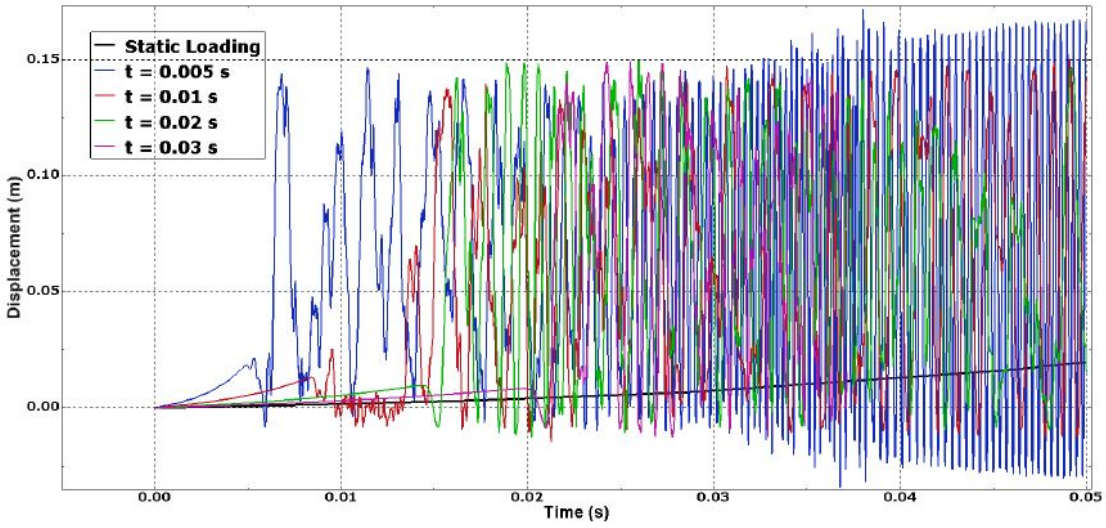

Figure 2.10. Icosahedron: Displacement versus Time Curves above Snapping Load [6]

2.5.2 Hexakis Icosahedron

2.5.2.1 Conceptual Design, Structural Analysis, and Design Space Exploration of a Vacuum Lighter than Air Vehicle

Brian Cranston's work contributed significantly to the model development of the hexakis icosahedron frame. The hexakis icosahedron is a geodesic polyhedron, which is made of 120 equivalent triangles approximating a sphere and based on the Catalan solid [29]. The Catalan solid is essentially a series of structures produced using face-transitive polytopes to generate a structure with a spherical composition. To be face-transitive, each of the individual faces must be the exact same. The vertex locations were calculated using the eight coordinate formulas and the 62 vertex combinations as shown in figures 2.11 and 2.12. These vertex locations were utilized in this research to create the air evacuation models and several of the Computer Aided Drafting (CAD) models.

$C_0 = \frac{r_{hex}\sqrt{\frac{5}{2}(85-31\sqrt{5})}}{22}$
$C_1 = \frac{r_{hex}\sqrt{\frac{5}{2}(25-11\sqrt{5})}}{3}$
$C_2 = \frac{r_{hex}\sqrt{5(25-2\sqrt{5})}}{22}$
$C_3 = r_{hex}\sqrt{\frac{1}{10}(5-\sqrt{5})}$
$C_4 = \frac{5r_{hex}}{3\sqrt{5+2\sqrt{5}}}$
$C_5 = \frac{r_{hex}\sqrt{\frac{5}{2}(65+19\sqrt{5})}}{22}$
$C_6 = r_{hex}\sqrt{\frac{1}{10}(5+\sqrt{5})}$
$C_7 = \frac{r_{hex}\sqrt{\frac{5}{2}(5-\sqrt{5})}}{3}$
$C_8 = \frac{r_{hex}\sqrt{5(25-2\sqrt{5})}}{11}$

Figure 2.11. Hexakis Icosahedron: Coordinate equations [7]

Hexakis Icosahedron Vertex Locations		
V0 = (0.0, 0.0, C8)	V20 = (-C3, 0.0, C6)	V41 = (C5, -C0, -C2)
V1 = (0.0, 0.0, -C8)	V21 = (-C3, 0.0, -C6)	V42 = (-C5, C0, C2)
V2 = (C8, 0.0, 0.0)	V22 = (C6, C3, 0.0)	V43 = (-C5, C0, -C2)
V3 = (-C8, 0.0, 0.0)	V23 = (C6, -C3, 0.0)	V44 = (-C5, -C0, C2)
V4 = (0.0, C8, 0.0)	V24 = (-C6, C3, 0.0)	V45 = (-C5, -C0, -C2)
V5 = (0.0, -C8, 0.0)	V25 = (-C6, -C3, 0.0)	V46 = (C2, C5, C0)
V6 = (0.0, C1, C7)	V26 = (0.0, C6, C3)	V47 = (C2, C5, -C0)
V7 = (0.0, C1, -C7)	V27 = (0.0, C6, -C3)	V48 = (C2, -C5, C0)
V8 = (0.0, -C1, C7)	V28 = (0.0, -C6, C3)	V49 = (C2, -C5, -C0)
V9 = (0.0, -C1, -C7)	V29 = (0.0, -C6, -C3)	V50 = (-C2, C5, C0)
V10 = (C7, 0.0, C1)	V30 = (C0, C2, C5)	V51 = (-C2, C5, -C0)
V11 = (C7, 0.0, -C1)	V31 = (C0, C2, -C5)	V52 = (-C2, -C5, C0)
V12 = (-C7, 0.0, C1)	V32 = (C0, -C2, C5)	V53 = (-C2, -C5, -C0)
V13 = (-C7, 0.0, -C1)	V33 = (C0, -C2, -C5)	V54 = (C4, C4, C4)
V14 = (C1, C7, 0.0)	V34 = (-C0, C2, C5)	V55 = (C4, C4, -C4)
V15 = (C1, -C7, 0.0)	V35 = (-C0, C2, -C5)	V56 = (C4, -C4, C4)
V16 = (-C1, C7, 0.0)	V36 = (-C0, -C2, C5)	V57 = (C4, -C4, -C4)
V17 = (-C1, -C7, 0.0)	V37 = (-C0, -C2, -C5)	V58 = (-C4, C4, C4)
V18 = (C3, 0.0, C6)	V38 = (C5, C0, C2)	V59 = (-C4, C4, -C4)
V19 = (C3, 0.0, -C6)	V39 = (C5, C0, -C2)	V60 = (-C4, -C4, C4)
	V40 = (C5, -C0, C2)	V61 = (-C4, -C4, -C4)

Figure 2.12. Hexakis Icosahedron: Vertex locations [7]

The vertex locations are only dependent on the desired radius of the frame, labeled r_{hex}. A MATLAB program was created to identify the vertex locations based on the desired radius, r_{hex} of the overall structure. These locations were used in this research to build several of the models, especially the air evacuation models and CAD models. With the vertex locations known, Cranston generated the lengths of the each triangular edge broken up by short (l_{se}), medium (l_{me}), and long edge (l_{le}). These lengths were calculated using equations (2.24a), (2.24b), and (2.24c).

$$l_{se} = r_{hex}\frac{5}{11} * \sqrt{49 - \frac{65\sqrt{5}}{3}} \tag{2.24a}$$

$$l_{me} = r_{hex}\frac{1}{11} * \sqrt{81 - 21\sqrt{5}} \tag{2.24b}$$

$$l_{le} = r_{hex}2 * \sqrt{\frac{7}{3} - \sqrt{5}} \tag{2.24c}$$

The internal volume and surface area could then be computed, equations (2.25a) through (2.25c), based on the triangle lengths and used to compute the ideal beam cross-section by applying equation (2.23).

$$p_{ht} = \frac{l_{se} + l_{me} + l_{le}}{2} \tag{2.25a}$$

$$A_{HI} = 120 * \sqrt{p_{ht}(p_{ht} - l_{se})(p_{ht} - l_{me})(p_{ht} - l_{le})} \tag{2.25b}$$

$$V_{HI} = \frac{100 r_{hex}^3}{3 * \sqrt{53 + \frac{118}{\sqrt{5}}}} \tag{2.25c}$$

where,

$\mathbf{p_{ht}}$ = Average beam length

$\mathbf{A_{HI}}$ = Surface area of hexakis icosahedron

$\mathbf{V_{HI}}$ = Internal volume of hexakis icosahedron

The beam cross section is a thin-walled pipe and optimized based off of the desired W/B of the frame, W/B_f, and skin, W/B_s. The W/B_f is the volume of the frame times the density of the material used for the frame, divided by the buoyancy of the structure, and W/B_s is the volume of the skin times the density of the material for the skin, divided by the buoyancy of the structure. This was done similar to Adorno-Rodriguez's method for the icosahedron and resulted in equations (2.26a)-(2.26c).

$$r_{beam} = r_{icos} * \sqrt{\frac{\frac{W}{B_f}\rho_a V_{hi}}{((\pi 60(2c - c^2))(l_{se} + l_{me} + l_{le}))\rho_f}} \tag{2.26a}$$

$$c = \frac{t_{beam}}{r_{beam}} \tag{2.26b}$$

$$t_{skin} = \frac{\rho_a \frac{W}{B_s} V_{HI}}{A_{HI}\rho_s} \tag{2.26c}$$

These equations were utilized in a MATLAB and python script that builds the hexakis icosahedron based on the desired radius of the frame and inputs the model into Abaqus for analysis.

2.5.2.2 A Study Of Quasi-Static and Dynamic Analyses of a Hexakis Icosahedron Frame for Use In a Vacuum Lighter-Than-Air Vehicle

Jordan Snyder compared the analysis from Lucas Just with the icosahedron to the hexakis icosahedron. He performed the Lyapunov exponent analysis to determine whether or not chaotic behavior was an issue. The results of the comparison are shown in table 2.1, where the more positive the Lyapunov value, the more chaotic the structure was. Snyder concluded two important differences. One was that the hexakis icosahedron was less susceptible to the effects of the BCs due to the symmetry of the structure, and the second conclusion was that the hexakis icosahedron was more

rigid. This led to smaller changes in the Lyapunov exponents than the icosahedron. While, most of the results in table 2.1 were positive, indicating chaotic behavior 2 of these values were not, indicating they were stable. Snyder verified the snapping load rate as identified in previous research by Adorno-Rodriguez and Just. It was in a similar range of 4-4.5 MPa/s for the frame, which is where this research will focus on avoiding when evacuating the air from the hexakis icosahedron. Snyder's research verified Just's in that the skin eliminates this snapback behavior [30].

Table 2.1. Icosahedron and Hexakis Icosahedron Lyapunov Analysis Results [8]

Load Case	Icosahedron	Hexakis	Load Rate (MPa/s)	BC
1	-0.0121	0.2552	5.0663	3
2	-0.0137	-0.0175	4.053	3
3	3.8814	0.6245	8.106	3
4	0.303	0.2341	5.0663	2
5	0.371	0.0143	4.053	2
6	19.67	4.767	8.106	2

The rest of Snyder's research focused on analyzing the stress fields of the hexakis icosahedron frame and skin models using Beryllium S-200 for the frame to see how the model held up with respect to the material being used. Figure 2.13 depicts one of the analyses and the results for reference, where you can see the von Mises stress being compared to the material properties to identify whether or not yield or failure occurred for each load rate. Snyder noticed that the actual load rate did not affect the maximum stress as much as the actual maximum load applied. The figure shown has lower stresses at 10% sea level with a higher load rate than another model that used a smaller load rate at 20% sea level pressure.

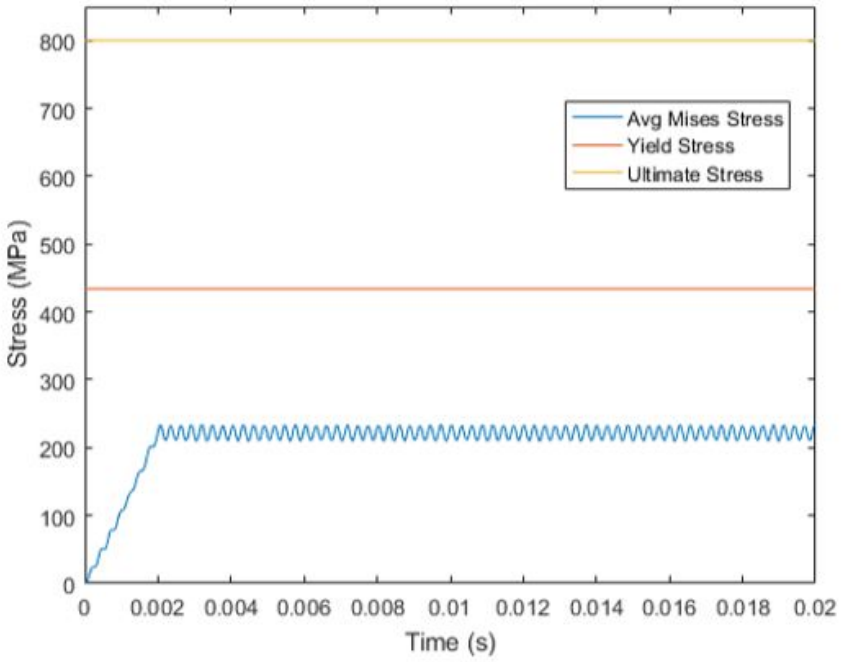

Figure 2.13. Hexakis Icosahedron: Mises stress results for load case 1 [8]

2.5.2.3 Optimal Design of a Hexakis Icosahedron Vacuum Based Lighter than Air Vehicle

Joseph Schwemmer verified Cranston's work and analyzed the hexakis icosahedron with a Carbon Nano-Tube (CNT) composite frame and a skin made of spectra [31]. Realizing the diameter needed to be very large for the structure to work, Schwemmer focused on optimizing the structure with different materials and different diameters in an attempt to reduce the size of the hexakis icosahedron. Taking the W/B as the key factor and holding the beam radius and skin thickness to manufacturing tolerances, the material densities needed for the varying diameters were computed at a W/B of 1 and 0.7. The results are summarized in table 2.2. Schwemmer concluded that it may be feasible to achieve a hexakis icosahedron with a W/B of approximately 0.7, using a CNT composite for the frame and graphene for the skin. Graphene is a very strong

and light weight material, which would allow the structure to survive the pressure at sea level with a 200g payload. Further research into the feasibility of the hexakis icosahedron with these characteristics will be studied for validation.

Table 2.2. Material Optimization Results [9]

Diameter (ft, m)	**Beam Radius (mm)**	**Beam Thickness (mm)**	**Skin Thickness (mm)**	**Density for W/B = 1** (kg/m^3)	**Density for W/B = 0.7** (kg/m^3)
1,0.3048	8	0.2	0.2	75	55
2,0.6096	8	0.2	0.2	225	165
5,1.524	12	0.3	0.2	620	430
10,3.048	25	0.5	0.2	880	620

2.6 Summary

Research performed by Metlen, Adorno-Rodriguez, and Just have identified the icosahedron as a possible VLTAV design, with important ground work in the model development and loading characteristics identified. Snyder compared the results of the icosahedron to that of the hexakis icosahedron with using Berllyium and identified several differences. Schwemmer used optimization algorithms with Cranston's code to identify the frame sizing and material needed for a W/B of approximately 0.7. This research will be used to further analyze the hexakis icosahedron as outlined by Schwemmer's research and identify methods for evacuating the air as to not create snapback or chaotic behavior as identified in Just's and Snyder's research. Chapter III will further discuss the model development and research methodology to achieve this analysis.

III. Research Methodology

3.1 Chapter Overview

The overall objective is to analyze the hexakis icosahedron under quasi static loading with the parameters identified in previous research and to develop an air evacuation design that can withstand sea level pressure. The model is not at the stage for actual construction and validation, therefore, the majority of the analysis for the hexakis icosahedron was done using Abaqus Finite Element Analysis (FEA) software [21]. This required an accurate Finite Element Model (FEM) to properly represent the structure and the frame. Snyder created a hexakis icosahedron model for both the frame by its self and the frame with the skin at one foot diameter [8]. The main focus of this thesis will be to analyze the hexakis icosahedron using the optimized parameters identified by Schwemmer; therefore, the models of the hexakis icosahedron will need to be remodeled to the dimensions specified by Schwemmer. Another model of the hexakis icosahedron was created using the MATLAB and Python scripts for continuity and model validation of previous research that utilized these scripts to develop the FEM. Finally, a FEM of the hexakis icosahedron with the air evacuation design needed to be created for an analysis of how the change in geometry handled the pressures undergone by the structure. By modeling the frame, the frame and skin, and the air evacuation design with a FEM, an analysis of the structure under different material properties, sizes, and loading conditions could give a conservative analysis of the overall structure and its behavior. A detailed discussion of the FEA methods, modeling techniques, and analysis process for the hexakis icosahedron structure are described in this chapter as well as the overall strategy for analyzing the hexakis icosahedron and air evacuation results.

The hexakis icosahedron model with the skin membrane was created using MAT-

LAB, Python, and Abaqus software based on work completed by Adorno-Rodriquez, Cranston, and Schwemmer. The scripts generated the model based on the desired radius of the structure and material properties, and then an analysis was done in Abaqus to see how the structure behaved under quasi static loading. The frame model of the hexakis icosahedron was based on Snyder's rework of the model and was used to study the behavior of the frame under similar quasi static loading. The air evacuation model was developed in Abaqus using the vertex locations from the re-worked model done for the frame.

3.2 Modeling and Design

There are three main different analyses taking place in this research. Each required slightly different modeling and design than the other. The first research goal compared the icosahedron results from Adorno-Rodriquez to the results of the hexakis icosahedron. The second analysis researched the hexakis icosahedron in more detail in terms of size, beam dimensions, Boundary Conditions (BCs), frame, skin, and FEM design. The last analysis focuses on designing an air evacuation method for the structure and testing it. The hexakis icosahedron was built the same between the first analysis and models III, IV, and V, and therefore, has been explained in the following section.

3.2.1 Models I-V

There were a total of five models created for analysis using a Carbon Nano-Tube (CNT) composite for the frame and graphene for the skin. Snyder's models were modified and compared against models that were generated by the MATLAB and Python scripts. The models are summarized in table 3.1. Models I and II were Snyder's original models with the material properties changed to the CNT composite

and graphene. Models III and V were generated with the MATLAB and Python scripts created by Adorno-Rodriguez and Cranston and shown in Appendix A. Model IV was based on Snyder's frame model, but scaled to a four foot diameter and modified to account for the pressure loads acting as concentrated loads, also known and shown later in this chapter as the reference point technique. The main models to be analyzed are models IV and V as these are the models that the air evacuation method will be applied to. The other models were created to verify the Weight-Buoyancy Ratio (W/B) of the structure at varying diameters, and to test model creation through the Abaqus CAE and the MATLAB scripts as well as BCs.

Table 3.1. Description of models I-V and their corresponding dimensions

Model	I	II	III	IV	V
Skin	None	Attached	Attached	None	Attached
BC	3	None	3	None	3
Diameter - ft (m)	1 (0.3048)	1 (0.3048)	1 (0.3048)	4 (1.2192)	4 (1.2192)
W/B	0.3389	NA	11.9286	0.7528	0.7654
r_{beam} (mm)	0.955	0.955	8	8	8
t_{beam} (mm)	0.0477	0.0477	0.2	0.2	0.2
t_{skin} (mm)	0.012216	0.012216	0.0005	0.0005	0.0005
Manufacturing Limit	No	No	Yes	Yes	Yes

Schwemmer used manufacturing limitations on his optimization equations which set the beam radius, beam thickness, and skin thickness to values different than those used in previous research. Schwemmer's manufacturing constraints have been tabulated in table 3.2. Typically the beam radius, beam thickness, and skin thickness would be calculated using equations (2.26a), (2.26b), and (2.26c) as was done for models I and II. The actual beam and skin dimensions are summarized in table 3.1 for models I through V.

The models used graphene and the carbon nanotube composite due to their very high modulus of elasticity and light weights. Graphene is one of the strongest materials ever measured with a Young's modulus of 1.0 tera-pascals, and an intrinsic

Table 3.2. Manufacturing constraints identified by Schwemmer [9]

	Dimension	Units
Beam cross-section radius	2.625e-02 (8e-03)	ft (m)
Beam cross-section thickness	6.562e-04 (2e-04)	ft (m)
Skin thickness	1.6404e-06 (5e-07)	ft (m)

strength of 130 giga-Pascals[11]. This allows the material to maintain a light enough weight while providing the strength necessary to counteract the large stresses being placed on the frame. With a layer of graphene as small as 0.335 nm for the material properties listed, graphene will add essentially no weight to the system allowing the W/B ratio to be much smaller than previously looked at materials. The material properties for graphene in these models were given by Air Force Research Laboratories (AFRL) and used in previous analyses by Schwemmer.

The carbon nanotubes are still young in their production process, but have shown considerable strength to weight ratios as well. The CNT cannot be made into a pipe by its self and therefore needs an epoxy matrix to form the geometry. Cranston identified the CNT composite which utilized the matrix consisting of Bismaleimide (BMI) [7],[2]. With a CNT composite sheet being able to withstand a tensile loading of 3.8 GPa and having a Young's modulus of 293 GPa, this material allows each beam to maintain a weight of 0.639 grams while providing the initial support of the structure[10]. The material properties have been summarized in tables 3.3 and 3.4.

Table 3.3. Hexakis Icosahedron CNT/BMI Material Properties [10]

	Dimension	Units
Density	78.035 (1250)	$lb/ft^3(kg/m^3)$
Modulus of Elasticity	6.119e09 (293)	$lb/ft^2(GPa)$
Poisson's Ratio	0.33	unit less
Yield Stress, σ_y	551.143 (3.8)	ksi (GPa)

Snyder's model of the hexakis icosahedron built in Solid Works was imported into Abaqus' FEA software as a wire beam model and became the basis for model I. A

Table 3.4. Hexakis Icosahedron Graphene Material Properties [11]

	Dimension	Units
Density	124.8559 (2000)	$lb/ft^3(kg/m^3)$
Modulus of Elasticity	1.044e10 (500)	$lb/ft^2(GPa)$
Poisson's Ratio	0.10	unit less
Yield Stress, σ_y	7251.887 (50)	ksi (GPa)

second version was made and scaled to have a diameter of 4 ft (1.2192 m) to become the basis for model IV. Figure 3.1 depicts the wire beam model from Abaqus. The material properties from Schwemmer's research and table 3.3 were applied to the models along with the beam profile dimensions calculated in MATLAB and shown in table 3.1. This produced the frame of the hexakis icosahedron shown in figure 3.2 and used for models I and IV.

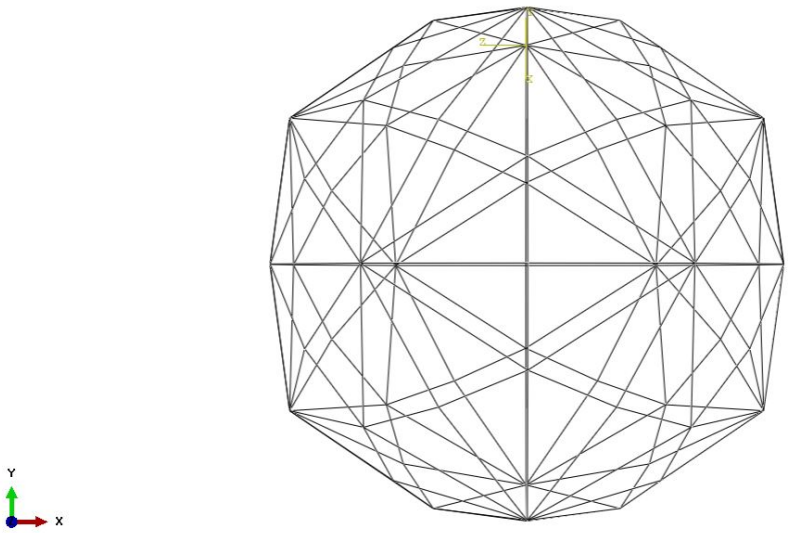

Figure 3.1. Hexakis Icosahedron Wire Profile

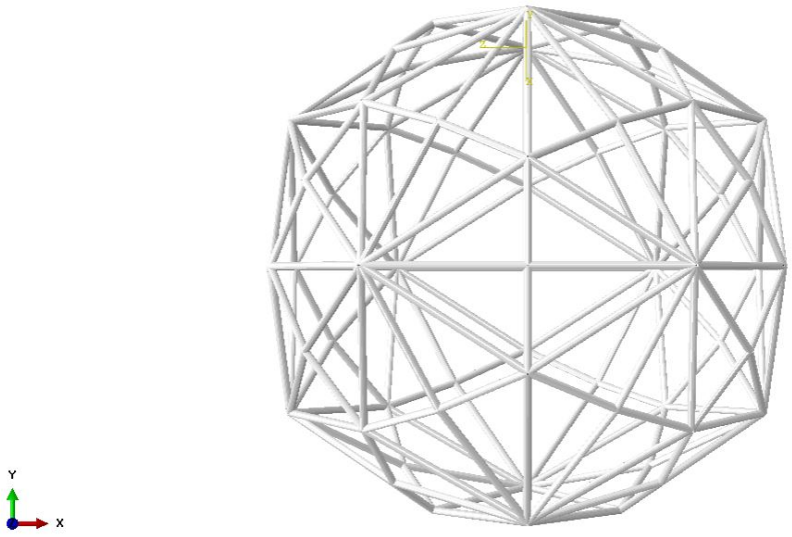

Figure 3.2. Hexakis Icosahedron Beam Profile

In order to analyze models I and IV, a method for applying the atmospheric pressure to the frame needed to be established. This was done through a reference point technique as shown by Adorno-Rodriguez in his research as an accurate method of estimating the loading conditions [5]. The technique is achieved by finding the center of mass of each individual triangular face, which is composed of straight beams making up the triangle. Abaqus has built in tools to calculate the center of mass, which was also verified by a simple hand calculation. Once this value is known, a reference point is placed at that location. When all 120 faces had a reference point, a coupling constraint was used in Abaqus to tie the motion of each triangular face to the motion of their respective reference point [21]. This is shown by figure 3.3. This technique guarantees that the load applied will act at the center of each triangle and become distributed evenly.

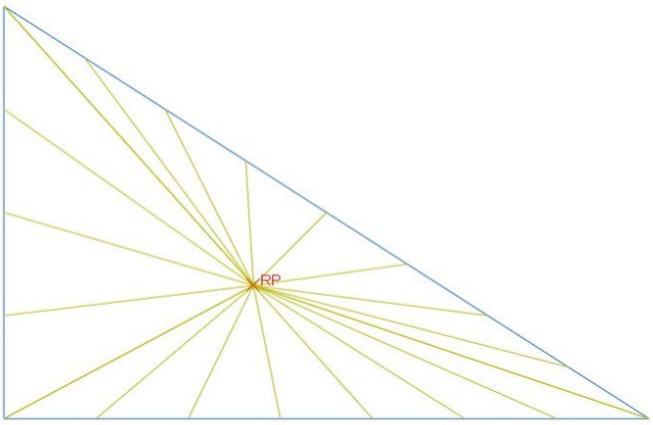

Figure 3.3. Single triangular face with the continuum constraint reference point technique

In the Abaqus graphical interface for the constraint definition, each triangle was selected to be a circumferential surface, and each reference point was selected as a control point. Using the continuum distribution coupling type, a restriction on all six degrees of freedom occurred. This reference point technique generated 120 sets of coupling constraints that can be seen in figure 3.4 with a single set highlighted. These steps and options can be seen in the appendix.

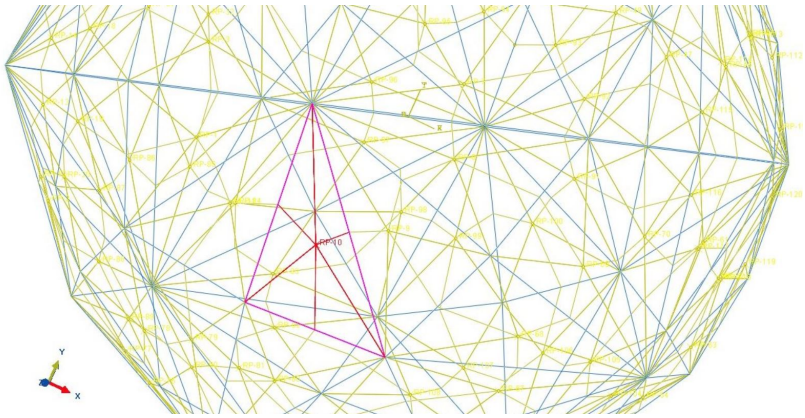

Figure 3.4. Hexakis Icosahedron structure with a single continuum constraint identified

The atmospheric pressure was then applied as a concentrated load at each reference point using a spherical coordinate system to direct the loads towards the center of the structure. The "follower" force option was selected to allow the force to follow

the nodal displacement. This allowed the concentrated force to act as a pressure load while the structure deforms by keeping the force normal to the surface of the structure. Due to the large deformations of the structure, a nonlinear analysis had to be used to obtain accurate results. In order to apply an equivalent concentrated force, sea level pressure was multiplied by the surface area, which was found using Abaqus, of the triangular faces to produce a force in Newtons. This equated to different values depending on the size of the hexakis icosahedron frame. The 0.3408 m diameter frame, model I, used a concentrated force of -210.326 N, while the 1.2192 m frame used a concentrated force of -3374.12 N. These forces were applied to each of the triangular faces with their respective reference point through the Abaqus CAE load display. Figure 3.5 depicts the loading conditions described as well as the boundary conditions at the top and bottom of the frame for model I. The boundary conditions involved restricting the Degree of Freedom (DOF) at the top and bottom nodes from translating in the U1 and U2 directions. This left the U3 direction, the vertical direction, to be free to translate. These boundary conditions were shown in previous research to give the most symmetric results while allowing the model to converge [5].

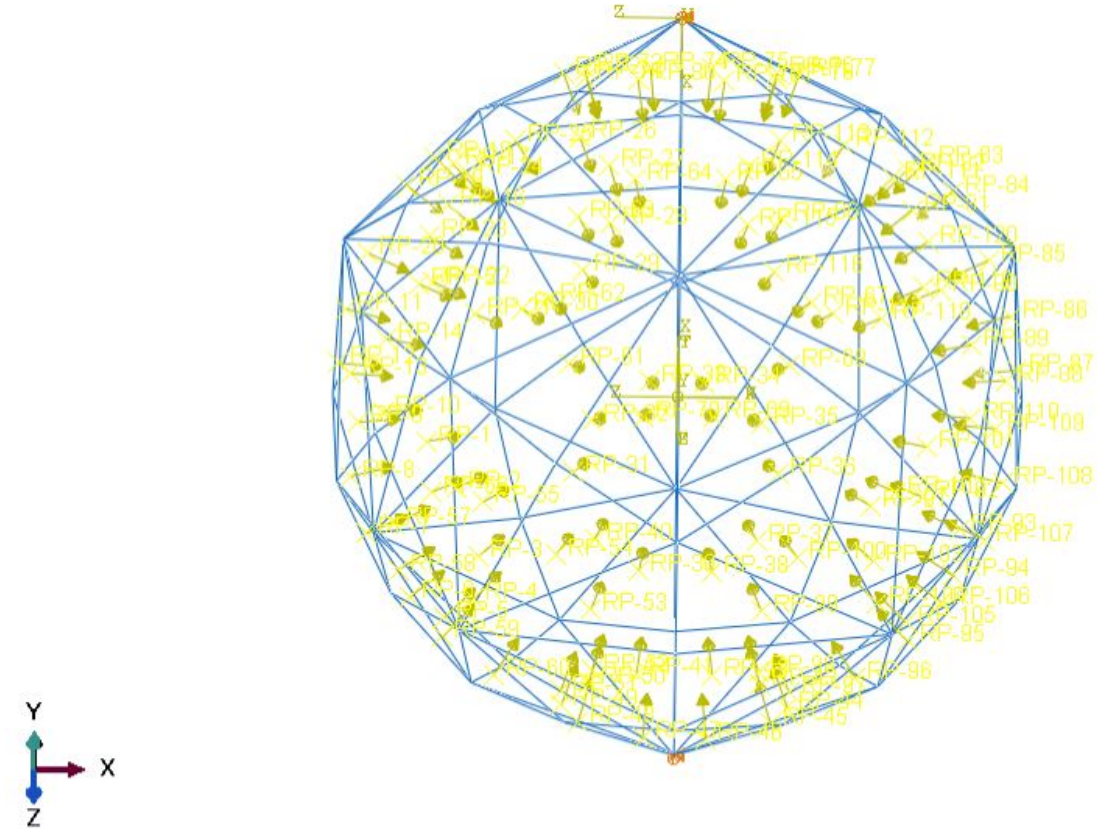

Figure 3.5. Hexakis Icosahedron loading and boundary conditions model I

As more models are introduced and talked about in this research, models I-V will be followed by a short description of the overall diameter of the structure, whether it is just the frame or the frame and skin (f/s), what size beams were used: the roughly 1 mm or 8 mm beams, and the BCs used: none or BC3. This notation should help keep track of the different models during the following chapters. An example of this for reference would be model II (ø=0.3408 m, f/s, 1 mm beams, none), which is the 0.3408 diameter model built with the optimized beams that were 0.955 mm in radius and had a skin attached, with no BCs.

Model IV (ø=1.2192 m, frame, 8 mm beams, none), which is simply a larger version of model I, but with thicker beams was able to converge on a solution in Abaqus without using boundary conditions. Previous research had utilized the boundary

conditions described for model I, in order to avoid causing a singularity and resulting in a failed computation of the simulation. The reason this model was able to run without BCs is most likely due to the symmetry of the structure and the linear response of the frame, in combination to the specific loading being applied exactly at the center of mass of each triangular face. The results of this detailed in chapter IV. Figure 3.6 depicts the loading conditions and lack of boundary conditions utilized in model IV.

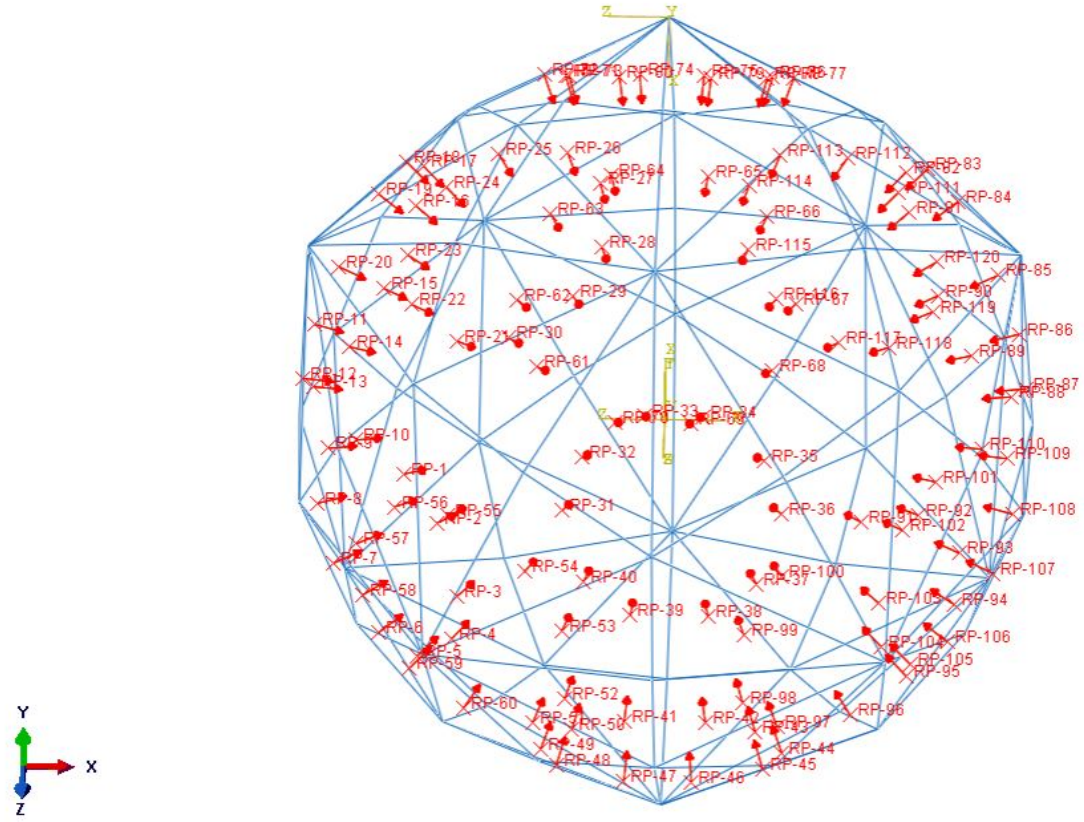

Figure 3.6. Hexakis Icosahedron loading and boundary conditions model IV

The hexakis icosahedron frame was constructed of B32 elements in the FEA software Abaqus. The B32 element is a three dimensional quadratic element accounting for six degrees of freedom at each of the three nodes. The B32 element is modeled as a Timoshenko beam which is mainly known for being able to model transverse

shear deformation through its quadratic interpolation. Abaqus makes the assumption "that the transverse shear behavior of Timoshenko beams is linear elastic with a fixed modulus and, thus, independent of the response of the beam section to axial stretch and bending" [21]. Previous research by Adorno-Rodriguez showed that eight of the B32 beam elements were needed per beam for convergence, and all previous research has used the same amount. This research utilized eight or more of the B32 beam elements per beam for the mesh of both models I and IV for consistency. The result was a model consisting of 1440 elements with 2760 nodes. Figure 3.7 shows the mesh applied to the frame and figure 3.8 is a zoomed in visualization of one of the vertices.

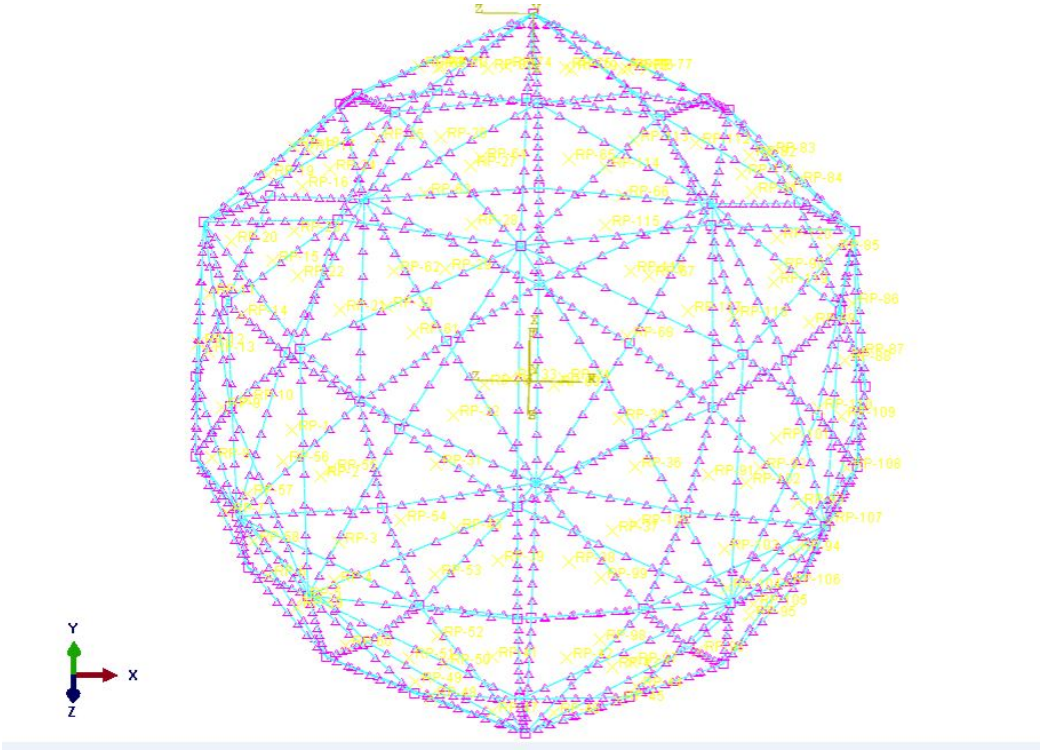

Figure 3.7. Hexakis Icosahedron frame mesh-1440 B32 beam elements

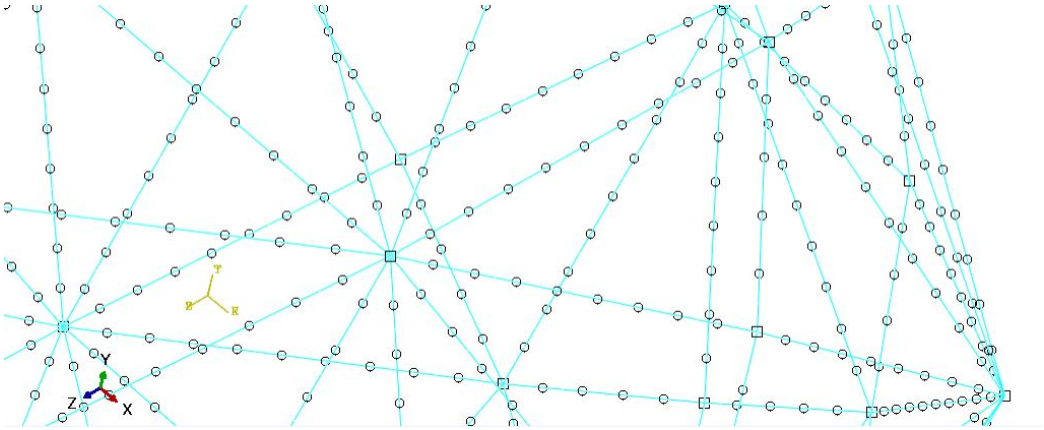

Figure 3.8. Hexakis Icosahedron frame mesh-1440 B32 beam elements - zoomed in

The membrane like skin which is applied to the frame to complete the structure is constructed of M3D3, 3-node triangular membrane elements. The M3D3 is a three dimensional cubic element with three degrees of freedom at each of the three nodes. These elements were used in previous research for static loading and offer strength in the plane for loading, but do not have bending stiffness. Another element that could have been used is the S3R element, which has given very similar results as the M3D3 element, but has the ability to account for the three rotational DOF as well. The structure, model III and V, consists of 2100 quadratic line elements of type B32 and 13792 linear triangular elements of type M3D3. Figure 3.9 depicts the mesh of the frame with the membrane like skin attached and figure 3.10 zooms in on one of the vertices of the mesh.

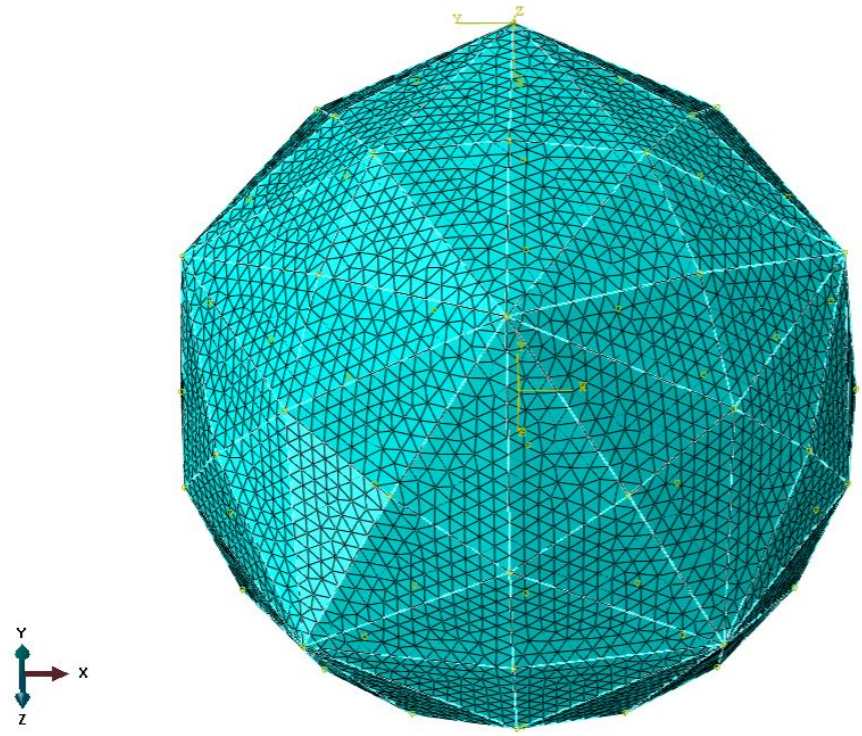

Figure 3.9. Hexakis Icosahedron skin mesh-13792 M3D3 3-node triangular membrane elements

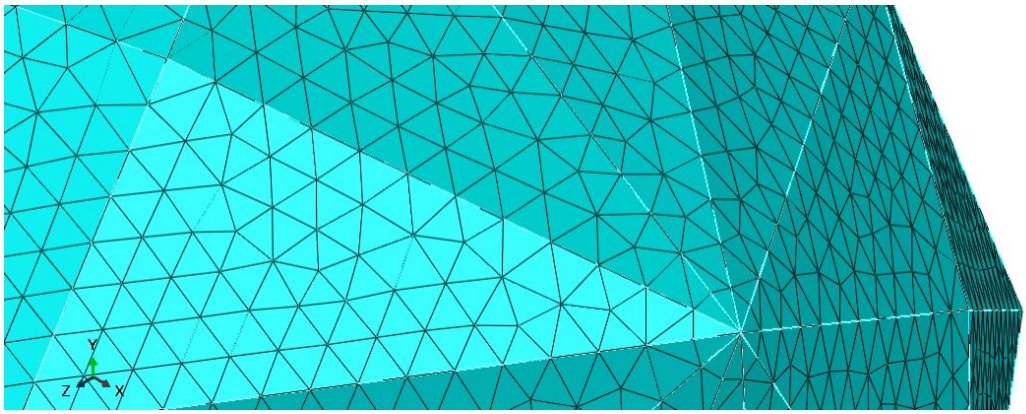

Figure 3.10. Hexakis Icosahedron skin mesh-13792 M3D3 3-node triangular membrane elements - zoomed in

3.2.2 Air Evacuation Models

The air evacuation design was analyzed utilizing a combination of standard fluid dynamic calculations, and the development of two more FEMs. These FEMs are simplified representations of the overall system. This was done by analyzing the stress profile of model V and applying similar loading conditions to a portion of the overall model in an attempt to reduce the modeling, but generate accurate results. The need for the simplified models is due to the fact that the structures have been utilizing wire beam line elements, which cannot model the air evacuation system being applied to portions of the beam. This requires a three dimensional model in the FEA software to capture the true effects of the overall system.

The two simplified models were built in Abaqus using three dimensional homogeneous solids to represent the two different air evacuation systems. The structures were meshed using Abaqus' C3D10, 10 noded tetrahedral elements. This element has three translational DOF per node and is ideal for quick computation of three dimensional models. To reduce the error an excessive number of elements was utilized. Table 3.5 shows the number of nodes and elements for each design. Figures 3.11 and 3.12 show the models and their respective meshes.

Table 3.5. Mesh parameters of simplified air evacuation models

Design	Element Type	DOF/node	# nodes	# elements
1	C3D10	3	114107	69148
2	C3D10	3	688906	354462

Both models were analyzed linearly and non-linearly to identify how the model responded and to get the most conservative model. The linearity test of the deformation is displayed in chapter IV.

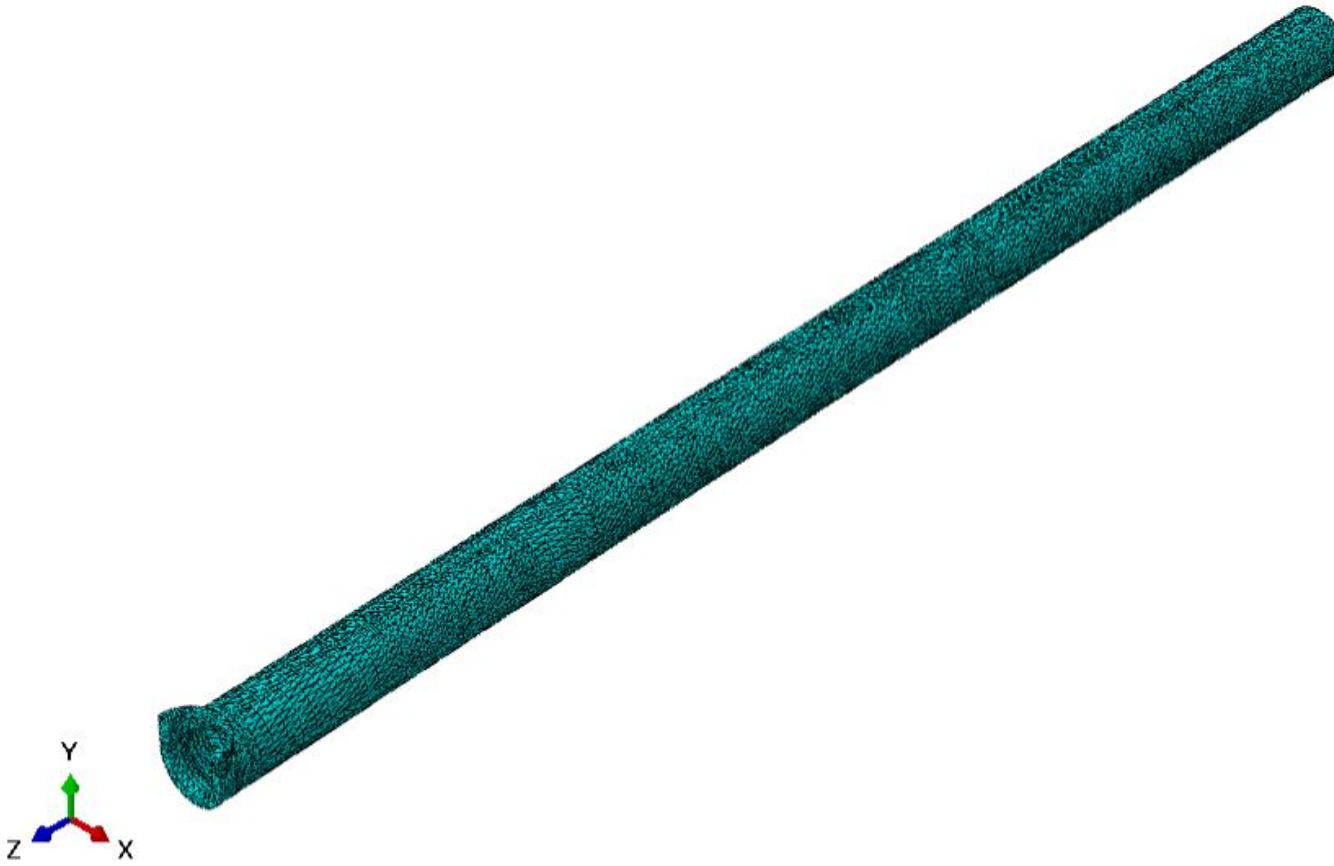

Figure 3.11. Meshed air evacuation system 1

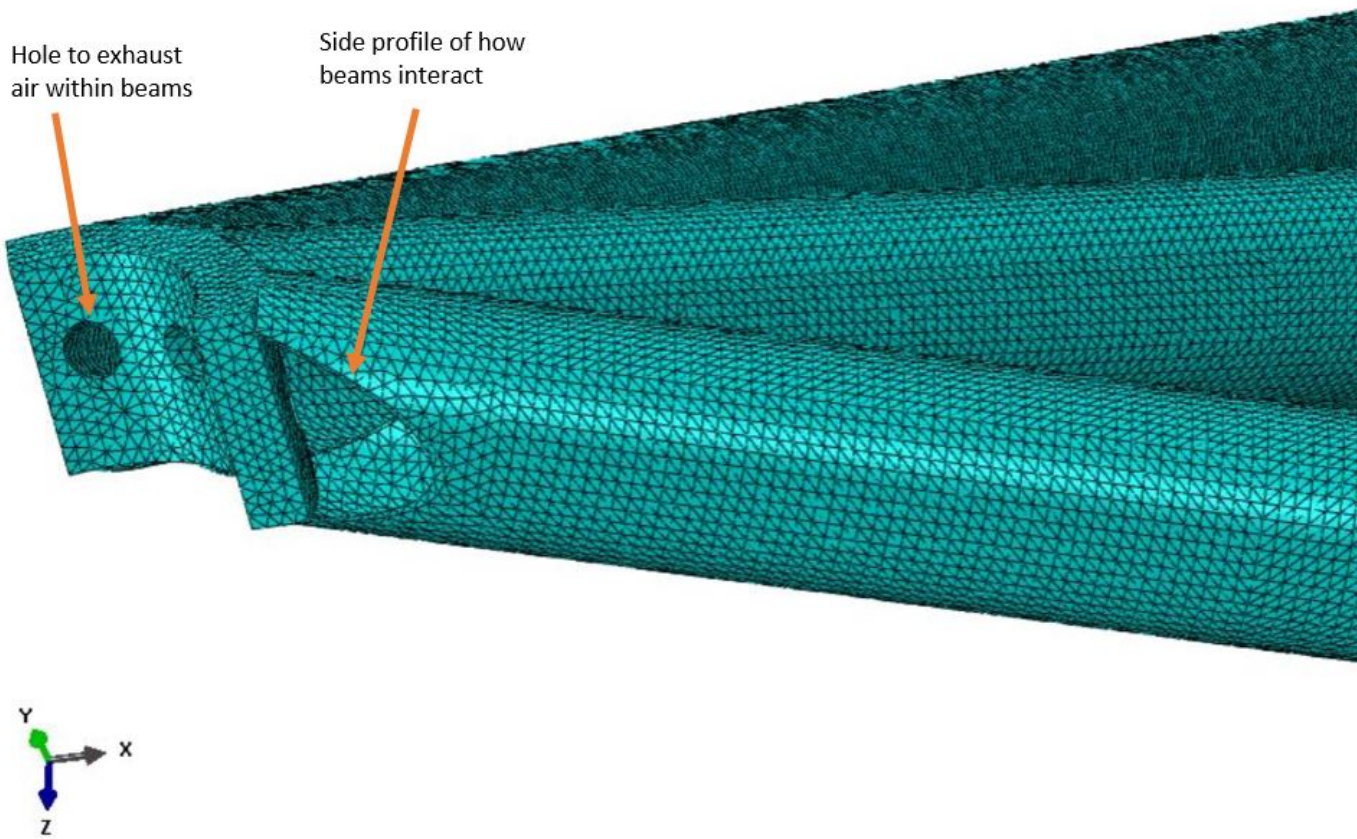

Figure 3.12. Meshed air evacuation system 2

The models were loaded using pressure loads down the center of the beams. To get an equivalent loading the calculated concentrated loads that were used in model IV (ø=1.2192 m, frame, 8 mm beams, none), with the reference point technique were multiplied by the length of the beam. The beam lengths were slightly different depending on which beam was used. The main beam being analyzed was 323.129E-03 m long. Abaqus takes the load and distributes it evenly along each of the beams, so by multiplying the force, 3374.12 N, by the length of the beam, the magnitude of the force for each individual beam was obtained to be 1090.3. There is a force being applied on each side of the beam due to the geometry of the structure. This was accounted for by multiplying the magnitude by 2, in order to obtain the actual magnitude, which was approximately 2182. Abaqus cannot apply a line load to a 3 dimensional model, so the force had to be inputted as a pressure or a concentrated load. Within the pressure menu of Abaqus there is an option to input the pressure load with the total force option selected to distribute the force evenly over the given area. This allowed the creation of a line load without having to calculate how the force was being distributed due to the geometry. This also allowed the force to be applied as a pressure, in the sense that the magnitude of the force was normal to the surface, removing the need to apply three different loads to simulate the correct direction of the load. A screen shot of applying this load through the Abaqus CAE has been included in the appendix.

The models were constrained at the exhaust end from translating and rotating in all three directions to simulate being joined to ten other beams. The other end of the beam was constrained from translating in all three directions to simulate the 3 other beams connected to it. This allowed the beams to rotate, but prevented translational DOF at the ends of the beam. The constraints and loadings for the exhaust end of each model are shown in figures 3.13 and 3.14.

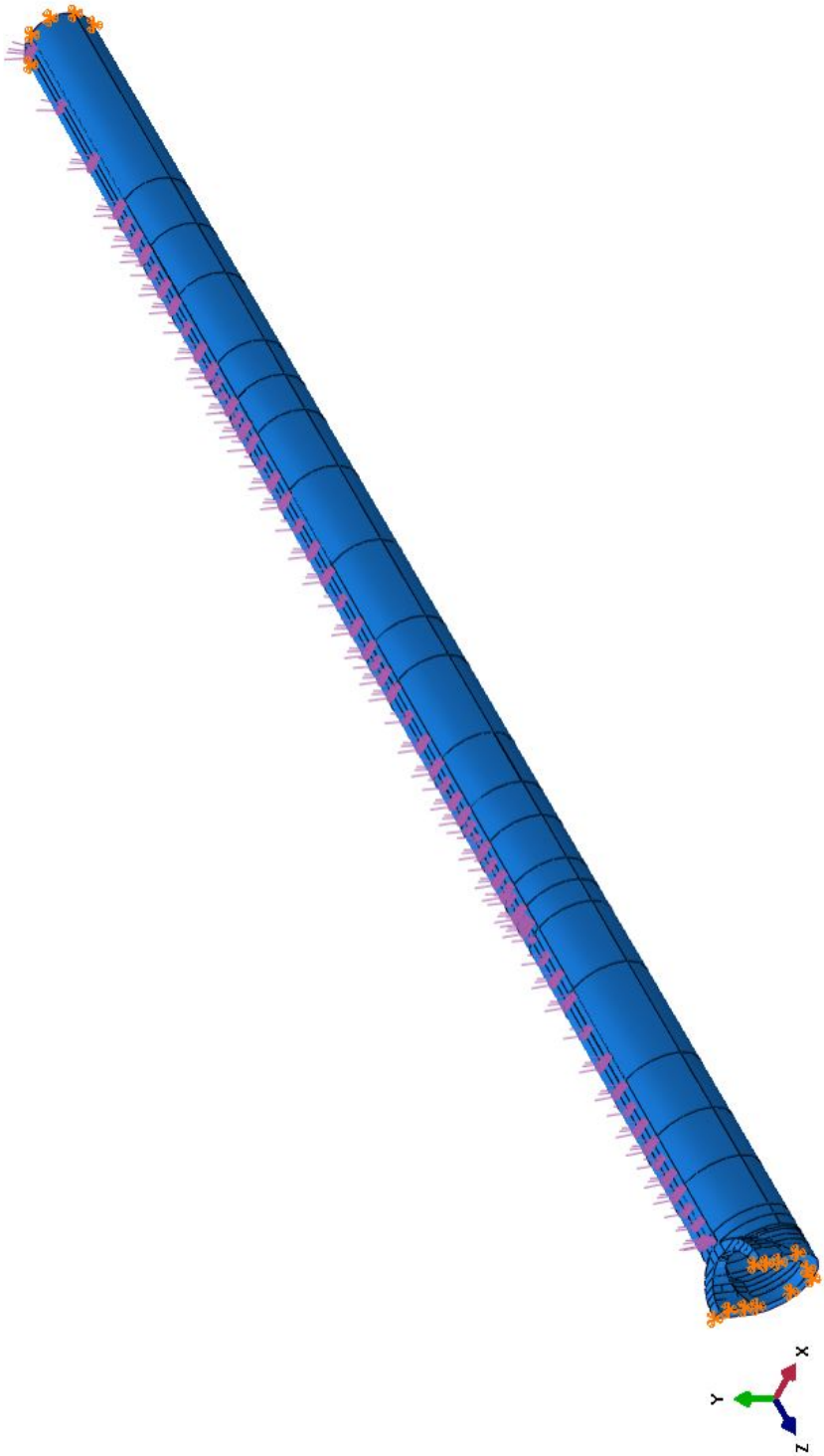

Figure 3.13. Constraints and loading of air evacuation system 1

Figure 3.14. Constraints and loading of air evacuation system 2

3.3 Summary

This chapter presented the model creation and methodology for analysis of the hexakis icosahedron frame, frame and skin, and air evacuation. The FEA software Abaqus was utilized in all model creation, with MATLAB and Python contributing to the development of the Abaqus input files (.INP). There were several models of the hexakis icosahedron developed for comparisons between other research and the most favorable model to date, the optimized structure presented by Schwemmer. The hexakis icosahedron will be analyzed statically at 100% sea level pressure with the frame by its self, and the structure consisting of the frame and skin. Stress fields of the hexakis icosahedron will be compared to those of the icosahedron for better understanding into what parameters affect the structure most significantly and to identify the stress concentrations for air evacuation design. Chapter IV will present the results of the models mentioned in this chapter, along with the results from the fluid flow equations mentioned.

IV. Results

4.1 Chapter Overview

Modeling, loading techniques, and flow equations were discussed in chapter III. The hexakis-icosahedron has been analyzed dynamically and even optimized for a Weight-Buoyancy Ratio (W/B) of 0.7654, but the manufacturing of the structure has not been considered. In order to validate the Finite Element Analysis (FEA) of the structures to date, an air evacuation system needs to be designed to evacuate the air while still providing enough strength to resist buckling.

This chapter will describe the results from the models built in Abaqus and the different tests that were done to statically assess the stress fields of the hexakis-icosahedron and specifically the air evacuation design. The results will cover:

- The comparison between the one foot diameter icosahedron from Adorno-Rodriguez's work and the hexakis icosahedron using Carbon Nano-Tube (CNT) material properties for the frame and skin.
- The FEA results for models I (ø=0.3408, frame, 1 mm beams, BC3), model II (ø=0.3408 m, f/s, 1 mm beams, none), model III (ø=0.3408 m, f/s, 8 mm beams, BC3), model IV (ø=1.2192 m, frame, 8 mm beams, none), and model V (ø=1.2192, f/s, 8 mm beams, BC3) of the hexakis icosahedron at varying diameters using a CNT/Bismaleimide (BMI) composite frame and graphene for the skin.
- The fluid flow computations and air evacuation designs with their respective FEA results.

4.2 Icosahedron and Hexakis Icosahedron Comparison

The icosahedron was analyzed in the finite element solver, Abaqus, by Adorno-Rodriguez, where two models were found that could potentially survive using a CNT composite as the material for both the frame and the skin [5]. The material was called Nanocyl NC7000 thin multi-wall CNT composite. To accurately compare the difference, a model of the hexakis icosahedron was developed using the same material properties, but with different dimensions, as the hexakis icosahedron has 6 times the number of beams and it can distribute the force more allowing for thinner beams. The dimensions of the beams and results of the analysis are shown in table 4.1. Models 3 and 7 were the models that Adorno-Rodriguez identified in his research along with the results shown in the table [5]. Model 3h was designed using the set of equations described in chapter II that were made for optimizing the beam dimensions based on a given radius of the structure and the c ratio. Model 7h was built using Schwemmer's manufacturing constraints for the beam dimensions. All models were 1 foot in diameter with the same material properties. The first parameter compared was the W/B ratio for the four different models. The first three models all had a W/B less than one; it wasn't until model four that the W/B exceeded one. This was due to the fact that the beam dimensions were 157% larger than needed for a 1 ft (0.3408 m) hexakis icosahedron due to the manufacturing limitations. The stress fields in the frame were around 6.79 GPa and 8.64 GPa for models 3 and 7 respectively. The stress increased as the beam radius was reduced. Model 3h used a much smaller beam radius and produced an even larger stress concentration of 9.61 GPa. Model 7h had the lowest stress at 0.12 GPa, but this is attributed to its much larger beam radius. The stress fields for the skin become interesting. Models 3 and 7 each have large stress values of 9.62 GPa and 13.3 GPa, which shows that the skin becomes greatly affected by stress concentrations in the frame for the icosahedron. Models 3h and 7h have

stresses of 6.78 GPa and 11.8 GPa in the skin. The stress in the skin is much smaller for the hexakis icosahedron when compared to its counterpart, the icosahedron. This is most likely due to the location of the maximum stress in the skin for each structure. Figures 4.1 and 4.2 show the von Mises stress visualization as outputted by Abaqus. It can be seen that the icosahedron creates stress concentrations at the vertices of the structure, while the hexakis icosahedron pushes the stress concentrations further out from the vertex. The hexakis icosahedron continues to push the stress concentrations in the skin closer to the mid beam location as the radius of the structure increases. This can be seen in stress visualizations of the 4 ft (1.2192 m) hexakis icosahedron. One last comparison between the two structures was conducted. The results are summarized in table 4.2. The two models in this analysis were built to understand the influence the geometry alone has on the studied parameters. The exact same beam dimensions and material properties that Adorno-Rodriguez used in his models 3 and 7 were used in these models. The W/B ratio is slightly larger than 1, but nowhere near that of model 7h. The overall von Mises stress in the frame and skin are both significantly lower than those of the icosahedron. This shows how the hexakis icosahedron is stiffer and redistributes the compressive load better, due to its shape as a sphere and its increased number of beams. To better demonstrate this, the sphericity (a measure of how close the structure is to an actual sphere) of the structures are 0.839 for the icosahedron and 0.94 for the hexakis icosahedron.

Table 4.1. 1ft (0.3048 m) diameter icosahedron and hexakis icosahedron comparison

	Icosahedron		Hexakis	
Model:	3	7	3h	7h
$r_{beam}(mm)$	1.49	1.33	0.955	8.00
$t_{skin}(mm)$	0.0118	0.0118	0.0121	5.E-04
W/B	0.91	0.81	0.8112	15.73
Material Properties	Nanocyl	NC7000	CNT	Composite
Density (kg/m^3)	1650	1650	1650	1650
Poison's ratio	0.2	0.2	0.2	0.2
Modulus of Elasticity (GPa)	1000	1000	1000	1000
Frame				
Maximum Displacement (mm)	3.05	3.97	55.1	0.0111
Maximum von Mises Stress (Pa)	6.79E+09	8.64E+09	9.61E+09	1.20E+08
Skin				
Maximum Displacement (mm)	8.64	9.53	56.4	2.355
Maximum von Mises Stress (Pa)	9.62E+09	1.33E+10	6.78E+09	1.179E+10

Table 4.2. 1ft (0.3048 m) Hexakis icosahedron comparison

		Hexakis Icosahedron	
	Model:	3	7
$r_{beam}(mm)$		1.49	1.33
$t_{skin}(mm)$		0.0118	0.0118
W/B		1.4384	1.2175
	Material Properties	Nanocyl	NC7000
Density (kg/m^3)		1650	1650
Poison's ratio		0.2	0.2
Modulus of Elasticity (GPa)		1000	1000
	Frame		
Maximum Displacement (mm)		0.0576	0.340
Maximum von Mises Stress (Pa)		4.75E+08	7.17E+08
	Skin		
Maximum Displacement (mm)		2.15	2.44
Maximum von Mises Stress (Pa)		4.69E+09	5.50E+09

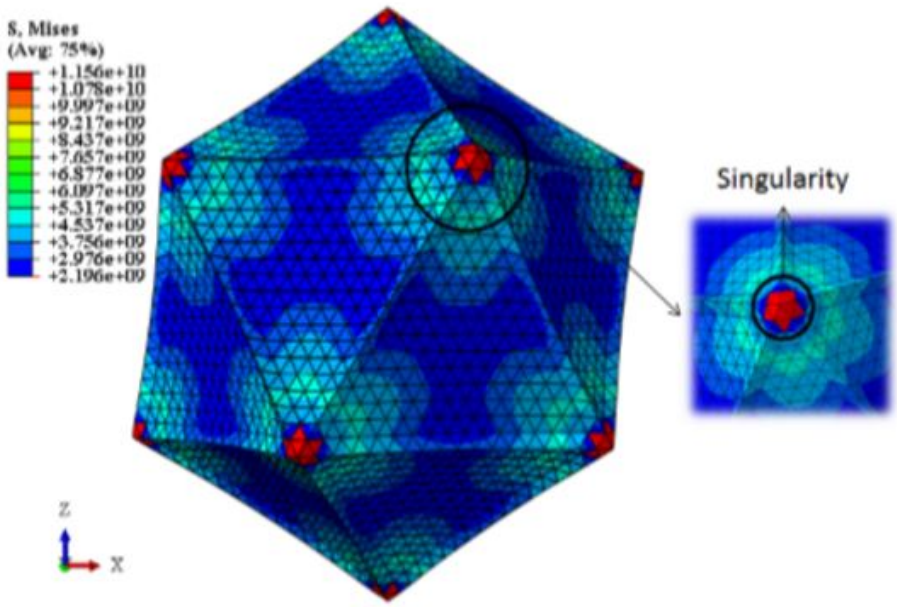

Figure 4.1. Model 7, von Mises stress visualization of 0.3408 m icosahedron [5]

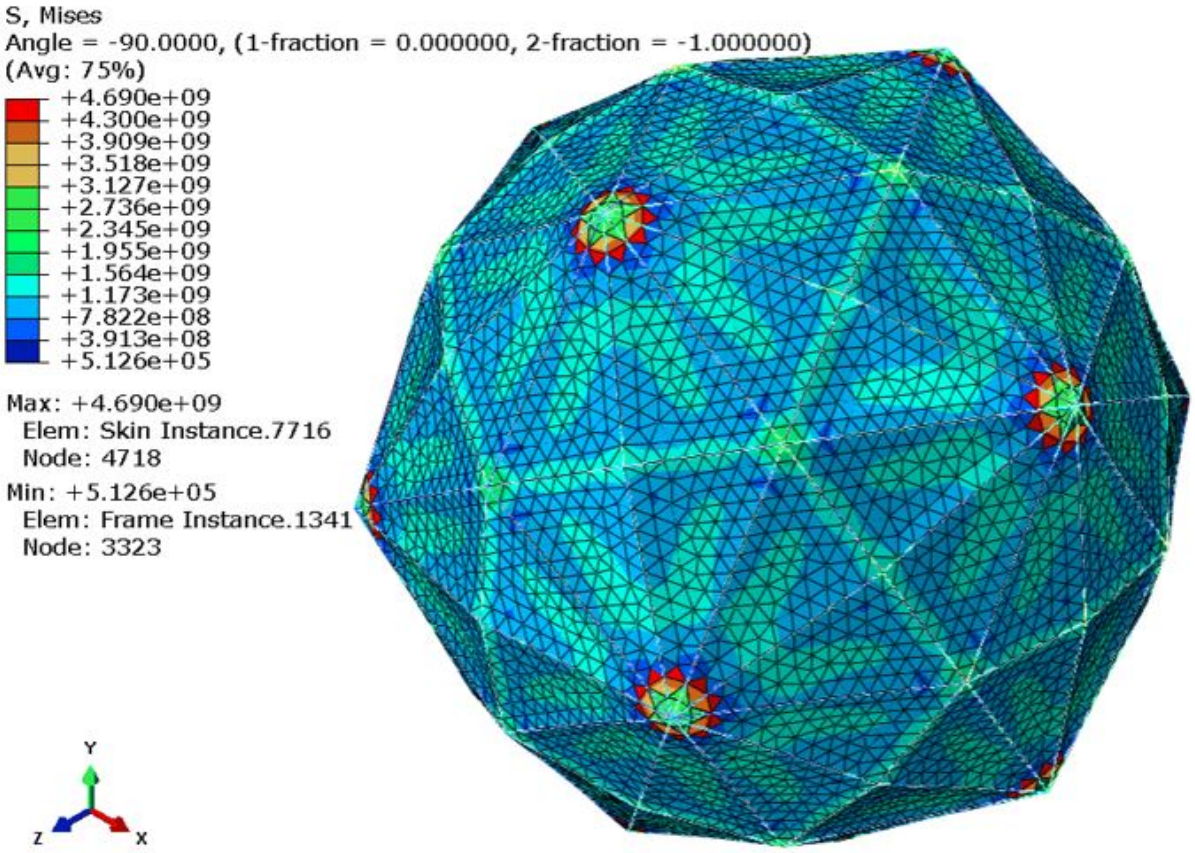

Figure 4.2. Model 3h, von Mises stress visualization of 0.3408 m hexakis icosahedron

The locations of the maximum stresses and displacements are also worth noting for these structures. The icosahedron, models 3 and 7, had stress concentrations at the vertices of the structure in both the frame and the skin. The maximum displacement for this model and almost every other model is located in the middle of the skin of one of the triangular faces. Model 3h showed slightly different results. The maximum stress of the model was in the frame at a vertex near the bottom of the structure. The deformation for this model was in an unusual spot which, explains why the maximum stress was in the frame and not the skin. The maximum deformation was located 33% from one of the minor vertices near the bottom vertex. This is shown in figure 4.3.

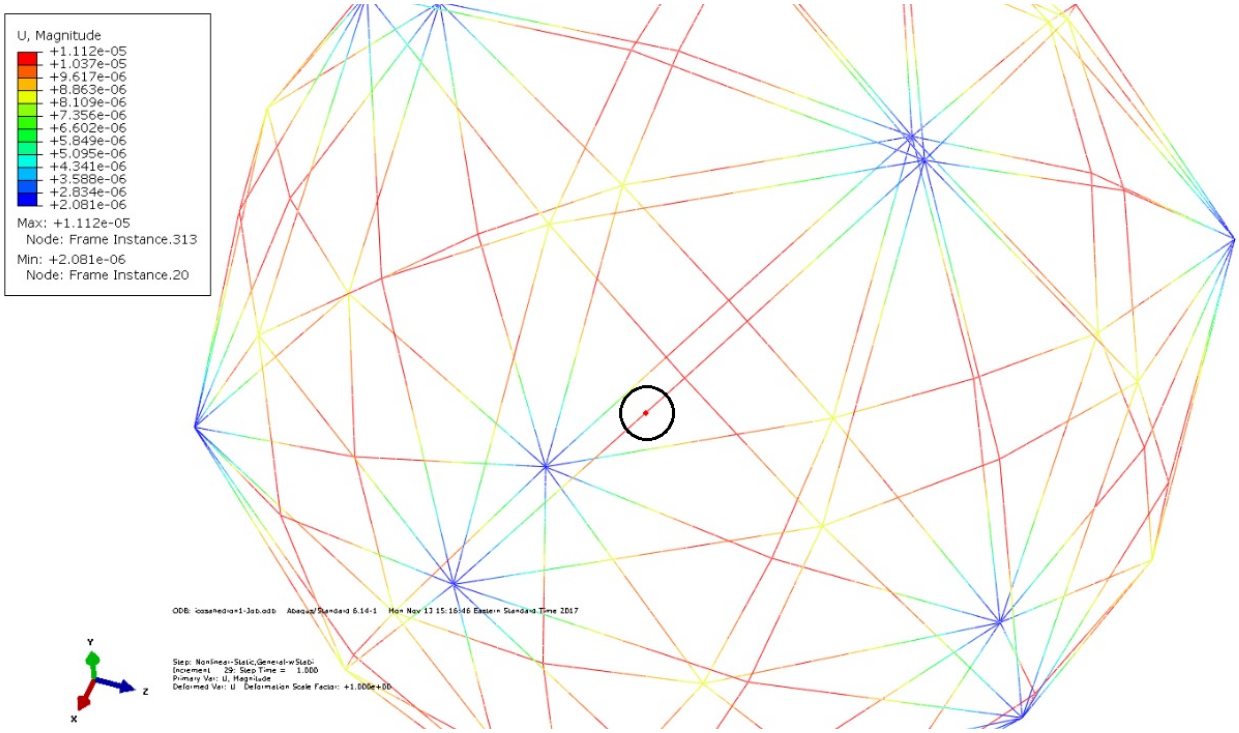

Figure 4.3. Model 3h, deformation visualization of 0.3408 m hexakis icosahedron frame

Models 7h, and the two hexakis icosahedron models 3 and 7, all displayed similar behaviors with the maximum stress being located in the skin along one of the beams near a vertex and the maximum deformation occurring in the middle of the skin of

one of the triangular faces. The maximum value for the models all appear to occur near the bottom side of the structure.

4.3 Hexakis Icosahedron FEA Results

To analyze the hexakis icosahedron, several models were generated in an attempt to produce a structure with a W/B less than one that could survive sea level pressure. Some of the models are designed to be a more conservative approach while others were designed to accurately represent the structure. The models in this section were described in detail in chapter III, specifically by table 3.1. Each of the five models will be presented along with the corresponding results in this section.

4.3.1 Model I

Model I (ø=0.3408 m, frame, 1mm beams, BC3) was split into two separate analyses. The frame has been shown to act linearly, which will be covered later in this section, but this model had severely large deformations which resulted in a linear and non-linear analysis being conducted. The linear analysis presents the most conservative analysis of the frame, while the non-linear analysis incorporates energy dissipation and is typically less conservative. Model I demonstrated the issue with the beam diameter and material limits. The non-linear analysis allows the local material matrix to rotate with the node. This allows for better computation, but can also lead to failure if the beam diameter or material limits are exceed too much.

4.3.1.1 Linear Analysis

Model I was a 1 foot (0.3048 m) diameter hexakis icosahedron consisting only of the CNT/BMI composite frame. The main focus of this model was to create a conservative analysis of the 1 foot model and to compare to previous research which also

looked specifically at the frame, but also for comparison to this research at the 4 foot diameter. As mentioned in chapter III the model was built in Abaqus FEA software based on Snyder's model used in his research. The frame used the CNTBMI composite material properties as shown in table 3.3. The pressure was applied utilizing the reference point technique, Boundary Conditions (BCs) were applied to the top and bottom node, and a quasi-static analysis was conducted. Figure 4.4 shows the stress field of the frame. The maximum stress that occurred was 10.77 GPa. The stress concentrated at the vertices which is expected for a constrained beam under a distributed loading. The diagram has been scaled by a factor of 2.703 to exaggerate the deformation. This simply means that all X, Y, and Z coordinates of the deformation were multiplied by that value to help show, what otherwise would be too small to see a difference. The deformation visualization from Abaqus can be seen in figure 4.5. The max deformations were located at the middle of each beam directly connected to a vertice.

The magnitude of the deformation was 12.05 mm, which exceeds the beam radius by 170%. These large deformations indicate an issue with the structure under these loading conditions. A pipe that exceeds its diameter in deformation should behave in a non-linear manner, requiring a non-linear analysis. This can be seen further in the deformation analysis.

The maximum stress exceed that of the material yield stress by 95.7%. This explains the large deformations as the material has gone beyond its yield point. The stresses reached failure or the yield stress at two places in specific for this model. The first place was at the vertex, where the maximum stresses are located. The second place was in the middle of the beams attached to these vertices, where the stresses floated from 3.6-5.4 GPa. This was a conservative look at the structure as the beams for the model was designed with the skin in mind, however this indicates potential

failure for model II.

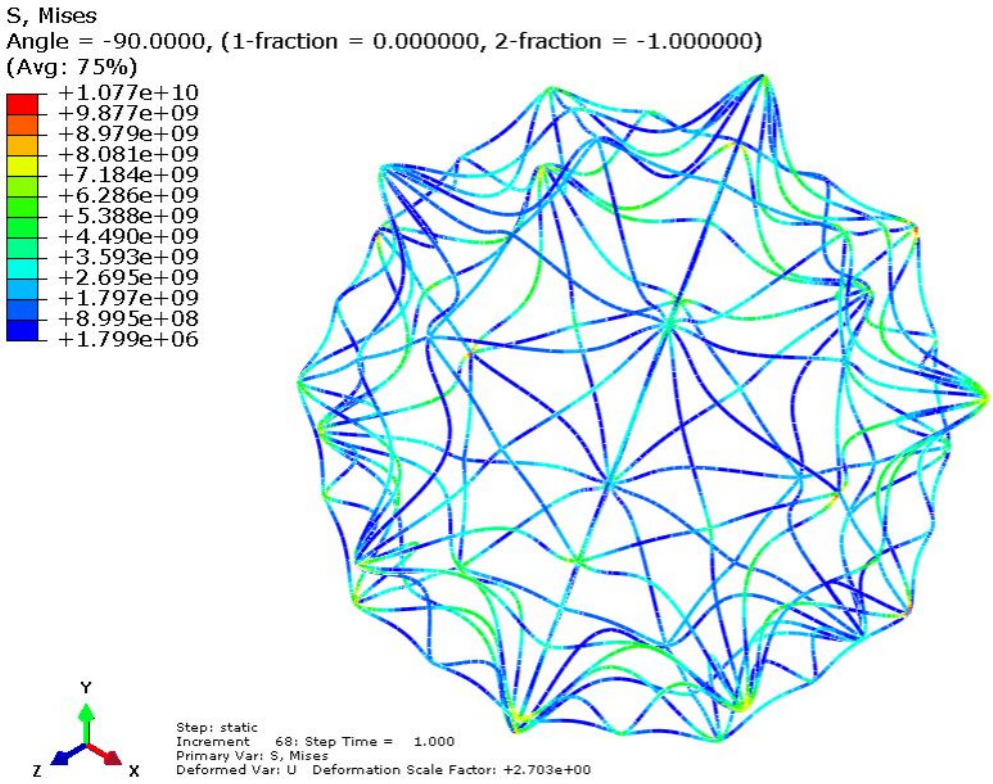

Figure 4.4. Model I (ø=0.3408 m, frame, 1 mm beams, BC3), von Mises stress visualization of 0.3408 m hexakis icosahedron frame

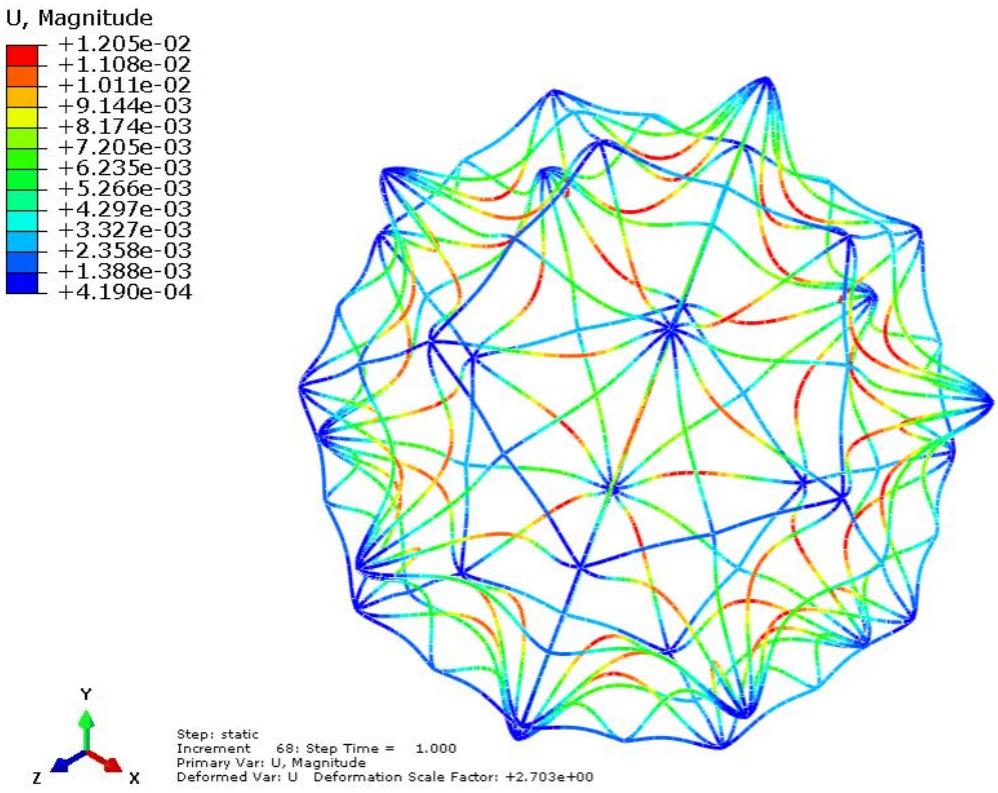

Figure 4.5. Model I (ø=0.3408 m, frame, 1 mm beams, BC3), Deformation visualization of 0.3408 m hexakis icosahedron frame

The linearity of this model was analyzed by tracking the deformation of a point as the loading was incremented. The point was selected to be near the bottom of the structure along one of the edges connected to the constrained node. This was analyzed in Adorno-Rodriquez's research and displayed in chapter II. Model I consisted only of the frame and gave very linear results as shown by the plot in figure 4.6. This makes sense due to the linear analysis and how Abaqus computes the local material directions. The deformations as mentioned earlier were well above the diameter of the pipe and should have produced non-linear results, meaning a non-linear analysis needed to be conducted.

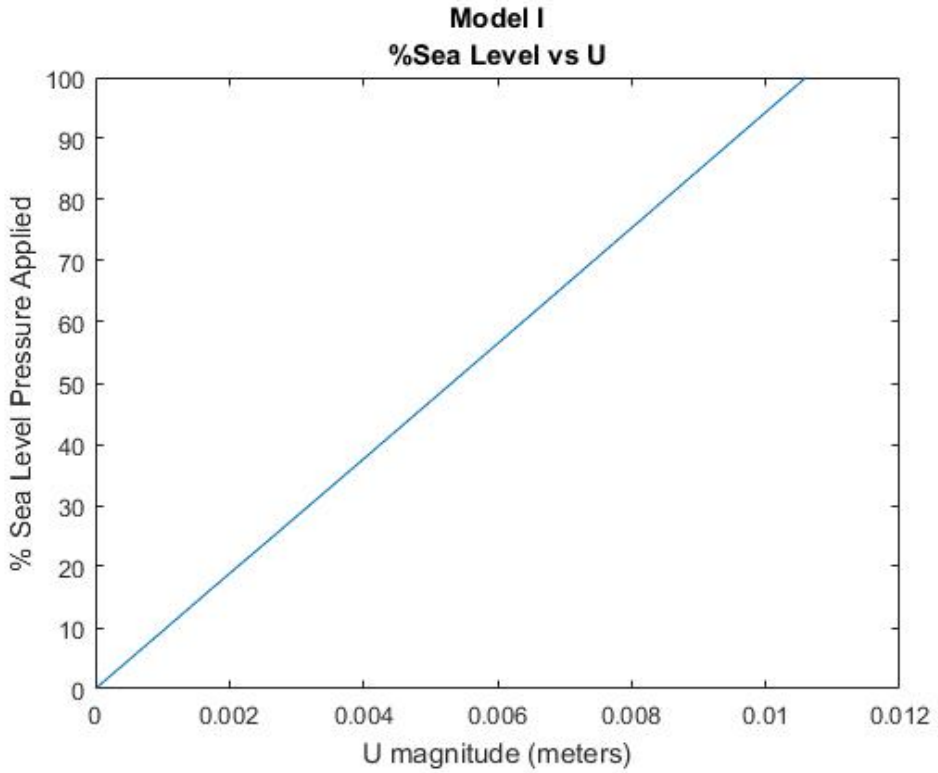

Figure 4.6. Model I (ø=0.3408 m, frame, 1 mm beams, BC3), Frame Tracking - % Pressure applied vs Deformation

4.3.1.2 Non-Linear Analysis

The non-linear analysis kept everything the same except for the non-linear geometry option in the Abaqus step menu. The energy dissipation fraction was also turned on and set to 0.0002 as done for every other model. Utilizing the non-linear analysis resulted in a failed computation. The model began to deform wildly and spring back. This is similar to the snapback behavior identified in previous research, except this model deformed significantly more. The maximum pressure reached was 25.05% sea level pressure. Figures 4.7 and 4.8 show the non-linear collapse and spring back of the structure. The deformations sky rocketed to 4 meters as the structure collapsed and sprang back towards its free direction in the vertical axis. This analysis also demonstrates the impact of the boundary conditions on the model. Previous research showed that the models stability was greatly impacted by which BCs were used, and

this is shown in this model where they actually impose greater stresses on the beams and lead to chaotic behavior.

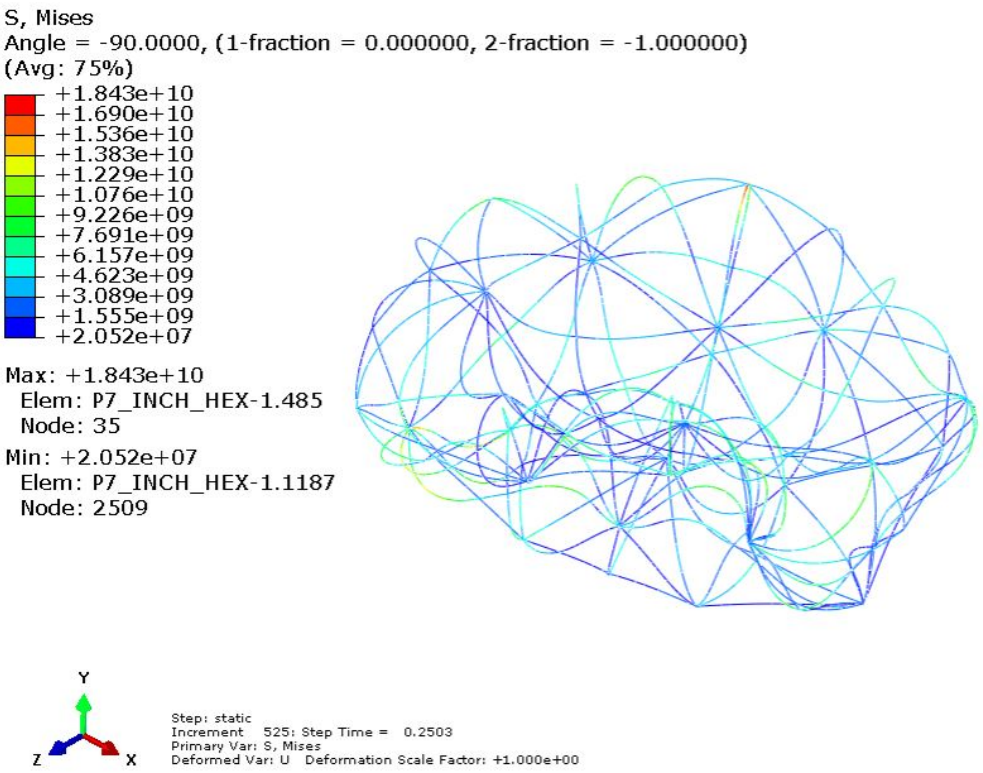

Figure 4.7. Model I (ø=0.3408 m, frame, 1 mm beams, BC3), Frame collapsing during non-linear analysis

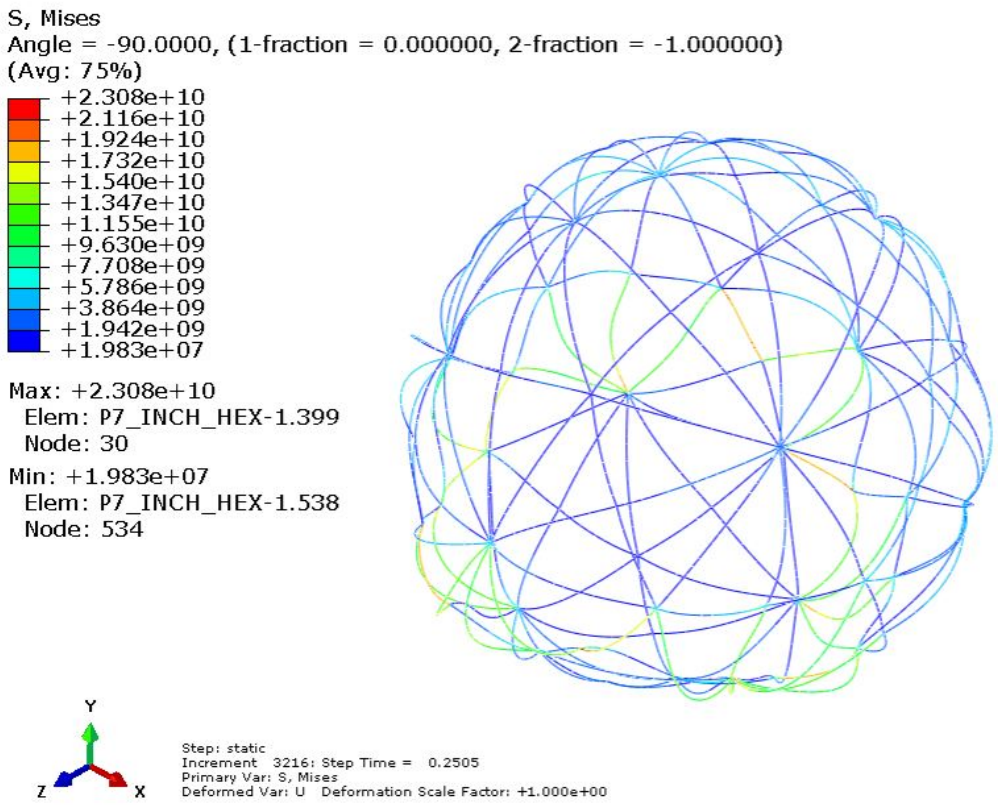

Figure 4.8. Model I (ø=0.3408 m, frame, 1 mm beams, BC3), Frame spring back during non-linear analysis

4.3.2 Model II

Model II (ø=0.3408 m, f/s, 1 mm beams, none) was built from Snyder's model by changing the material properties and loading conditions. The model is a 1 ft (0.3048 m) hexakis icosahedron with a frame and skin attached. The beam and skin dimensions were calculated using the equations in chapter II, the radius of the structure, and the c ratio equal to 0.05. This model did not utilize BCs like the rest of the models. The top and bottom nodes were free in both translation and rotation. This analysis was done using non-linear geometry. The von Mises stress visualization is shown in figure 4.9. The maximum stress was 9.41 GPa located in the frame, unlike every other model that has it located in the skin. Figure 4.10 depicts the deformation of the structure and indicates what's happening a little more detailed. The maximum

deformation of 213.1 mm is occurring in the frame as well, at one of the minor vertices which has been deformed inward.

The maximum stress exceeds the yield stress of the material by 84.9%. This was expected as shown by model I. The maximum stress decreased due to the skin being added, but still remains significantly higher than the yield stress of the material. This simulation was able to produce results for the last step it could iterate, at 94.3% sea level pressure. The model can be seen rotating as the simulation built up the pressure. It is concluded that the beam dimensions were too small or the material was too weak for the given beam dimensions to survive the quasi static sea level pressure applied.

The large deformations of this model are still similar to its counterpart model I in terms of location, however, they are larger by an order of magnitude. This is most likely due to the rotation experienced by the structure during the incrementation. The deformations tended to concentrate around the middle of the model, where several of the minor vertices became concaved inward. Not having BCs allowed for the model to rotate, but still resulted in a successful analysis. The results were symmetrical along the horizontal and vertical plane, but not so in any others. The model never fully reached its full loading criteria of 100% sea level pressure indicating severe deformations, which causes the simulation to halt.

In conclusion, these two models demonstrated that model I does result in a more conservative approach by 13%, when using a linear analysis, and indicated failure in the frame due to the large stresses and deformations. Model II showed the potential for running the simulation without boundary conditions, but still resulting in failure due to the rotations during incrementation. The hexakis icosahedron at 1 ft (0.3408 m) in diameter using the equations to calculate the beam dimensions will result in failure for the CNT/BMI frame and graphene skin materials used.

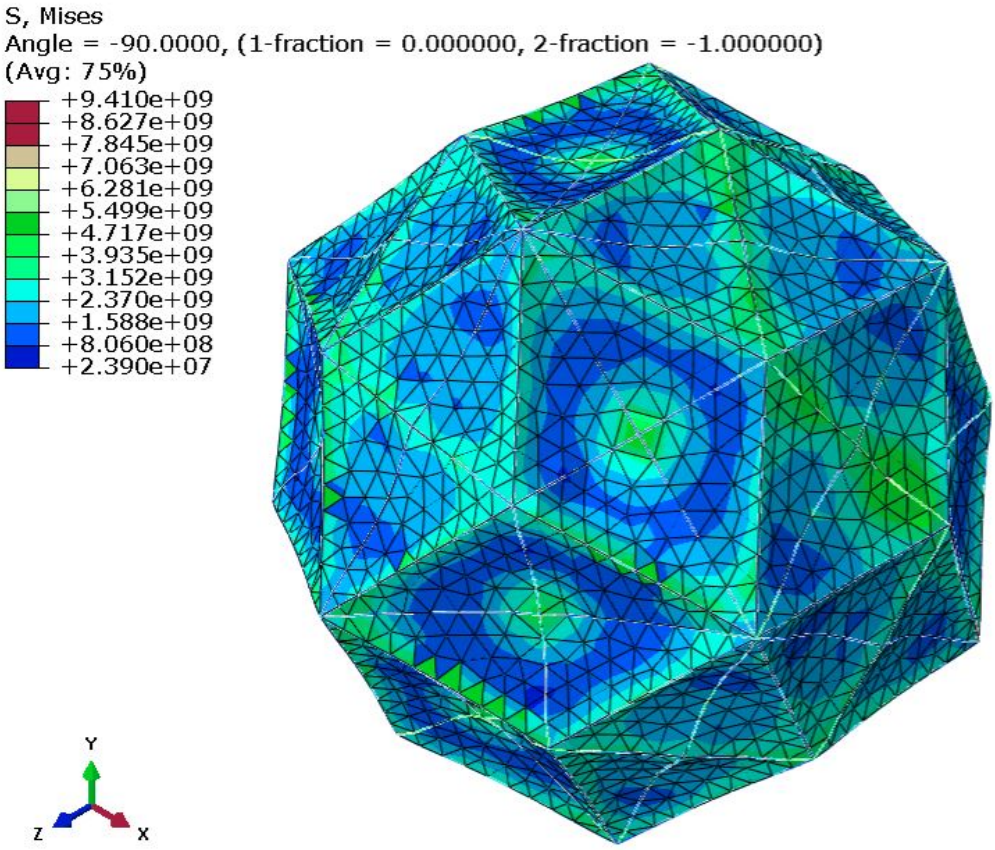

Figure 4.9. Model II (ø=0.3408 m, f/s, 1 mm beams, none), von Mises stress visualization of 0.3408 m hexakis icosahedron

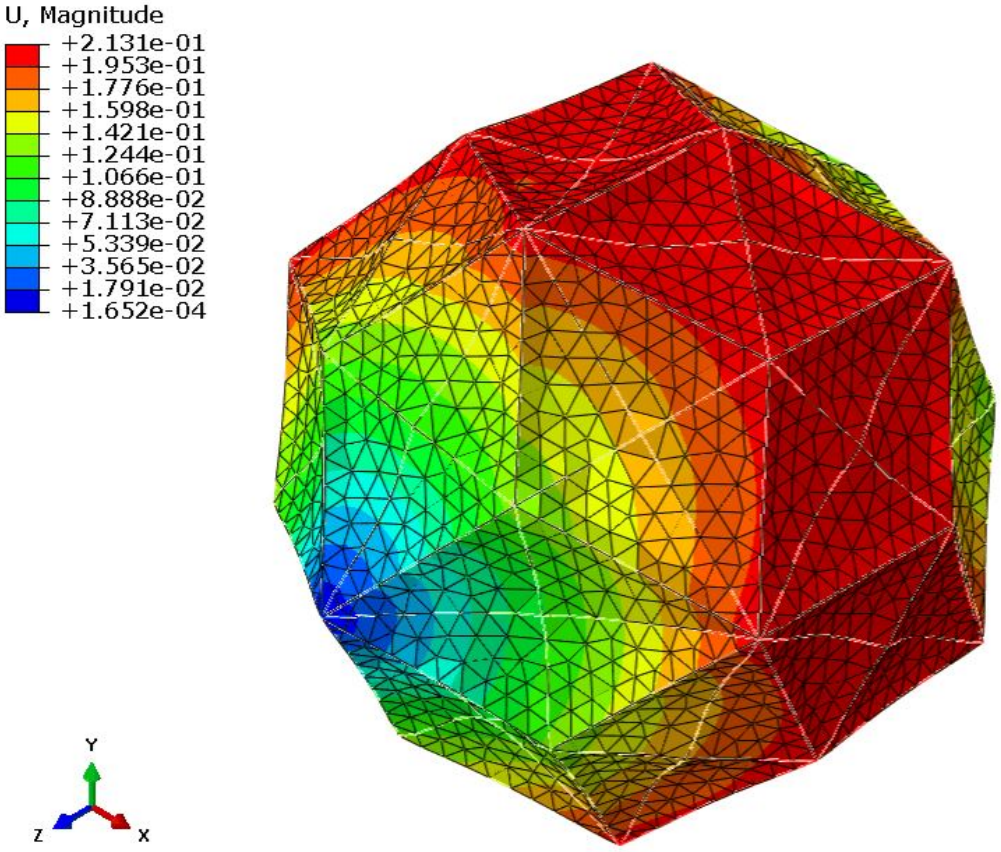

Figure 4.10. Model II (ø=0.3408 m, f/s, 1 mm beams, none), Deformation visualization of 0.3408 m hexakis icosahedron

The linearity of this model was tracked through a point in a similar location to model I. Both the skin and frame deformations at the same place were tracked and resulted in the plot shown in figure 4.11. There is a linear step, where it then becomes unchanging, and then snaps back and the deformation sky rockets. This analysis resulted chaotic and non-linear behavior.

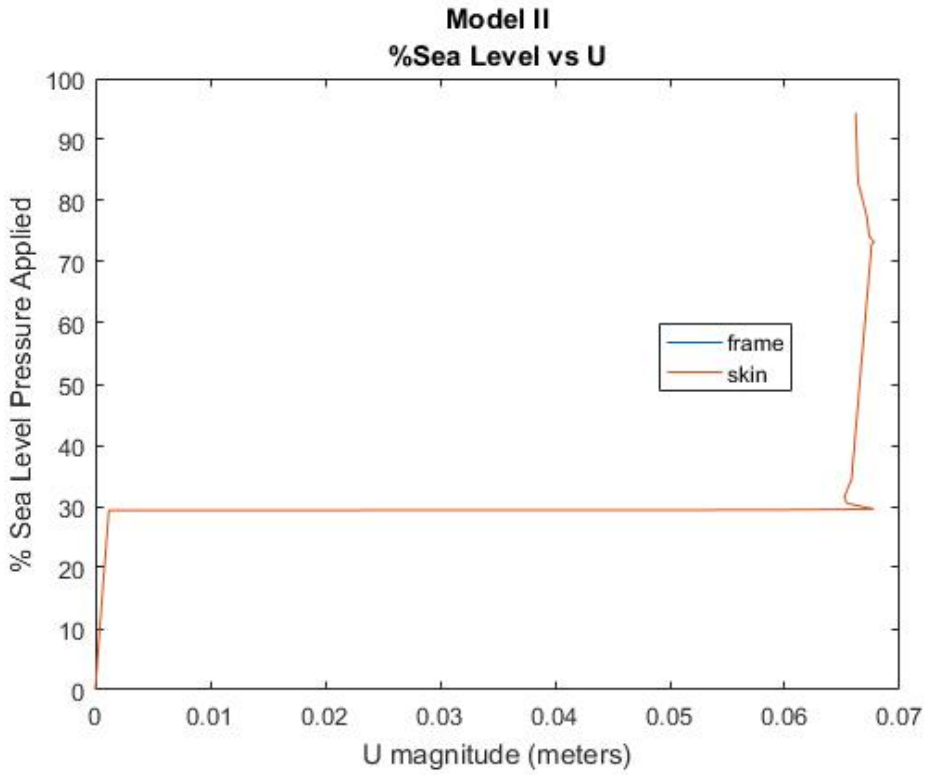

Figure 4.11. Model II, Tracking - % Pressure applied vs Deformation

4.3.3 Model III

Model III (ø=0.3408 m, f/s, 8 mm beams, BC3) has the same radius and material properties as model II except it utilized the beam and skin dimensions identified by Schwemmer. Model II failed due to the beam dimensions or material, therefore model III increased the beam dimensions to those that are used in model IV (ø=1.2192 m, frame, 8 mm beams, none) and V (ø=1.2192 m, f/s, 8 mm beams, BC3) . The first

analysis of this structure was to look at the W/B, which came out to be roughly 11.93. This is well above 1 and has no potential to float in standard air. The stress field produced was significantly better than that of model II. The von Mises stress field is shown in figure 4.12. The stress concentrations in the skin can be seen further away from the vertex in this model, located near the middle of the beams. The deformations for this model are shown in figure 4.13. The maximum displacements occur in the middle of the skin of each triangular face, with the frame maintaining its shape.

The maximum stress was 9.786 GPa located in the skin. This is 134% below the yield stress of graphene indicating the skin did not fail. The maximum stress in the frame was 0.1 GPa, which is 190% below its yield stress of the CNT composite. The overall stresses survive in terms of material limits, and maintain symmetry along the structure. When compared to model II the overall stress is 3.9% larger, but the full incrementation of the sea level pressure was applied and the frame did not fail. Compared to the hexakis icosahedron model 3, which used a different CNT composite for both the frame and the skin, stresses were about 70% larger. The material is about half as strong, yet the beam dimensions play a critical role in the overall stress of the system. In order to reduce the W/B of this structure, either the manufacturing tolerances of the material need to be reduced or stronger and lighter materials need to be identified.

The maximum deformation was 3.082 mm located in a similar location to model V. This structure did deform 35.6% more than the hexakis icosahedron model 3, and 26.7% more than model 7h. The deformations are 88% smaller than the radius of the beams indicating that the frame behaved in a linear manner. While this structure was capable of surviving the loads caused by the vacuum it would not have floated due to its large W/B ratio.

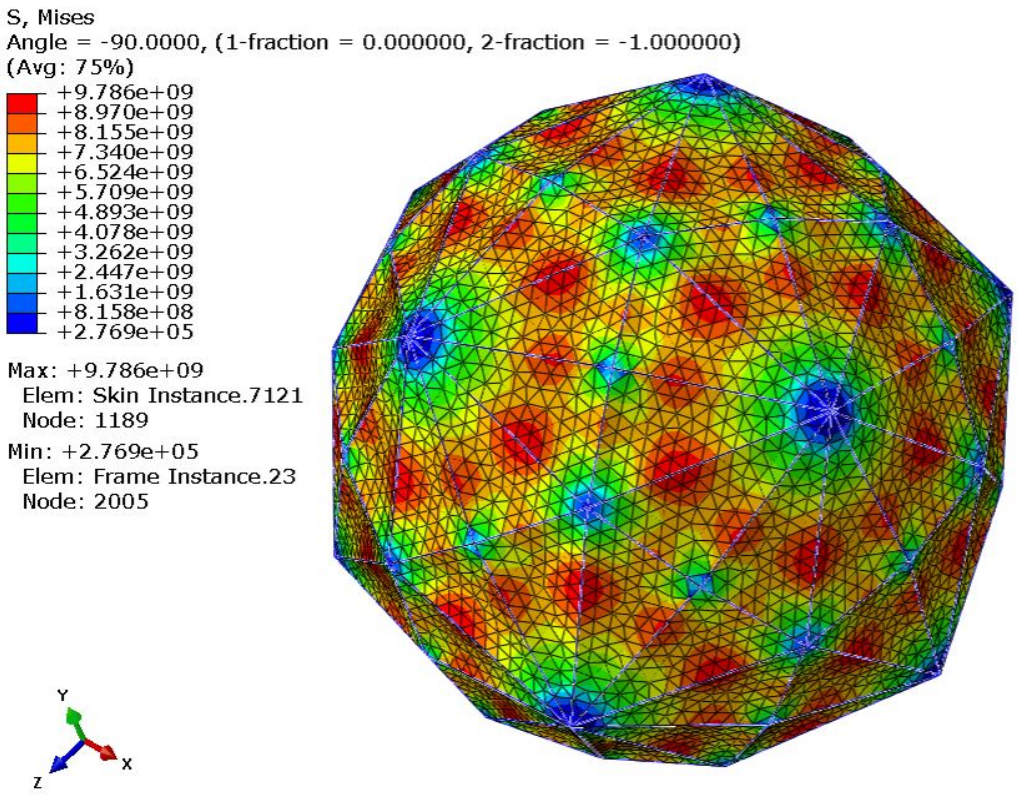

Figure 4.12. Model III (ø=0.3408 m, f/s, 8 mm beams, BC3), von Mises stress visualization of 0.3408 m hexakis icosahedron

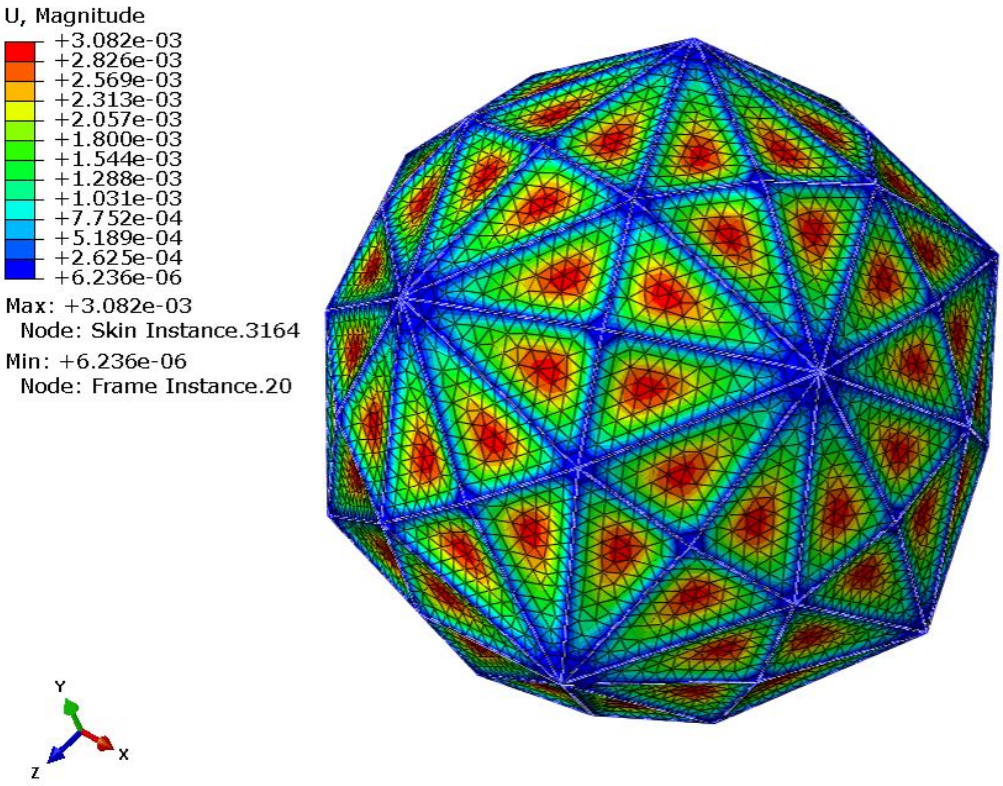

Figure 4.13. Model III (ø=0.3408 m, f/s, 8 mm beams, BC3), Deformation visualization of 0.3408 m hexakis icosahedron

Models III (ø=0.3408 m, f/s, 8 mm beams, BC3), IV (ø=1.2192 m, frame, 8 mm beams, none), and V (ø=1.2192 m, f/s, 8 mm beams, BC3) all behaved in a similar manner when tracking the nodes for linearity. The frame displayed a linear plot as shown in figures 4.14, 4.15, and 4.16. The skin behaved in the same manner between models III and V. This is shown in figures 4.17 and 4.18. The skin behaves in a non-linear manner the further from the frame it gets, and the frame behaves linearly. This is the reason a non-linear analysis is required when the skin is applied.

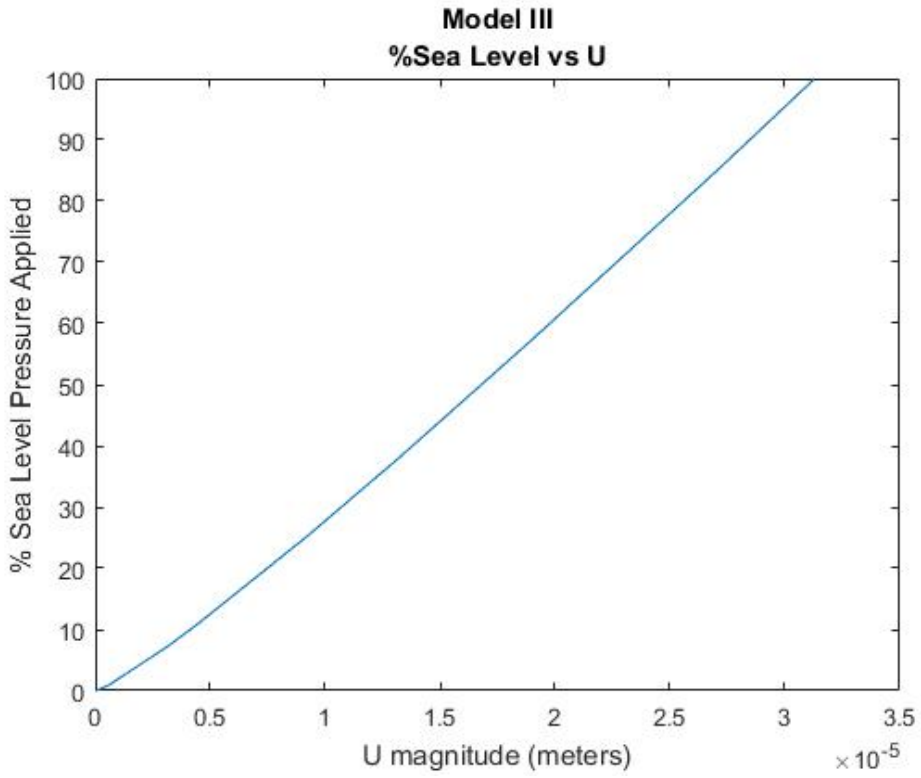

Figure 4.14. Model III (ø=0.3408 m, f/s, 8 mm beams, BC3), Frame Tracking - % Pressure applied vs Deformation

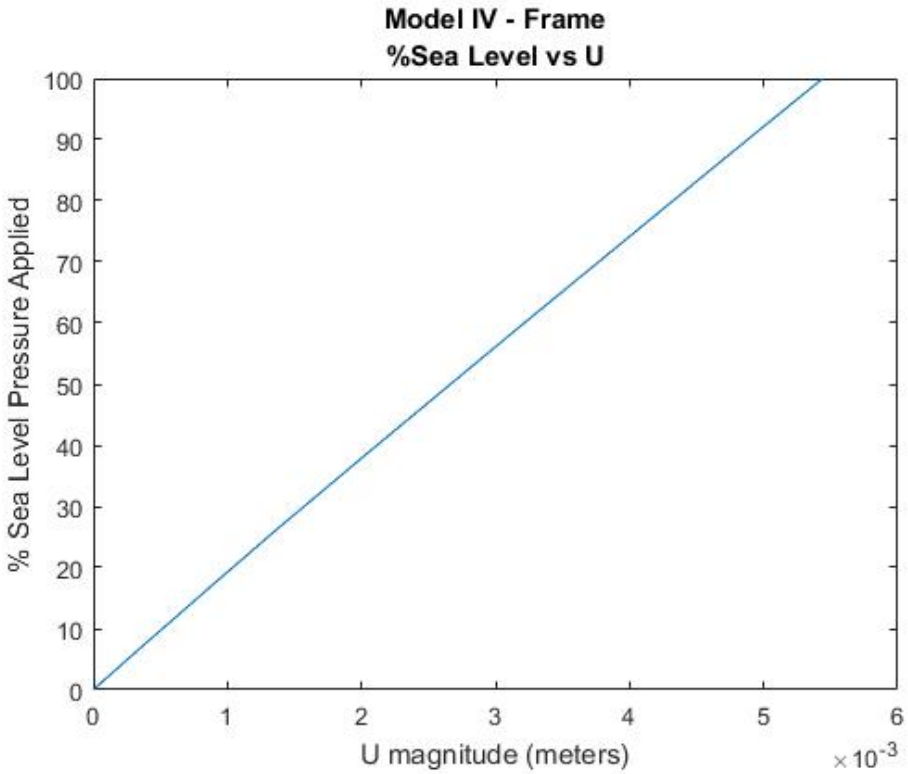

Figure 4.15. Model IV (ø=1.2192 m, frame, 8 mm beams, none), Frame Tracking - % Pressure applied vs Deformation

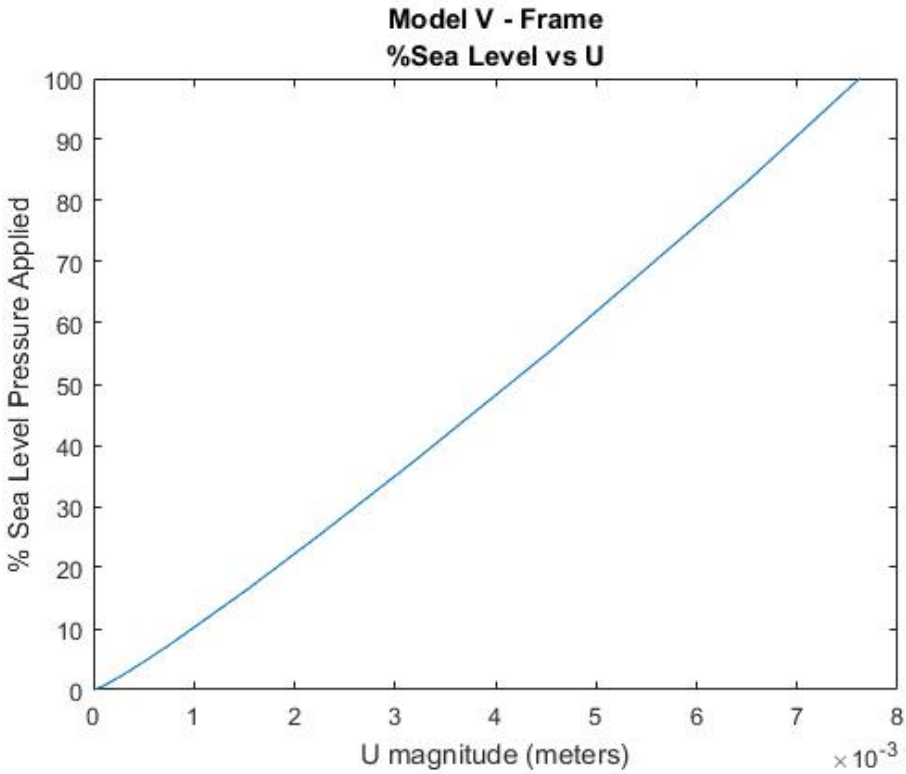

Figure 4.16. Model V (ø=1.2192 m, f/s, 8 mm beams, BC3) , Frame Tracking - % Pressure applied vs Deformation

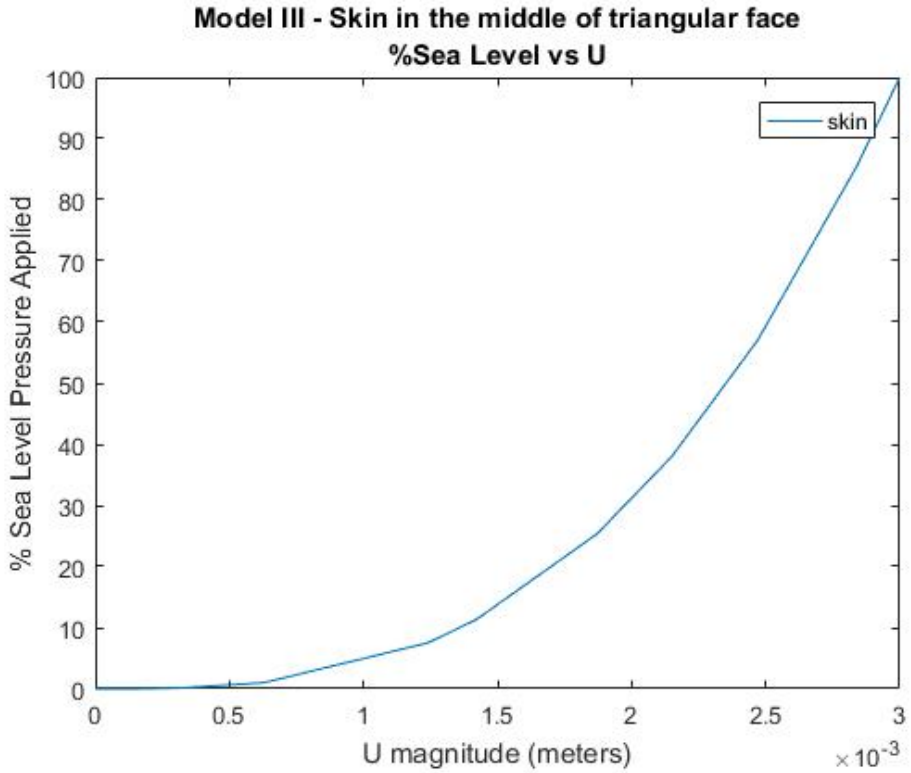

Figure 4.17. Model III (ø=0.3408 m, f/s, 8 mm beams, BC3), Skin Tracking - % Pressure applied vs Deformation

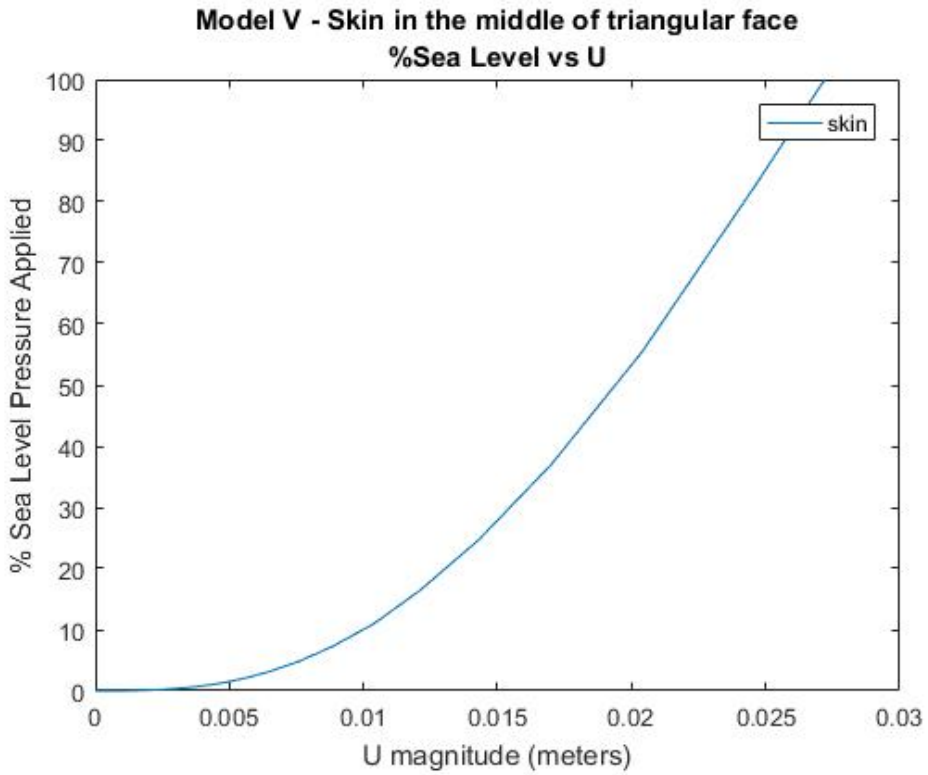

Figure 4.18. Model V (ø=1.2192 m, f/s, 8 mm beams, BC3), Skin Tracking - % Pressure applied vs Deformation

4.3.4 Model IV

Model IV (ø=1.2192 m, frame, 8 mm beams, none) looks at the hexakis icosahedron frame utilizing the dimensions described by Schwemmer's research. The overall frame is 4 ft (1.2192 m) in diameter with beam dimensions constrained by manufacturing constraints, and the use of the CNT composite that has been used in the previous three models. The pressure load was applied in the same method as model I, but this model did not use BCs. The top and bottom node were allowed to translate and rotate freely, similar to model II. The stress field is shown in figure 4.19. The deformation visualization is depicted in figure 4.20.

Using the same materials, but a larger radius structure with larger beam dimensions was able to reduce the maximum stress in the frame from 10.77 GPa as seen in model I to 2.461 GPa. The stress concentrations still occur at the vertices with the

minimum stresses appearing to occur at approximately one-third, and two-thirds the length of the beams. Unlike model I, the maximum stress for the frame at these dimensions is 42% below the yield limit of the material. The lack of boundary conditions did not appear to affect the results. There were no rotations during incrementation, and the results were symmetrical as seen in model V when analyzing the frame by its self. The main difference is the fact that the stresses appear to be 31% lower than stresses of the frame in model V. This is most likely due to the fact that the skin distributed the loading slightly more, and that the BCs do increase the maximum stress due to the restrictions in movement. This actually makes model IV to be less conservative than model V and was taken into consideration when designing the air evacuation design. The BCs seem to become more important when the skin is applied, which might be attributed to the non-linearity in the skin when compared to the linearity of the frame.

The deformations are significantly smaller than those of model I, sitting at 5.573 mm vs the 12.05 mm of model I. The maximum displacement is located at the middle of the beams with very small or virtually no displacement at the vertices. Compared to model V's frame, the displacements in model IV are 33.3% smaller. This means that model IV is less conservative in terms of stresses, and in terms of the displacement. The lack of BCs did not cause any rotations or movements of the model, indicating that the frame just experiences larger deformations in the beams.

The overall W/B ratio of the frame was 0.7528. The W/B of the skin and frame for model V was 0.7654. The frame is the main source of the weight and changes significantly based on the size of the structure.

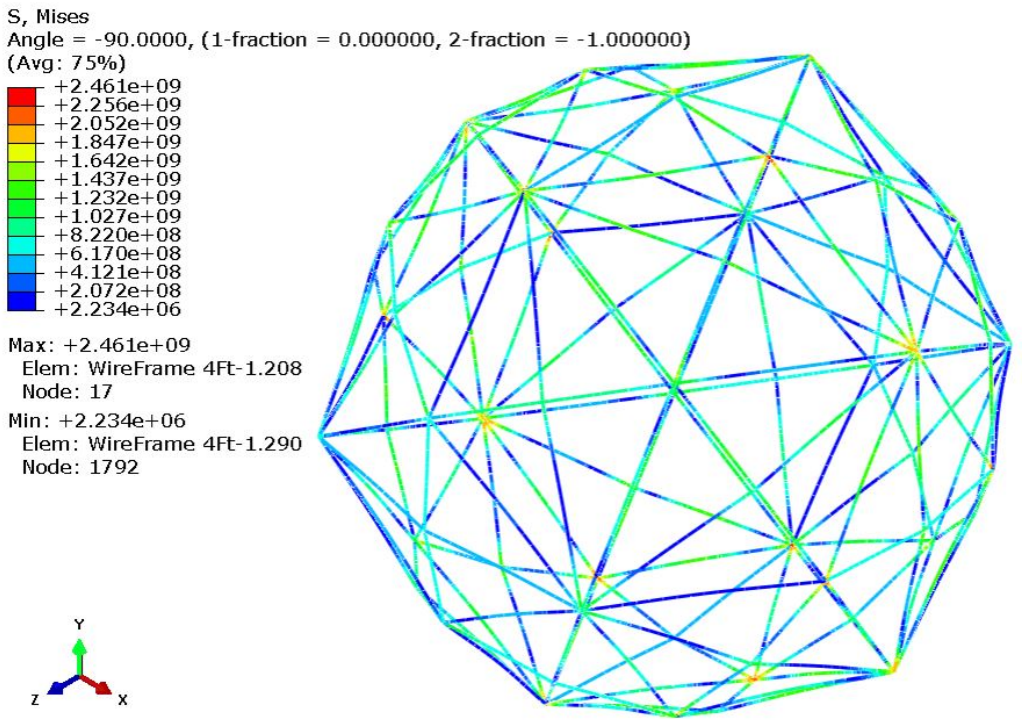

Figure 4.19. Model IV (ø=1.2192 m, frame, 8 mm beams, none), von Mises stress visualization of 1.2192 m hexakis icosahedron frame

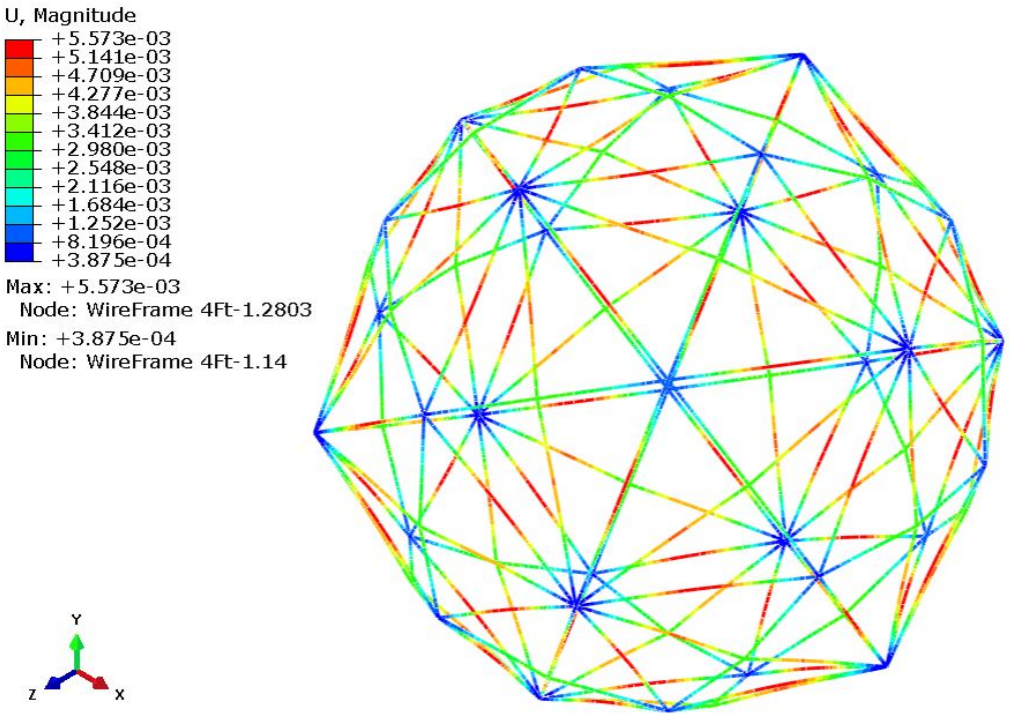

Figure 4.20. Model IV (ø=1.2192 m, frame, 8 mm beams, none), Deformation visualization of 1.2192 m hexakis icosahedron frame

4.3.5 Model V

Model V (ø=1.2192 m, f/s, 8 mm beams, BC3) incorporates model IV, but adds the graphene skin to the structure for a complete analysis. This model was created in the same manner as model III and produced results similar to the results shown Schwemmer's research. The W/B ratio of this structure came out to be 0.7654, which is small enough to enable a light payload. The stress field for both the frame and the skin had maximum stresses of 3.38 GPa and 22.1 GPa respectively. These stresses are both under the yield stress for their respective materials. The stress visualization is shown in figure 4.21. The von Mises stresses are very similar to those shown in model III, with the exception that the stresses are slightly more distributed resulting in smaller concentrations at the beams conjoined to the vertices. This model does have stresses two times as great as model III, but again are all within the yield limits. Model V was analyzed with respect to the principal and shear stresses found in the S11, S22, and S12 directions as well. Their results are shown in figures 4.22, 4.23, and 4.24. The S11 principal stress gives the maximum stress experienced by the structure at 23.1 GPa, while S22 is supposed to give the minimum stress or maximum compressive stress, it could not due to the element type of the membrane. There is no bending stiffness and therefore runs to infinity when computing the S22 value. The third principal stress S33, gives a value of zero due to the element type as well. S12 or the shear stress did produce results, with a maximum shear stress of 11.32 GPa as seen in figure 4.23.

In addition to the stresses, the deformations were analyzed for this model as well. The magnitude of the deformation can be seen in figure 4.25. The overall deformation is 27.37 mm which is the largest deformation seen so far when compared to the other models, with the exception of model II. The deformations appear to be mostly in the skin with the maximum frame deformation only being 7.8 mm in the beams. This

shows that the deformation in the beam is smaller than the actual diameter of the beam indicating the frame behaves in a linear manner, which was also point out in the model III section. The deformations in the 1, 2, and 3 directions were all looked at, and line up nicely with each other, with the maximum displacement in each being the same at 26.59 mm.

Model II (ø=0.3408 m, f/s, 1 mm beams, none), III (ø=0.3408 m, f/s, 8 mm beams, BC3), and V (ø=1.2192 m, f/s, 8 mm beams, BC3) were compared to one another by probing values in each model and comparing them. Table 4.3 summarizes the stresses and displacements for each model in the middle of the skin of one of the triangles and in the middle of the beam for the same triangle. The results showed increased stresses and displacement between the two models, with very small difference between the displacements where the frame is located. The skin is displacing significantly more in the 4 ft (1.2192 m) model than the 1 ft (0.3048 m) model. Table 4.4 has summarized the three models with the frame and skin and identified the maximum stress in the frame and skin along with their corresponding yield stress to identify whether or not each model would have survived. Model II failed with both models III and V surviving in terms of the quasit static analysis. Model III however did not have the W/B ratio needed for sustained buoyancy.

Table 4.3. Stress/Displacement for the middle of the skin and beam of a single triangle of the hexakis.

Model	Location	Stress (Pa)	Displacement (m)
Model II	mid skin	2.01E+09	1.76E-02
	mid beam	3.83E+09	1.66E-02
Model III	mid skin	8.00E+09	3.02E-03
	mid beam	9.78E+09	3.33E-05
Model V	mid skin	1.90E+10	2.70E-02
	mid beam	2.21E+10	4.79E-03

The models showed linear results in the frame and non-linear results in the skin.

All models utilized a non-linear analysis to test this. The frame becomes non-linear when the beam dimensions are too small or the material is too weak, resulting in large deformations and chaotic behavior.

Table 4.4. Summary of max stress compared to yield stress

Model	II	III	V	Yield Stress (Pa)
Skin Stress (Pa)	1.04E+10	9.79E+09	2.21E+10	5.00E+10
Frame Stress (Pa)	3.85E+09	1.01E+08	3.38E+09	3.80E+09
Survive	No	Yes	Yes	

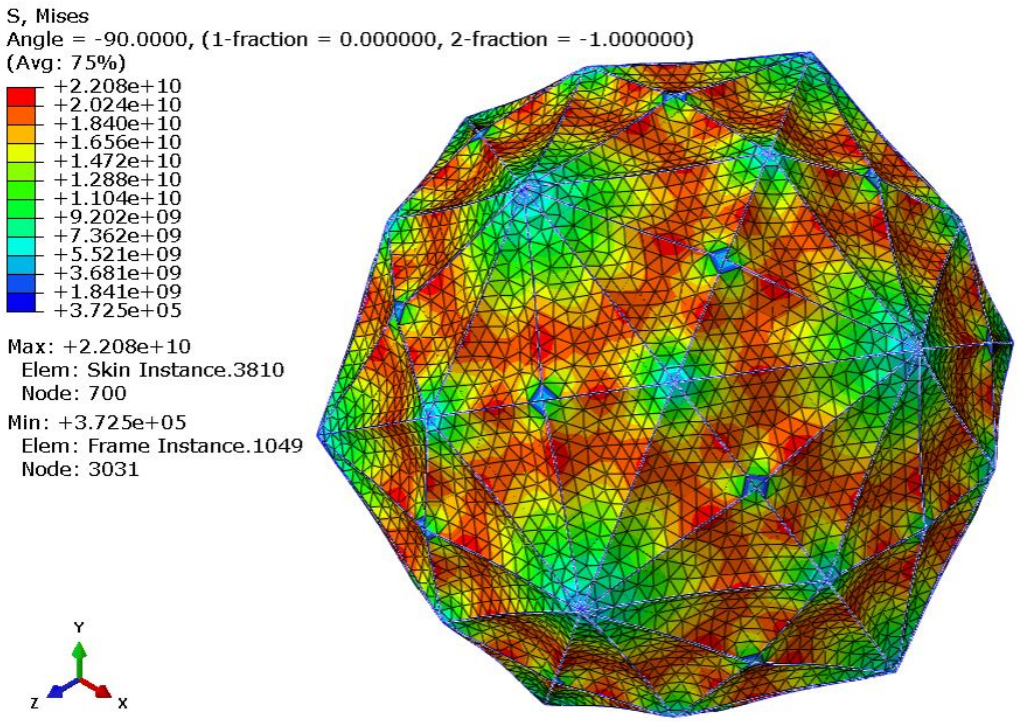

Figure 4.21. Model V (ø=1.2192 m, f/s, 8 mm beams, BC3) , von Mises stress visualization of 1.2192 m hexakis icosahedron

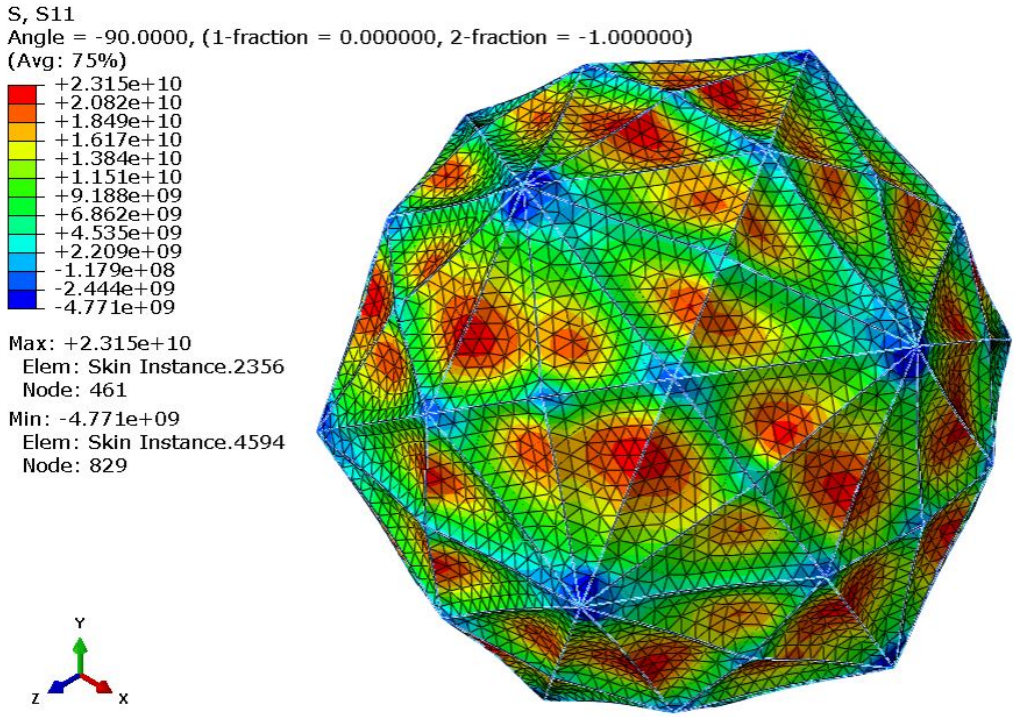

Figure 4.22. Model V (ø=1.2192 m, f/s, 8 mm beams, BC3) , S11 stress visualization of 1.2192 m hexakis icosahedron

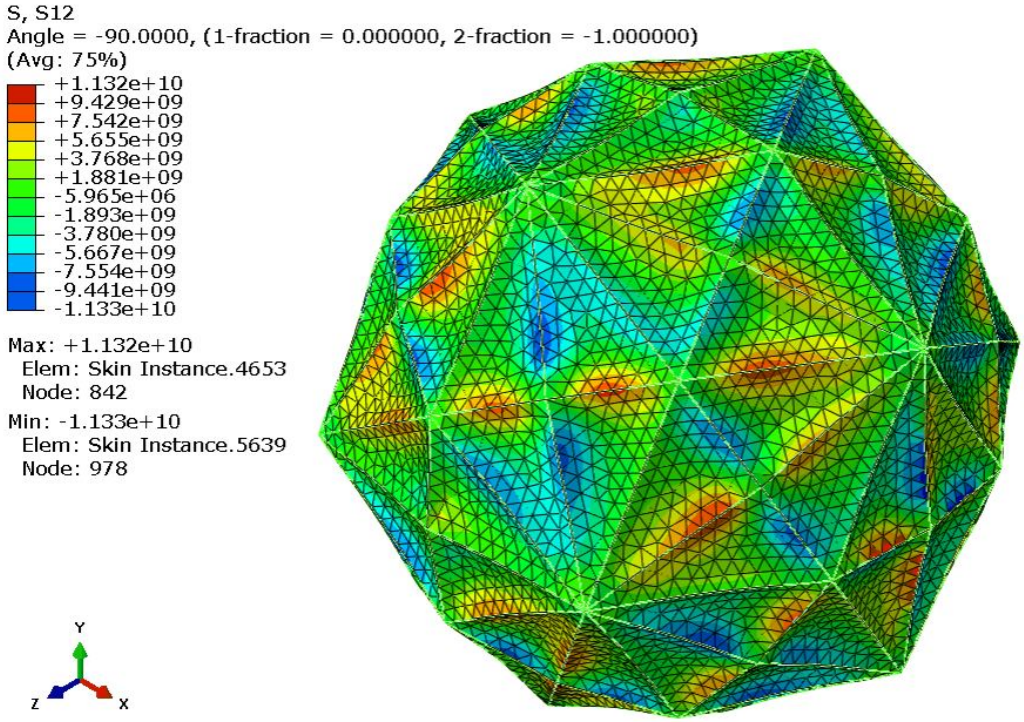

Figure 4.23. Model V (ø=1.2192 m, f/s, 8 mm beams, BC3) , S12 stress visualization of 1.2192 m hexakis icosahedron

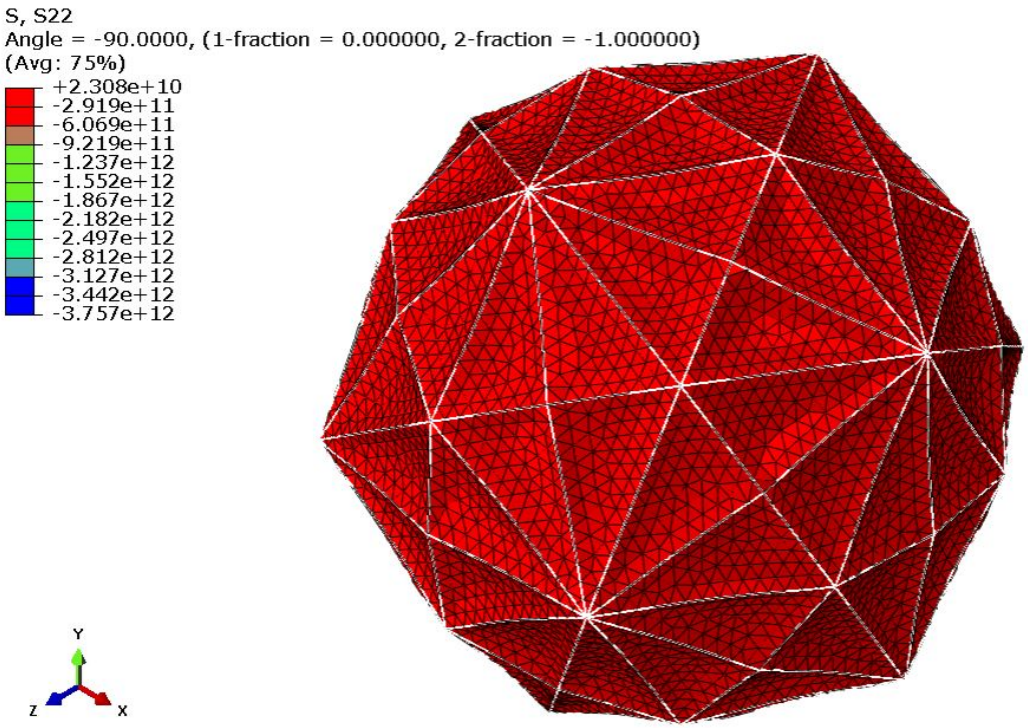

Figure 4.24. Model V (ø=1.2192 m, f/s, 8 mm beams, BC3) , S22 stress visualization of 1.2192 m hexakis icosahedron

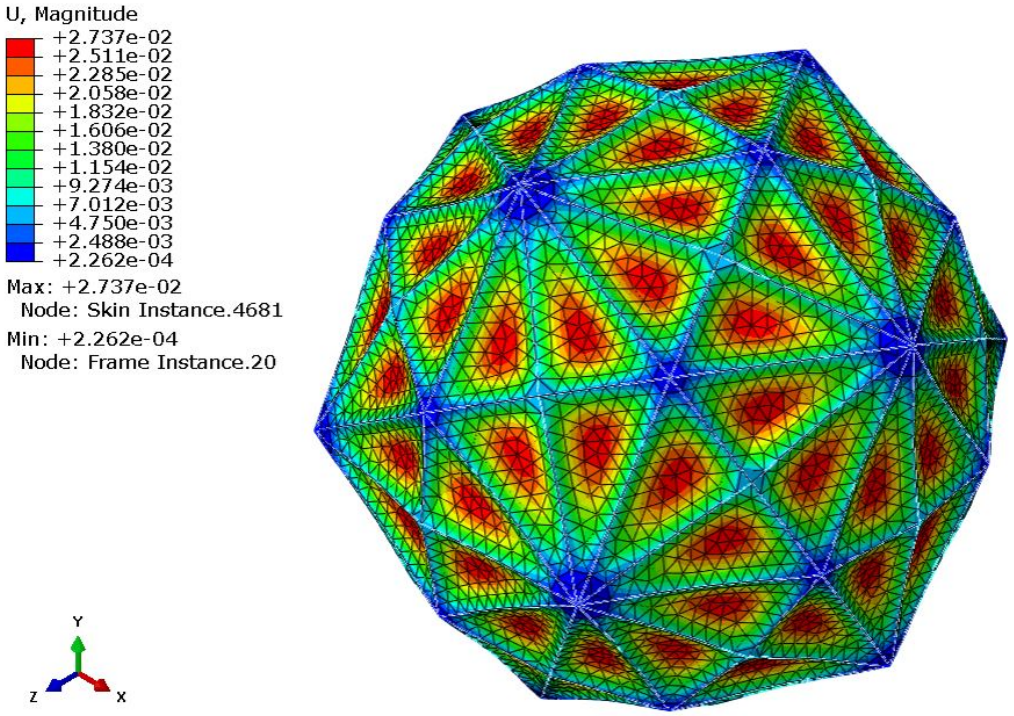

Figure 4.25. Model V (ø=1.2192 m, f/s, 8 mm beams, BC3) , Deformation visualization of 1.2192 m hexakis icosahedron

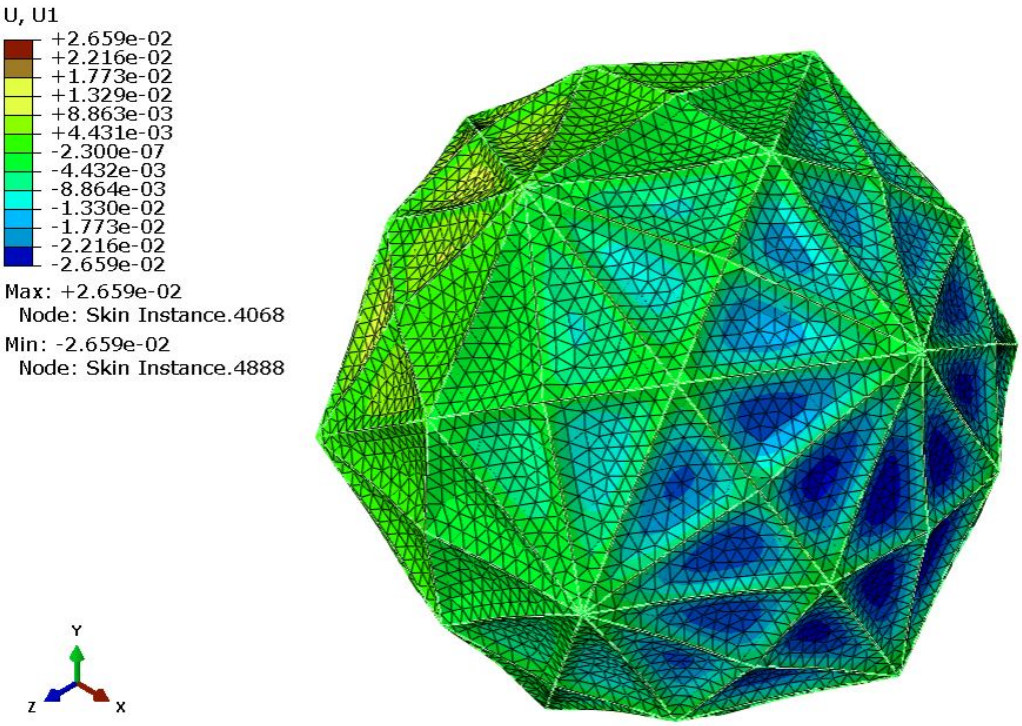

Figure 4.26. Model V (ø=1.2192 m, f/s, 8 mm beams, BC3) , U1 Deformation visualization of 1.2192 m hexakis icosahedron

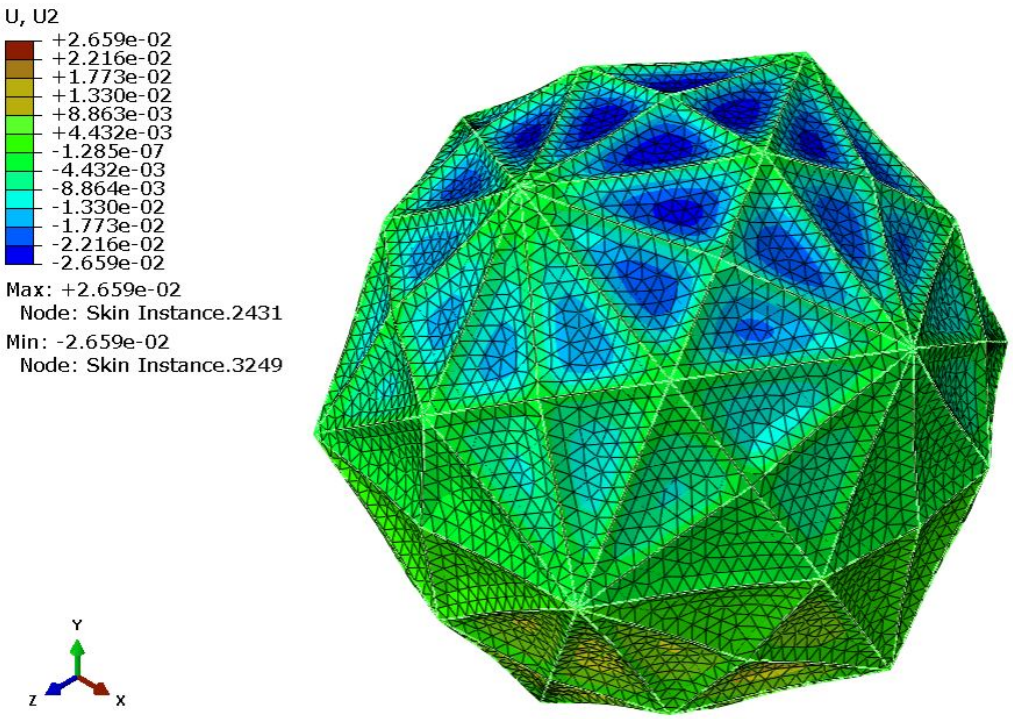

Figure 4.27. Model V (ø=1.2192 m, f/s, 8 mm beams, BC3) , U2 Deformation visualization of 1.2192 m hexakis icosahedron

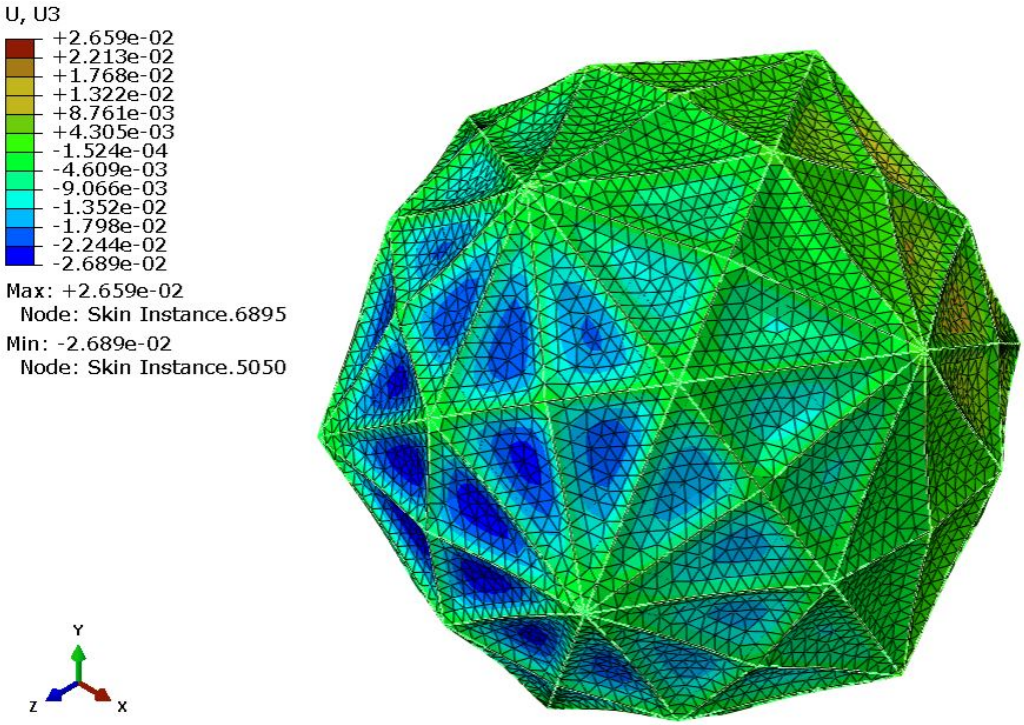

Figure 4.28. Model V (ø=1.2192 m, f/s, 8 mm beams, BC3) , U3 Deformation visualization of 1.2192 m hexakis icosahedron

4.4 Air Evacuation Design and Results

The hexakis icosahedron has only been studied as a finished model, however the act of creating the internal volume is a large component that needed to be analyzed. The next step was to identify this method of evacuating the air and creating a vacuum within the structure to achieve the W/B less than one that is needed for buoyancy. This was done by first analyzing the frame of the hexakis icosahedron for the location in the beams with the least amount of stress, finding the velocity of the fluid the structure can evacuate before chaotic behavior began, using conservation of mass to identify the size of the holes needed for the evacuation, and analyzing the beams with the holes to verify failure does not occur.

The air evacuation design for the hexakis icosahedron is the main research topic for this thesis and has been broken into five steps. The first step was to identify the buckling velocity of the beams through Dowell's equation. The second step was to find the velocity and flow of the fluid that would be used in the evacuation system. The third step was to design the actual geometry of the exhaust system. The fourth step was to analyze the designs in FEA software, and the last step was to identify potential vacuum pumps that could create a partial vacuum for the structure. The following results were all conducted for the 1.2192 m hexakis icosahedron.

4.4.1 Buckling Analysis: Beams and Fluid Flow Through a Flexible Pipe

4.4.1.1 Saada Beam Equation for Buckling

Saada describes the scenario of a beam under a compressive load with an axial load, which is similar to the case of the individual beams in the hexakis icosahedron. The beam will approach the critical load when the value of $KL/2$ approaches the value of $\pi/2$ [25]. The beams will be treated as individual pipes for this buckling

analysis, and the material properties of the CNT/BMI composite will be used. The value of K was computed by calculating the axial force P and the moment of inertia as shown in equation 4.1.

$$K^2 = \frac{P}{EI_3} \tag{4.1}$$

where,

P = axial load - compressive stress multiplied by cross-sectional area

E = Young's Modulus of the material

I = second moment of inertia

Plugging in the dimensions of the 8 mm beam, the material properties of the CNT/BMI composite, and the calculating P from the simplified beam analysis shown in section 4.4.4, the value of $KL/2$ came out to be 0.0025. This came out to be 200% below the value of $\pi/2$ indicating that buckling should not occur in the 1.2192 m hexakis icosahedron with the 8 mm beams.

4.4.1.2 Dowell Fluid Flow Through a Flexible Pipe

Dowell presents an equation that can identify the static buckling of a flexible pipe under fluid flow as shown in equation (4.2) and described in chapter II. Solving for U, will give the velocity that will invoke buckling based on the material and dimensional parameters of the pipe. Using the same material properties of the CNT/BMI composite frame, and calculating the second moment of inertia for the pipe, it is easily shown that the fluid would have to be flowing 167,610 m/s. This is well beyond supersonic flow and shows that any evacuation system designed will most likely not

cause static buckling due to the fluid flow exclusively.

$$\rho U^2 = \frac{EI}{Aa^2} * \pi^2 \tag{4.2}$$

where,

ρ = density of the fluid

U = flow velocity

E = Young's Modulus of the material

I = second moment of inertia

A = area of the pipe

a = length of the pipe

4.4.2 Velocity and Flow

Models IV and V were analyzed near the top and bottom of the structure where the boundary conditions are located. There are ten beams going into a single vertex, where the largest stress concentrations in the frame can be found. The material yield limit of the carbon nano-tubes was 3.8 GPa, with the maximum stress in the frame to be approximately 3.38 GPa. This did not leave a lot of room for extra stress in the frame which would be created by adding holes in the frame to evacuate the air. Holes generally create stress near the center edges equal to approximately 3 times the largest stress in the model [32]. By creating a path along each of the beams in Abaqus and getting a stress profile along the distance of the beam as shown in Figure 4.29, the maximum and minimum stress locations could be identified. Figure 4.29, shows that the minimum stress occurred at roughly 20% and 66% of the beam length. This was consistent with all ten beams having only small variations in the true location of the minimum stress. Knowing this location gives the best placement for the air evacuation system.

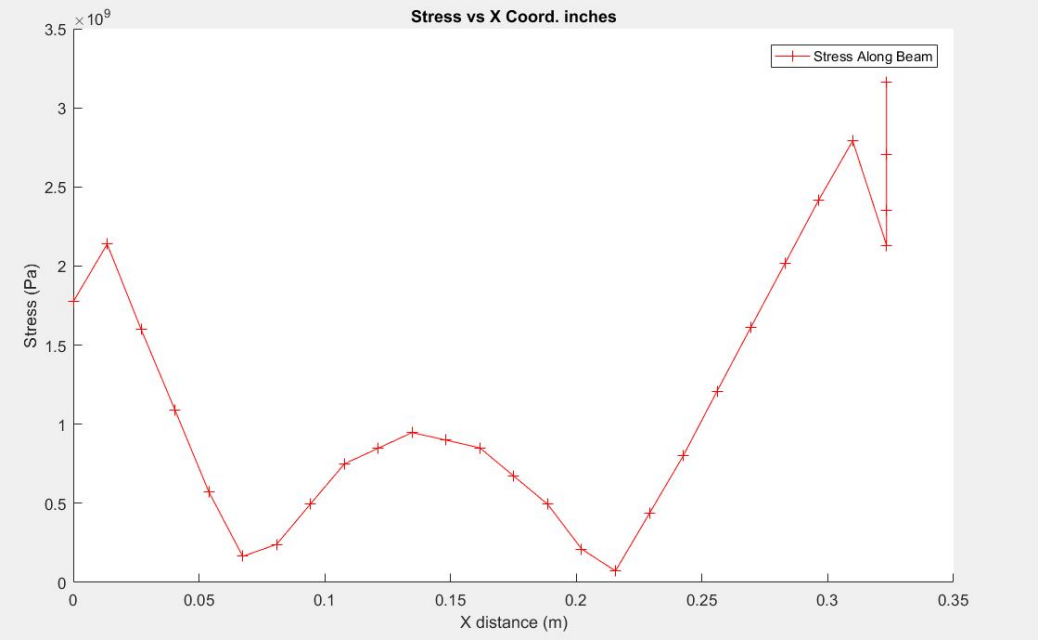

Figure 4.29. Stress (Pa) along true distance of beam (m)

The next step was to identify the parameters of the air evacuation system that would be used. The velocity of the fluid being evacuated is dependent upon the hole sizing and the pump used to evacuate the air. To analyze the model with the most conservative outlook, a velocity was identified based on previous research by Just, which identified a load rate of 4.0 MPa/s causing unstable chaotic behavior known as snapback [6]. Knowing the load rate, the time to remove the pressure would simply be a ratio of the air removed or pressure removed at a given time vs the load rate. Solving equation (4.3) for x, gave a time of 0.0253 seconds. Using this time, a flow rate can be identified to be 37.5494 m^3/s which is simply the volume of the hexakis icosahedron divided by the time. The flow rate for an orifice can be related to the velocity through the orifice by equation (4.4) [33]. Using the flow rate and the predetermined exhaust area, which is a slightly smaller pipe (radius = 0.006 m), the velocity was calculated to be between 3.3200e+05 m/s and 6.5100e+05 m/s depending on the C value used. The C value is based on the geometry of the orifice and can be considered to be 0.51 for a cut off surface, or 0.91 for a curved surface.

These velocities are extremely high and were verified by using a simple correlation between force and the change in momentum. Using Newton's second law a velocity equal to 1.1338E+05 m/s was found. These velocities would not be achieved with a vacuum pump light enough to be attached to the hexakis icosahedron, or even desired. Therefore, the velocity was calculated based on the flow of the air through an orifice of the prescribed geometry using the pressure head at sea level and a vacuum. The head can be calculated using equation (4.5) [34]. Knowing the head, the new flow rate can be calculated and placed into equation (4.6), which is a modified version of equation (4.4) with pressure head replacing velocity, to get the flow rate of the system. This can then be placed back into equation (4.4) to solve for velocity, which resulted in 44.4 m/s.

$$\frac{0.101325MPa}{x} = \frac{4MPa}{1s} => x = 0.0253s \tag{4.3}$$

$$Q = AVC \tag{4.4}$$

where,

Q = flow in cubic meters per second

A = area of the orifice in square meters

$\mathbf{V}$ = velocity of fluid in meters per second

C = contraction coefficient

$$Pressure(psi) = \frac{Head(h) * SpecificGravity(sg.)}{2.31} \tag{4.5}$$

$$Q = 25 * A * C * \sqrt{h} \tag{4.6}$$

Using this velocity a Reynolds number could be calculated for a single pipe with

standard sea level properties of air. This number came out to be 1.1425e+06. Turbulent flow typically begins at 5e+05, but as mentioned in chapter II, the flow can be turbulent in a pipe above 2600. This means that the worst case scenario would generate turbulent flow. This simply means the flow would not be uniform and can result in larger friction throughout the beams. This will need to be taken into account in future research if a Computational Fluid Dynamics (CFD) analysis is ever conducted.

4.4.3 Design

There were two designs that were developed for this research as described in chapter III. The first design was created and analyzed which then led to the second design. To create these designs the previous results shown for the velocity and flow were needed. This drove the sizes and dimensions of the air entrance system. The results from the first design were then incorporated into the second design. The first design is shown by the Computer Aided Drafting (CAD) representation in figures 4.30a, 4.30b, and 4.30c. The second design is represented in figure 4.31. These figures show the complete vertex with all 10 beams and the complete air evacuation system. The FEA models only represent a portion of this system, but attempt to give accurate results due to the symmetry of the structure. These designs are further described and talked about in the analysis and results section that follows.

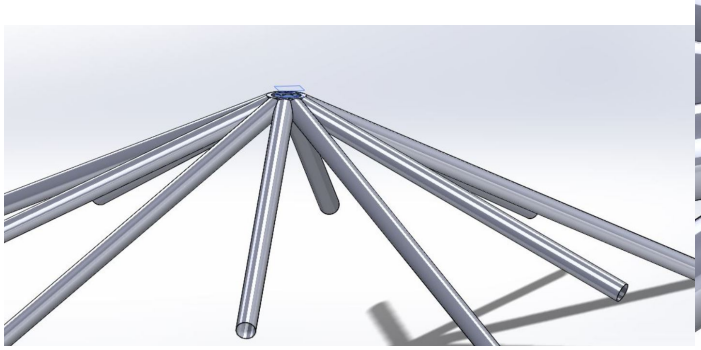

(a) CAD-View of modeled exhaust system

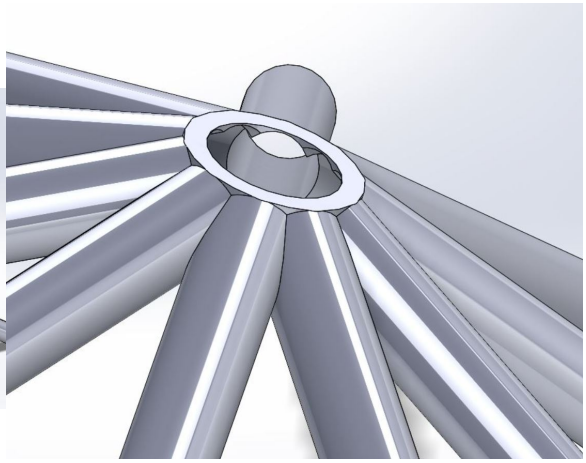

(b) CAD-View of exhaust hole and beam profile

(c) CAD-View of exhaust hole and beam profile

Figure 4.30. Air evacuation design #1

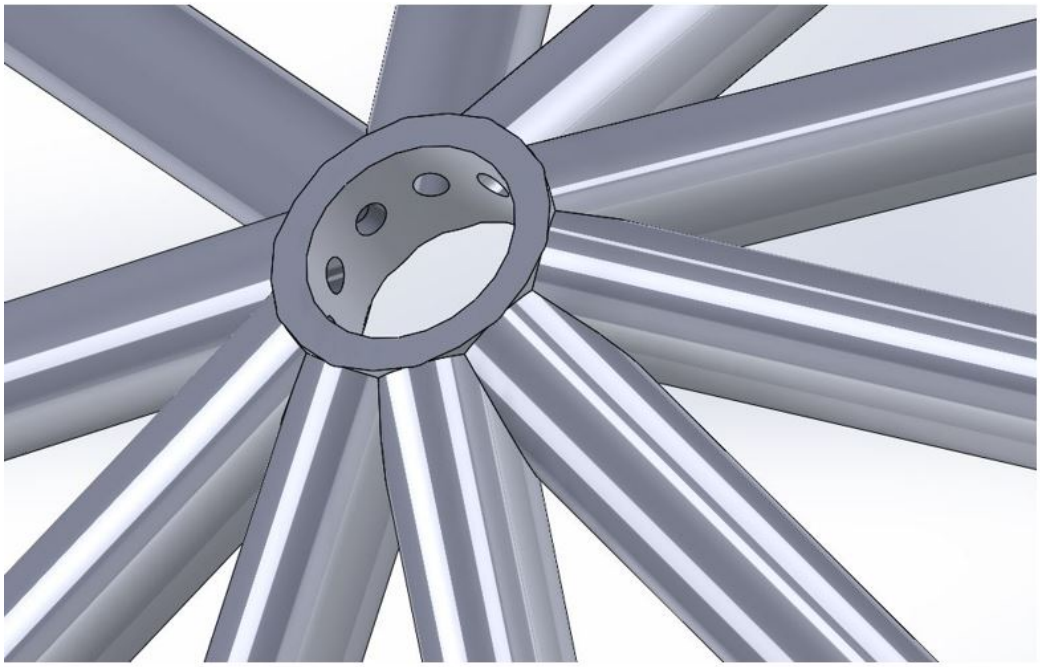

Figure 4.31. Air evacuation design #2

4.4.4 Analysis and Results

The size of the entrance holes needed for the exhaust were then calculated based on the identified fluid velocity. Utilizing conservation of mass, the velocity, density and area of the exit hole were known, the same velocity would be used for the entrance, which only left the area to be calculated. Using ten beams, and an exhaust radius of 0.006 m gave a radius of 0.0019 m for the entrance holes on each of the beams. The holes were then placed at the point of minimum stress nearest the top side of the hexakis icosahedron.

The main models used for the entire structure were made of wire beam elements which could not accurately represent the effects of the air evacuation system. This resulted in the creation of another model that could represent the stresses occurring on the beam, but accurately depict the effects of the air evacuation system. One of the 10 beams was analyzed near the top side of the structure. The resultant force

distribution, stress distributions, and loading were all collected in order to recreate a single beam with similar loading and stress patterns. A single pipe from the hex-akis icosahedron was created in Abaqus and constrained from translating in all three directions at both ends to simulate the vertex stress field. Model IV utilized a concentrated force coupled to a single triangle of beams to represent the skin pressure. This force is distributed evenly among the nodes and therefore can be seen as a distributed force. Multiplying the force by the length of the beam gave the maximum magnitude of the force (1,091 N). Each beam is essentially influenced by two forces, one from each side of the beam. This can be seen in figure 4.32.

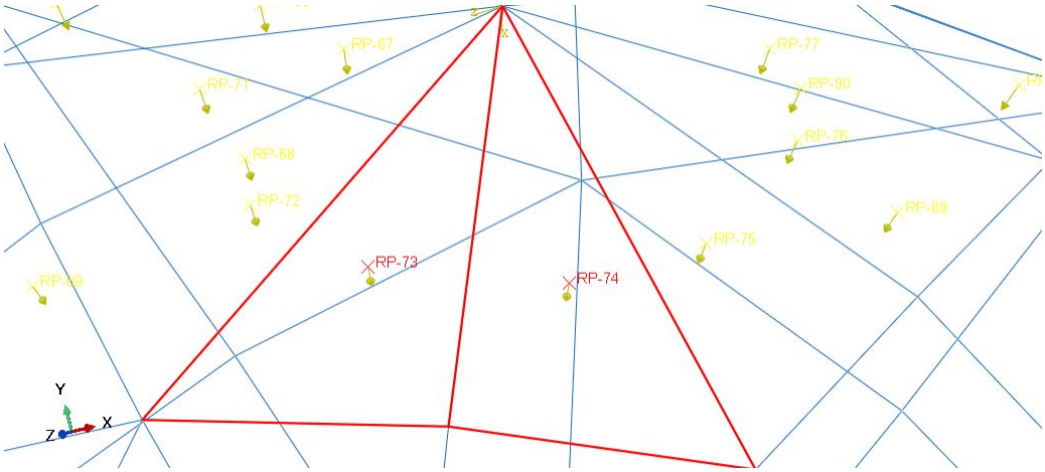

Figure 4.32. Beam being influenced by forces on both sides

The resultant forces from the model showed a triangular distribution, and was modeled as such with concentrated forces placed at 2/3 the length of the beam on each side of the mid node on a 3-D pipe model. This resulted in stresses similar to that of the full scale model for the single beam, however there were stress concentrations or singularities created due to the concentrated forces. The model was changed to utilize a pressure force along the length of the beam. In order to maintain a similar stress profile, a total force option was used in the pressure menu of Abaqus. This takes the total force encountered and turns it into a distributed load. With baseline results, an

exhaust hole and an entrance hole were added to the 3-D pipe and resulted in failure as the maximum stress was greater than the material yield stress. The failure points occurred at the exhaust hole where the pipe was too thin to handle the stresses due to the boundary conditions at that point, see figure 4.33a. The entrance hole had very small stresses on the order of 3e+06 Pa, with maximum stress near the edge at 1.6e+09 Pa, which was well below yielding.

More material needed to be added to the exhaust hole as this was the location of maximum stress in model IV. An analysis of the mass of the system was completed to identify how much material was removed from the overall system due to the holes. This identified how much mass could be added to the exhaust hole before (W/B) started to become affected. A total of 1.03E-03 kg was removed from the system, and 7.27E-04 kg was added. The added mass can be seen in figure 4.34a. The maximum stress experienced due to the added mass was 3.6E+09, which falls below the yield stress of the CNT composite used, but only by 11.7%. The maximum stress did not occur near the exhaust hole, but rather near the loading location.

The problem with the simplified model remains with the fact that 10 beams are conjoining on a single point. This would slightly alter the finalized geometry of the exhaust. To identify the true geometry of the exhaust system, the top portion of the full model was created in Dassault Systémes' Computer Aided Drafting (CAD) software Solid Works. The same concept used in the simplified beam model was generated and can be seen in figures 4.30a, 4.30b, and 4.30c. The geometry was slightly different than the one analyzed.

This led to the development of a second air evacuation design and analysis. The geometry of the interactions between the 2 beams on each side of the beam would create weak points where there was less material and sharp concentrations. This needed to be captured by the analysis. Another issue was the fact that the entrance holes on

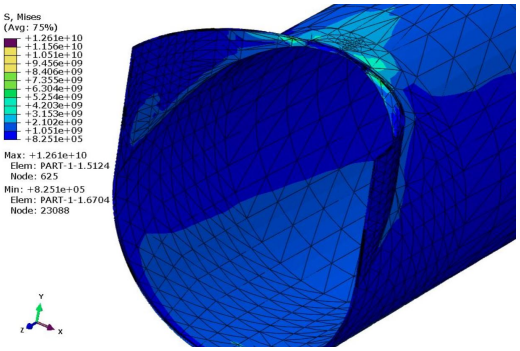

(a) Exhaust hole stress concentrations

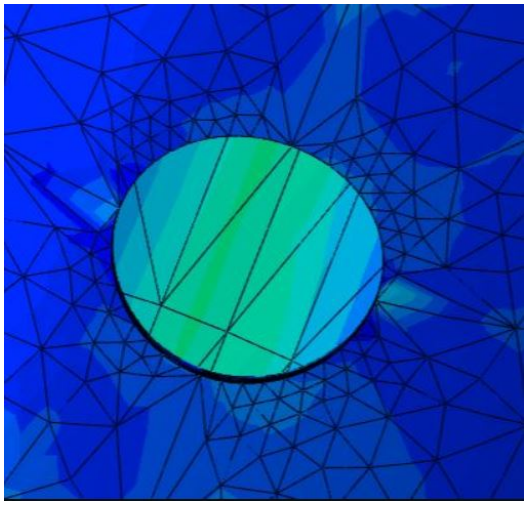

(b) Entrance hole with no stress concentrations due to placement

Figure 4.33. Stress field for air evacuation system

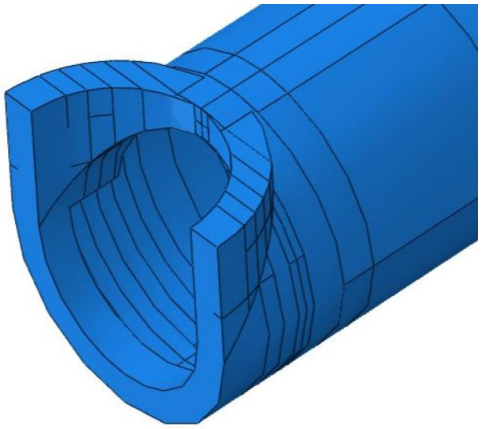

(a) Added mass to exhaust hole location

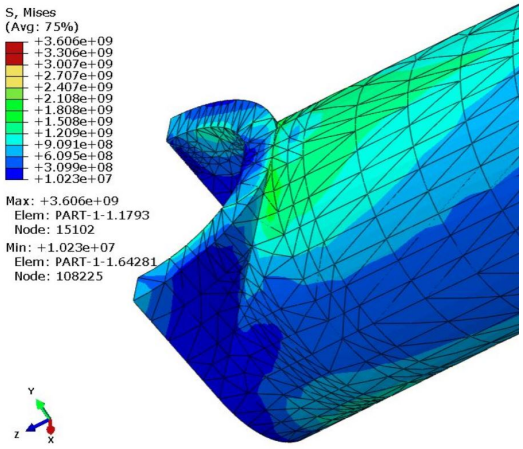

(b) Stress field at exhaust hole location

Figure 4.34. Exhaust hole analysis

the bottom of the beams could be introducing vibrations or counter productive forces on the beam as the air was being evacuated. To avoid these problems the second air evacuation design consisted of a single exhaust hole going all the way through the vertex. There were no entrance holes on the bottom of the beams, instead an orifice was placed at the end of each beam to evacuate the internal air of the beams. This can be better seen in figure 4.31. To analyze this design the 10 beams were reduced to 3 as described in chapter III. The model was run in Abaqus and the von Mises stresses were analyzed. Figure 4.35 shows the stress visualization for the simplified model with the maximum stress being 3.484 GPa. This is a 3.3% decrease in stress when compared to the first model, indicating that the other beams did indeed play a role in the strengthening of the structure and needed to be accounted for. The maximum stress is again under the yield limit of the material indicating success, however the safety factor for the entire model is now down to 1.09 versus the 1.124 before the air evacuation system. This design works, however when accounting for manufacturing defects and material isotropy the structure may fail. A stronger material may need to be identified in order to increase the safety factor and produce this structure consistently in a manufacturing setting.

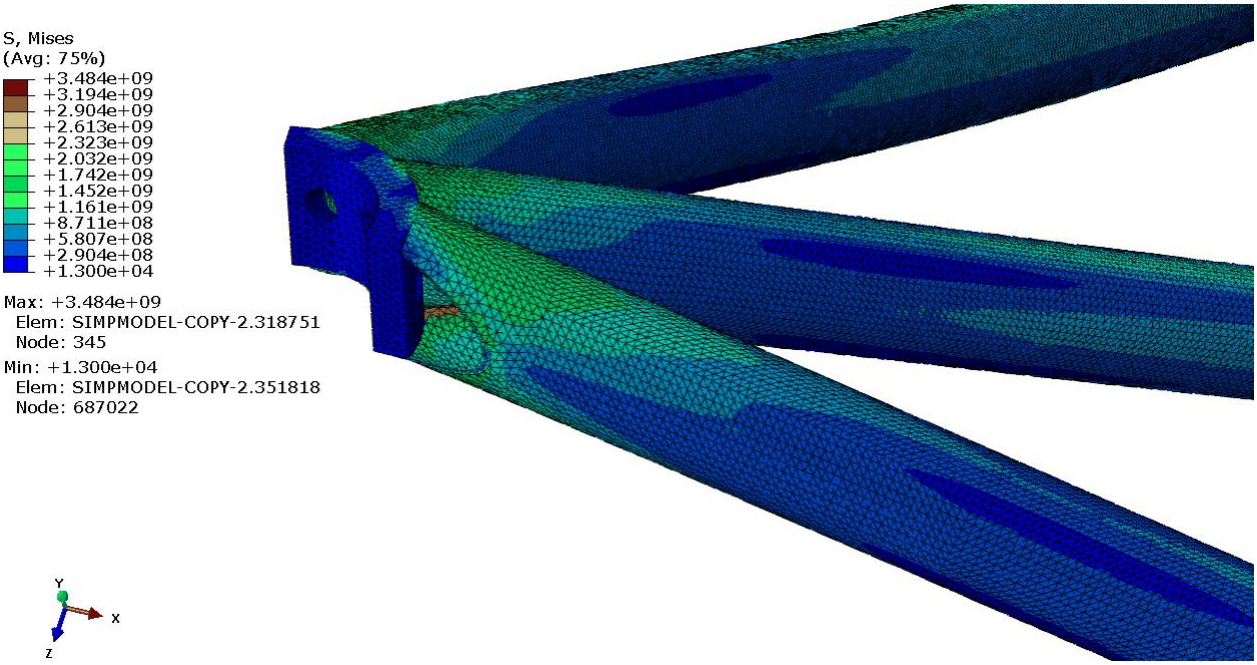

Figure 4.35. von Mises Stress Analysis of air evacuation design #2

Both air evacuation designs were also tested for linearity. The point of maximum deflection was analyzed and the % pressure applied vs the deformation was plotted. The models used non-linear analysis, and still resulted in linear results. This is consistent with the frame analysis of the previous models and shows the accuracy of these simplified models. The plots are shown in figures 4.36 and 4.37. The maximum deformations of these models were 2.7 and 2.91 mm respectively, which are both 90% smaller than the radius of the beam.

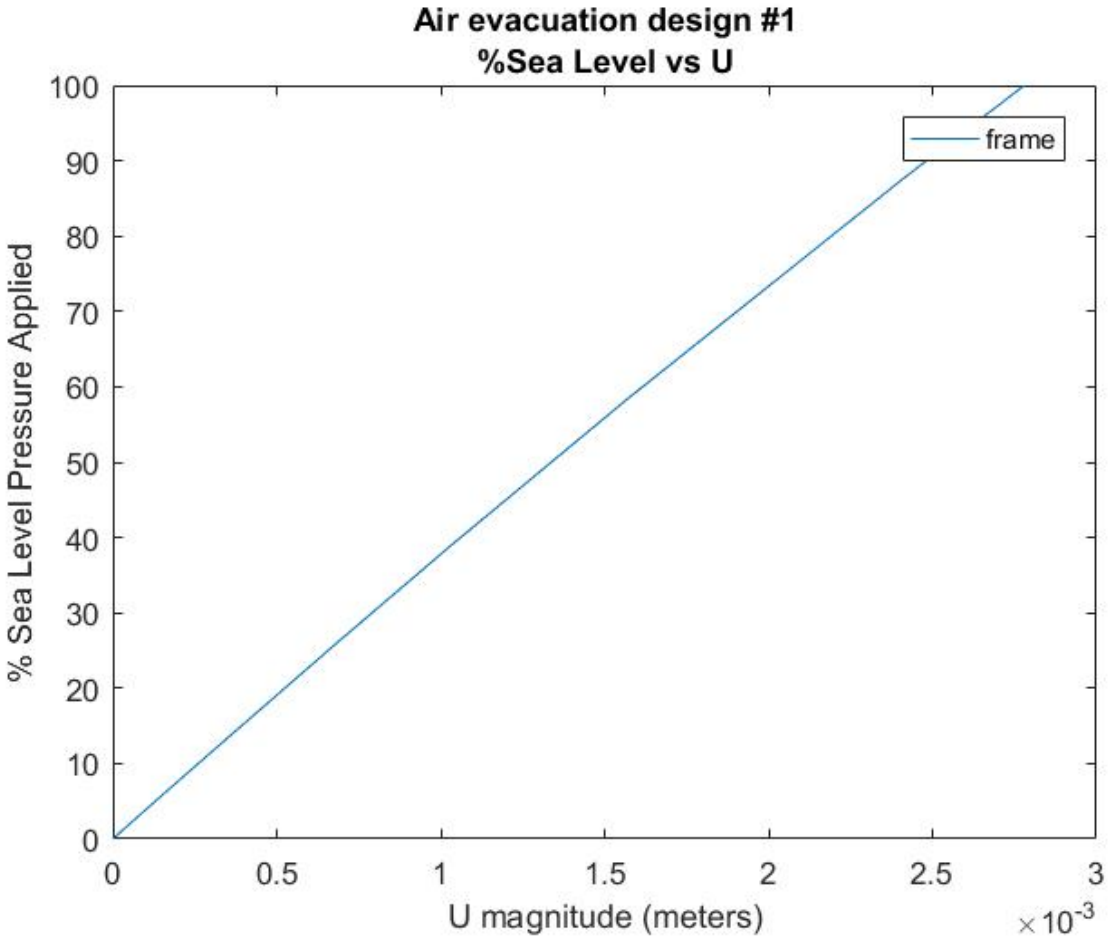

Figure 4.36. Linearity Analysis of air evacuation design #1

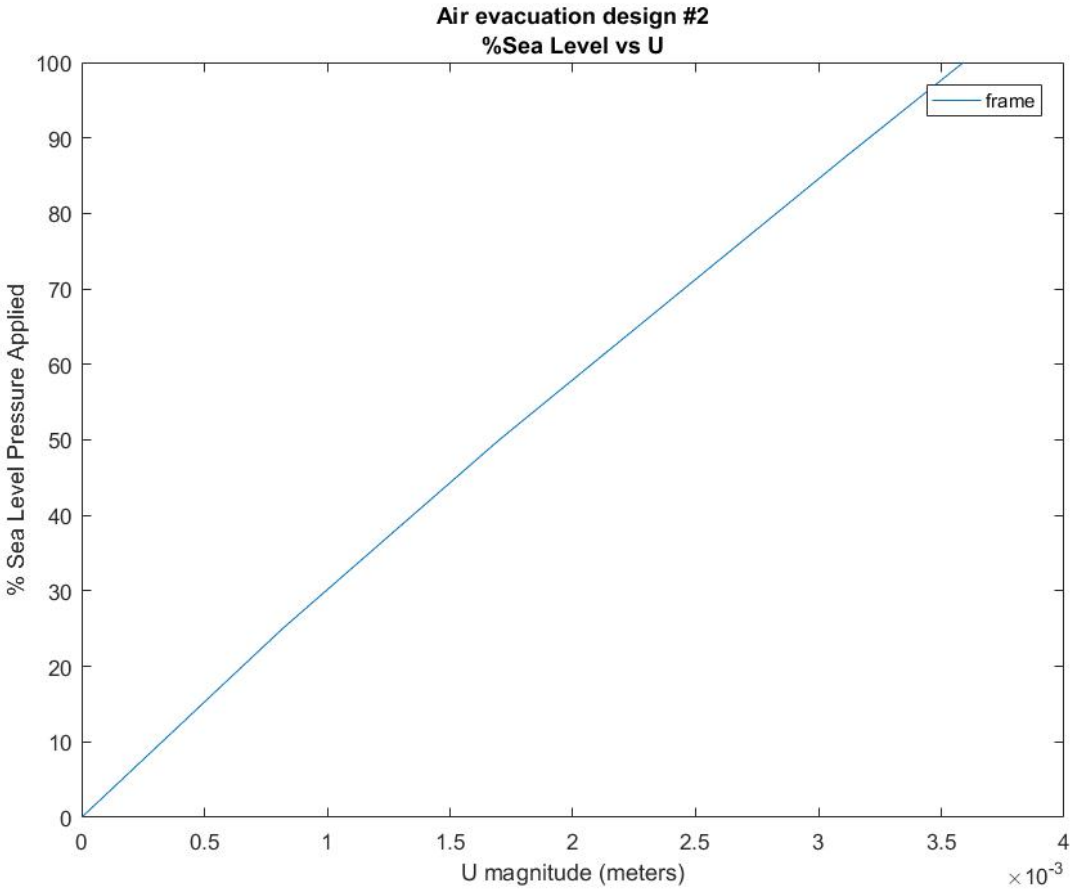

Figure 4.37. Linearity Analysis of air evacuation design #2

4.4.5 Vacuum Pump Result

The size of the vacuum pump depends on two things: how much of a vacuum is actually needed, and how much fluid needs to be pumped out. An ideal vacuum is not really practical and the best that can be achieved would be a partial vacuum. Vacuum pumps are broken into different groups: rough, coarse, and fine. The majority of vacuum pumps in the market are rough, indicating that they do not maintain a consistent vacuum and often times not even close to it. The fine pumps can get as close as one micron. The second criteria needed was the fluid flow, typically characterized by mass flow in cubic feet per minute, CFM. This was identified previously and is as simple as finding a pump with an equal or larger CFM.

The goal is to get as close to a vacuum as possible so a vacuum pump near 29.92 in.-Hg or 0 Torr is needed. This value is the theoretical maximum vacuum. There are very few pumps that actually get this close and the best one that was found was at 29.91 in.-Hg or around $10^{-}12$ Torr for ultra high vacuums. The volumetric flow rate calculated previously was 13.4 CFM, which correlated to the given exhaust area and velocity of 44.4 m/s. There are several pumps that could meet this criteria, but one identified specifically is the Welch Vacuum 1397B-01. This vacuum can achieve a maximum pressure of 1E-04 with a flow rate of 17.7 CFM. This is an industrial pump and could not be attached to the structure. The vacuum would have to be created and then sealed to utilize this pump. Another option is to ignore the CFM needed as this is the worst case scenario of the exhaust hole being left open. Ignoring the required CFM a smaller pump that could potentially be installed on the structure may be used to maintain the vacuum. The piCHIP by PIAB makes small light weight vacuum pumps capable of producing a maximum pressure of 92 kPa. This is only 9.64% below a perfect vacuum at sea level pressure. The rate at which it produces this vacuum is significantly smaller and several of these may have to be used.

4.5 Payloads

The air evacuation design added 9 grams of mass to the overall system, leaving 91 grams for any other payloads that need to be added. This concept was initial designed for Intelligence, Surveillance, and Reconnaissance (ISR) purposes, but could be applied for weather monitoring, communication networking, or several other domains. The hero5 black is a Commercial off the Shelf (COTS) high resolution camera weighing 87 grams allowing the structure to work as an ISR device. Solar sheets can weigh as little as 5.2 grams for a square meter and produce 120 watts. There are several other possible combinations available in private and commercial sections to accommodate the 91 grams left for a payload and meet a slew of operations. Another possibility is to connect a series of hexakis icosahedrons together to carry even more weight and act a constellation if needed.

4.6 Summary

The hexakis icosahedron can survive as predicted by Schwemmer, using a 4 ft (1.2192 m) diameter, CNT composite frame, and graphene skin. Maximum stresses in this structure were well below the yield limit of the material for the skin and under the yield limit for the material of the frame with a safety of factor of 1.124. In order to build the structure an evacuation method needed to be created. Developing simplified models to resemble the structure and apply the air evacuation method resulted in failure until the exhaust hole was reinforced, at which point two evacuation designs show potential. The maximum stress in air evacuation design #2 survived, without exceeding the yield limit of the material and with a safety of factor of 1.09. The results have been summarized into tables 4.5 and 4.6.

Table 4.5. Hexakis icosahedron complete results

Model	I	II	III	IV	V
Skin	None	Attached	Attached	None	Attached
BC	3	None	3	None	3
Diameter - ft (m)	1 (0.3048)	1 (0.3048)	1 (0.3048)	4 (1.2192)	4 (1.2192)
W/B	0.3389	NA	11.9286	0.7528	0.7654
Dimensions					
r_{beam} (mm)	0.955	0.955	8	8	8
t_{beam} (mm)	0.0477	0.0477	0.2	0.2	0.2
t_{skin} (mm)	0.012216	0.012216	0.0005	0.0005	0.0005
Frame					
Max Displacement (mm)	12.05	213.1	0.00354	5.57	7.8
Max von Mises Stress (GPa)	10.77	9.41	0.111	2.461	3.38
Safety Factor	0.35	0.40	34.23	1.544	1.12
Skin					
Max Displacement (mm)	-	213.1	3.082	-	27.4
Max von Mises Stress (Pa)	-	6.4	9.786	-	22.08
Safety Factor	-	7.812	5.12	-	2.264
Survive	No	No	Yes	Yes	Yes
Float	Yes	-	No	Yes	Yes

Table 4.6. Air evacuation complete results

Air Evacuation Design	I	I (modified)	II
r_{beam} (mm)	8	8	8
t_{beam} (mm)	0.2	0.2	0.2
$r_{exhaust}$ (mm)	6	6	6
$t_{exhaust}$ (mm)	0.2	2	4
r_{intake} (mm)	1.9	1.9	1.9
intake location	bottom of beam	bottom of beam	exhaust wall/vertex
Analysis			
Max Displacement (mm)	3.58	3.71	3.56
Max von Mises Stress (GPa)	12.61	3.61	3.48
Safety Factor	0.30	1.05	1.09
Weight Added (grams)	-0.3	0	9.1
Survive	No	Yes	Yes

V. Conclusions and Recommendations

5.0.1 Chapter Overview

Chapters I through IV covered the introduction, background, methodology, and results of the quasi-static analysis of the hexakis icosahedron and the air evacuation system. This chapter focuses on summarizing the key results and the future research needed to develop the hexakis icosahedron or similar structure as a Vacuum Lighter Than Air Vehicle (VLTAV).

This research took an in depth look at the hexakis icosahedron and manufacturing of the structure. There were several small impacts that will be discussed in the results, however the main contributions of this work are shown below.

Contributions:

- The quasi-static comparisons between the icosahedron and hexakis icosahedron.
- The hexakis icosahedron stress field with and without Boundary Conditions (BCs) under a quasi-static loading.
- The analysis of a working hexakis icosahedron.
- The design and analysis of a working air evacuation system.
- The identification of a vacuum pump for both creating the vacuum and maintaining the vacuum.
- The identification of several payloads including a camera that could be used for the 1.2192 m structure.
- The identification of structures that will not work and the main reasons as to why.

5.0.2 Results Conclusions

The main goal of this thesis was to do a quasi-static analysis of the hexakis icosahedron and to develop an air evacuation method that could be manufactured with the structure. To better understand the hexakis icosahedron, a comparison between the icosahedron and hexakis icosahedron was conducted. The key results from that analysis are shown below:

Icosahedron and Hexakis Icosahedron Comparison:

- The hexakis icosahedron produces lower overall stresses when compared to the same structure with an icosahedron design.
- Stresses tend to concentrate at the vertices in the icosahedron, but not so for the hexakis.
- The radius of the beams and the overall radius of the structure play a crucial role in the Weight-Buoyancy Ratio (W/B) of the structure. Comparing both models at the same size and dimensions resulted in a heavier hexakis icosahedron, due to the overall number of beams.
- The hexakis icosahedron can have much smaller beam radii, compared to the icosahedron for the same material properties. This allows the hexakis to utilize a wider assortment of materials than the icosahedron due to the increased stiffness, but the manufacturing constraints of the materials themselves are still the limiting factor.

The next analysis focused on the hexakis icosahedron under a quasi static loading scenario. Several models were developed to understand and analyze the stress field of the structure for varying dimensions, radii, and assortment of BCs. The key findings are shown below:

Hexakis Icosahedron Analysis of Models I-V:

- Using graphene and the Carbon Nano-Tube (CNT) composite identified for this thesis, resulted in failure when building the hexakis icosahedron at 1 ft diameter with beam dimensions calculated from the set of equations in chapter II.

- The hexakis icosahedron is a more symmetrical structure and has the potential to be simulated in Abaqus Finite Element Analysis (FEA) software without the use of BCs. This can be seen in model IV which produced similar results as the model with the skin attached. The main finding was that the model without BCs was not as conservative as the models with them by as much as 33.3%.

- The frame by itself produces linear results. The skin, however, requires a non-linear analysis as it deforms non-linearly the further away from the frame it gets.

- The stresses concentrate at the vertices of the frame and are the limiting factor in the analysis of the hexakis icosahedron. Its safety factor is the closest to failing, and requires a stronger material or potential a modification to the structure.

- Unlike the icosahedron, a model of the hexakis icosahedron is feasible with present day materials that can be manufactured. The limiting factor is how large and in what manner these materials can be produced.

The last analysis focused on the air evacuation design and applying it to the hexakis icosahedron. The key findings for this analysis are summarized below:

Air Evacuation Analysis:

- Attempting to produce a model of the hexakis icosahedron air evacuation designs required a reduced model for accurate simulation. Using the 3 beam approach compared to the single beam approach, produced results with the actual stress concentration locations.

- The most conservative analysis of the air evacuation would have been to look at the 4 MP/s load rate identified in previous research to produce snap back behavior when the skin was not attached. This load rate produced velocities in the supersonic regime and another approach needed to be identified. The conservative approach of a complete vacuum with a hole to identify the velocity was the next best method.

- The buckling velocity using Dowell's equation for fluid flow through a thin flexible pipe came out to be 167,610 m/s, which is well beyond the supersonic range, but shows the maximum velocity the pipe can experience before buckling with the given materials.

- There are many air evacuation designs that could be incorporated into the hexakis icosahedron and to truly know which method is best, would require a Computational Fluid Dynamics (CFD) analysis. In terms of pure quasi static analysis of the structure, design number 2 behaved the best without producing vibrations and unknown forces within the beams.

- The air evacuation design produced maximum stresses in the structure that were 12.6% lower than the yield limit of the material. This is a successful design that could potential work, but only has a safety factor of 1.09 and could lead to failure due to manufacturing tolerances.

- Placing small holes for air evacuation resulted in minimal stress changes for the entrance to the evacuation system, but created failure points at the positions of the structure where the exit to the air evacuation system was located.

- Adding material to the exit system solved the failure point and kept the stress levels below yielding.

- Further research into the geometry of the vertex revealed interactions between the 10 beams conjoining on a single location and led to the development of a second air evacuation design and analysis.

5.0.3 Future Research

One of the key findings of this research, was the fact that the material manufacturing for this design has not been studied closely enough. A complete analysis of potential materials and the ability to additively manufacture or produce as a membrane, need to be researched. Graphene and CNT composites can each be manufactured, and the CNT composites have even showed promise in additively manufacturing as shown by Ghoshal, but the quantity needed and actual application to the structure need to be verified [35].

The overall structure that has been analyzed in Abaqus consists of wire beams, which does not allow for a true analysis of the air evacuation system with regards to the actual structure. The development of a 3 dimensional model would allow for more accurate analysis of the air evacuation system and potential payloads.

The hexakis icosahedron showed significant improvements when compared to the icosahedron. The closer to a sphere the structure gets the wider assortment of materials become available due to the increased strength and compressive load resistance. The celestial structure which was introduced by Cranston and currently being studied by K. Moore could potentially reduce the stresses in the frame and allow a smaller diameter structure with the same materials. The celestial structure is shown in figure 5.1.

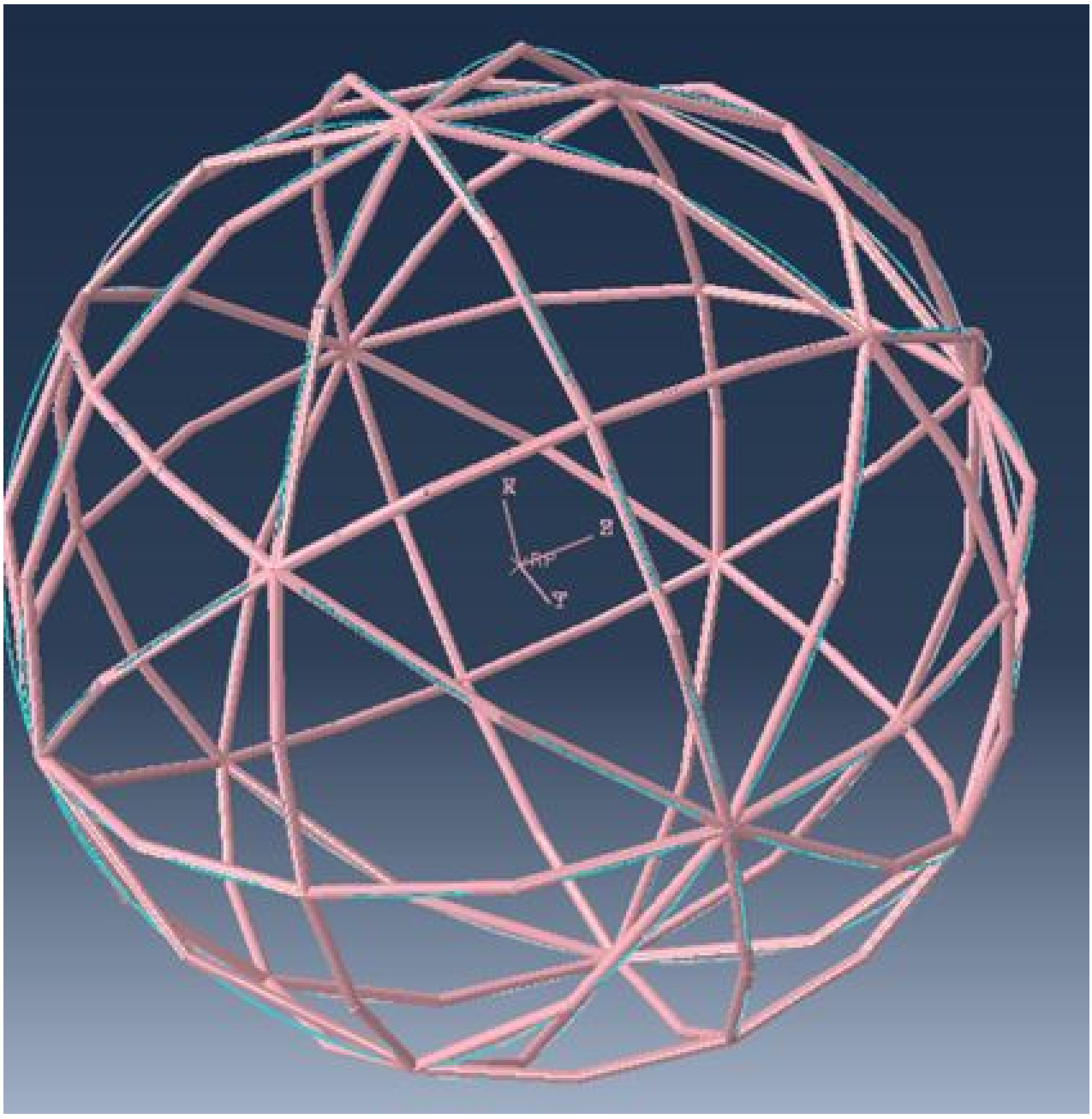

Figure 5.1. Celestial frame

Appendix A. MATLAB Explanation

The main driver for the code is the $ABAQUS\_Main.m$ MATLAB script. This script generates an .INP file and runs it through the ABAQUS terminal to generate several text documents in the folder location of the MATLAB script. The script also outputs several key findings such as the weight of the frame, the weight of the skin, the overall weight to buoyancy ratio, and a couple other parameters. This output can be seen in lines 191-196.

To generate the analysis the $ABAQUS\_Main.m$ file needs to be run. Once this is done, a .ODB file, .INP, and several results will be generated in the location of the MATLAB script. To generate the .CAE file for modification in the ABAQUS CAE, either import the .INP file or copy and paste the .INP in the command line.

To modify the MATLAB script to run the hexakis icosahedron with different parameters or materials, simply modify lines 10-15. These lines control the diameter of the beams, the thickness of the beams, the thickness of the skin, and the overall radius of the structure. The dimensions need to be entered in meters; however, the hex_{radius} needs to be entered in inches. To modify the materials being used a new matrix of the material properties needs to be created. This should be done where the other materials are stored. The order of the material properties is: density, Poisson's ratio, Young's Modulus, yield stress. The materials for the beams and the skin can then be changed in lines 124-125.

There are several other parameters in this MATLAB script that were utilized by Schwemmer in his analysis and can be described in his thesis [9].

The second script called $icosahedron\_fea\_inner.m$ was built by Adorno-Rodriquez and used in his model generation and analysis. The results for model 3 and 7 of the icosahedron were developed this way and his code and be seen and described in his thesis [5].

The last MATLAB script starting on line 650 was used by Snyder to calculate the vertex locations for the hexakis icosahedron based on a given radius of the structure. This was used in developing the FEA models of the hexakis icosahedron, but also for identifying the vertex locations for the air evacuation model that was built in SOLIDWORKS.

Appendix B. MATLAB Code

```
function [output_abaqus] = ABAQUS_Main()

% delete('*.inp','*.com','*.log','*.ipm','*.sim','*.msg',...
%        '*.rec','*.rpy','*.dat','*.sta','*.prt','*.lck','*.log'); ...
    clear f
% clc; clear all; close all
%% Static Analysis
% Last updated: Jan 17, 2018
% Edited by Castello, Anthony
% ...
    ************************************************************************
rb = 8.0000e-03; %0.000955;%
tb = 2.0000e-04; %4.77E-05;%
ts = 5.0000e-07; %1.2216E-005;%
payload = 0; %Kilograms
incr_num = 1; %used for optimization
hex_radius = 6; %meters needs to be inches
hex_alt = 0; %uses stdatmo, in feet
%% Geometry and Material Selection
% Material Selection
%       rho    nu     E           Sy    ; % Units: kg/m^3,-,Pa,Pa
% mat1 = [1870  0.3   440e9       3.73e9 ]; % UHM Unidirectional ...
    Carbon Epoxy tubes
% mat2 = [1560  0.37  303e9       5.8e9  ]; % Zylon
% mat3 = [2700  0.12  757e9       75.7e9 ]; % Diamond like Carbon, ...
    or Diamond thin film, yield aprox Y = E/10: see p1795,'Paper - ...
    Diamond like Carbon' in references
% mat4 = [2570  0.33  400e9       3.6e9  ]; % Boron Monofilament, nu ...
    guessed
```

```
mat5 = [1650  0.2   1000e9      10e9   ]; % Nanocyl NANOCYLâĎć ...
    NC7000 Thin Multi-Wall Carbon Nanotubes, nu aprox: see 'Paper - ...
    Study of Poisson Ratios of Graphene and Nanotubes' in references
% mat6 = [1844  0.18  303e9       0.4e9  ]; % Beryllium S-200, Tubing
% mat7 = [2650  0.18  379e9       1.7e9  ]; % CoorsTek Boron Carbide ...
    Reaction-Bonded Boron Carbide
% mat8 = [2800  0.33  738e9       0.14e9 ]; % Vista Metals ...
    Duramold-2âĎć Cast Aluminum Mold Plate, nu aprox
% mat9 = [247   0.33  5.76e9      0.024e9]; % 3A Composites Core ...
    Materials BALTEKÂő SB.150 Structural End-Grain Balsa, nu aprox
% mat10= [970   0.33  172e9       3.0e9  ]; % Honeywell SpectraÂő ...
    1000 Fibercl
% mat11= [1050  0.33  100e9       1.5e9  ]; % membrane laminate from ...
    cubic tech using CT155HB UHMWPE
% mat12= [1010  0.33  1.37642e11  2.28328e9]; % WHAT IS THIS?
% mat13= [970   0.33  172e9       3.0e9  ]; % enhanced membrane ...
    properties (spectra 1000 fiber)
% mat14= [970   0.33  125e9       1.75e9 ]; %estimated properties of ...
    a spectra composite (IM10 (Hexply 8552))
% mat15= [1110  0.33  2.01613e11  2.68849e9]; % WHAT IS THIS?
mat16= [1250  0.33  293e9       3.8e9  ]; %carbon nanotube composite ...
    properties from ** paper (CNT composite (NCSU))
%% Materials properties from Michael Snure, AFRL/RYDH
mat17= [2000 0.10 500e9 50e9]; %chemical vapor deposition (CVD) ...
    graphene (printed to 0.33 nm)
% mat18= [22 0.30 1e6 10e6]; %graphene aerogel - not hollow (printed ...
    to hundreds of nm)
% mat19= [3 0.30 10e6 16e3]; %silica aerogel - not hollow (printed ...
    to hundreds of nm)
%% Input
% possible values
% c_ratio_array = [.0150 .025];
```

```
% altitude_array = [0 15000];
% skin_percent_array = [0.1 0.15 0.2];

I.index = 1;
index = num2str(I.index);
I.filename = ['icosahedron',index]; % I.filename; % .py filename
% %frame material,skin material,altitude,c_ratio,skin percent,inches
% jobs = {mat16,mat13,0,.0150,0.15,6};
[rho,~,temp,press]=stdatmo(hex_alt*.3048); %ft to meters for the input
I.payload = payload;
I.scratch_folder = 'Temp Scratch Files'; % used to create the ...
    scratch folder and the enviroment .env file
% Job Info (Parallel Processing, memory allocation, use of GPUs)
I.job.num_cores = 2; % # of cores used in the analysis
I.job.memory_usage = 4*1024; %  amount of allocated memory, MB
I.job.num_GPUs = 0; % number of GPUs (graphics processing units) ...
    used, 0 for none

% Static Step Info
I.step.buckle = 0; % ON(1) / OFF(0), ON disables others
I.step.stabilization = 1; % stabilization ON(1) / OFF(0), ON ...
    w/membrane section, ON diables Riks
I.step.step_type = 0; % use Riks(1), use General(0); use General(0) ...
    w/membrane section
I.step.nonlinear_effects = 'ON'; % ON or OFF, ON w/membrane section
I.step.increment_method = 'AUTOMATIC'; % Increments (arc length if ...
    Riks) method: 'FIXED' or 'AUTOMATIC'
I.step.maxnuminc = 100; % max number of increments, if fixed
% Static Riks
I.step.initial_ArcInc = 0.1; % initial arc length
I.step.min_ArcInc = 1e-12; % minimum arc length
I.step.max_ArcInc = 1; % maximum arc length
```

```
70 I.step.max_LPF = 2; % max load proportionality factor
71 % Static General
72 I.step.initial_inc = 1e-2; % starting time increment
73 I.step.max_inc = 1; % max time increment
74 I.step.min_inc = 1e-36; % min time increment
75 I.step.stabilization_ratio = 0.05; % w/membrane only - adaptive ...
       stabilization: max stabilization/strain energy ratio, default = 0.05
76 I.step.stabilization_magn = 0.0002; % w/membrane only - dissipated ...
       energy fraction, default = 0.0002
77 % Linear Buckle
78 I.step.buck_num_Eigen   = 5;
79 I.step.buck_max_Iter    = 30;
80 I.step.buck_num_vectors = 30;
81
82 % Load
83 I.load.disp_control = 0; % displacement(1), load(0) controls
84 I.load.d = -5e3 ; % m, displacement control BC
85 I.load.P = press;%press; % Pa, sea level pressure (safety factor 1.5)
86
87 % Skin Sections
88 I.section.no_stiffness_skin = 0; % 0(no) or 1(yes); rigid skin, use ...
       surface elements
89 I.section.membrane          = 1; % membrane section (1), shell ...
       section (0)
90 % Shell Only
91 I.section.skin_section_idealization = 'NO_IDEALIZATION'; % ...
       'MEMBRANE','BENDING','NO_IDEALIZATION'
92 I.section.skin_section_location     = 'MIDDLE_SURFACE'; % ...
       'MIDDLE_SURFACE','TOP_SURFACE','BOTTOM_SURFACE'
93
94 % Tie Constraint
95 I.tie.rotations = 'OFF'; % tie rotations between skin/frame
```

```
96
97  % Mesh
98  I.mesh.skin_element_type1 = 'M3D3';%'M3D3' or 'S3'; % See 'Shell and ...
       Membrane Element Library Info.txt'
99  I.mesh.skin_element_type2 = 'M3D3';%'M3D3';
100 I.mesh.skin_element_shape = 'TRI'; % Element shape: rectangular or ...
       triangular
101 I.mesh.skin_seed_number   =  0.0065*(hex_radius/6);%0.005  ; % skin ...
       # of elements/edge, 30 edges in total
102 I.mesh.frame_element_type = 'B32'; % need to use beam element type: ...
       B31, B32, etc.
103 I.mesh.frame_seed_number  =  0.0065*(hex_radius/6);%0.005  ; % frame ...
       # of elements/edge, 30 edges in total
104 I.mesh.rays_element_type  = 'B32'; % need to use beam element type: ...
       B31, B32, etc.
105 I.mesh.rays_seed_number   =  0.0065*(hex_radius/6);%0.005  ; % rays ...
       # of elements/edge, 20 edges in total
106 I.mesh.stiff_element_type = 'B32'; % need to use beam element type: ...
       B31, B32, etc.
107 I.mesh.stiff_seed_number  =  0.0065*(hex_radius/6);%0.005  ; % rays ...
       # of elements/edge, 60 edges in total
108
109 % Parameters for W/B ratio calculation
110 I.W_B.rho    = rho; % air density at SL, kg/m^3, ...
       http://en.wikipedia.org/wiki/Density_of_air
111 I.W_B.g      = 9.81; % acceleration of gravity, m/s^2
112 % I.W_B.tot   = 0.9; % total W/B
113 % I.W_B.skin  = I.W_B.tot*(0.15);  % skin W/B ratio set value
114 % I.W_B.frame = I.W_B.tot*(1-0.15); % frame W/B ratio set value
115 % I.W_B.rays  = 0; % rays W/B ratio set value
116 % I.W_B.stiff = 0; % rays W/B ratio set value
117 I.W_B.To     = temp; % K, external temp (altitude dependent)
```

```
118 I.W_B.Ti     = I.W_B.To; % K, internal temp (altitude and heat ...
       transfer dependent)
119 I.W_B.Po     = press; % Pa, external pressure (altitude dependent)
120 % I.W_B.Po    = I.W_B.tot*press; % Pa, external pressure (altitude ...
       dependent)
121
122 %%
123 % Material Assignment
124 matf = mat16; % assigned frame material (from the selection above)
125 mats = mat17; % assigned skin  material (from the selection above)
126 matr = mat5; % assigned rays  material (from the selection above)
127 matst= mat5; % assigned stiffners  material (from the selection above)
128
129 I.materials.frame_density = matf(1); I.materials.frame_poisson   = ...
       matf(2);
130 I.materials.frame_modulus = matf(3); I.materials.frame_yield     = ...
       matf(4);
131 I.materials.skin_density  = mats(1); I.materials.skin_poisson    = ...
       mats(2);
132 I.materials.skin_modulus  = mats(3); I.materials.skin_yield      = ...
       mats(4);
133 I.materials.rays_density  = matr(1); I.materials.rays_poisson    = ...
       matr(2);
134 I.materials.rays_modulus  = matr(3); I.materials.rays_yield      = ...
       matr(4);
135 I.materials.stiff_density = matst(1); I.materials.stiff_poisson  = ...
       matst(2);
136 I.materials.stiff_modulus = matst(3); I.materials.stiff_yield    = ...
       matst(4);
137
138 % Geometry (icosahedron)
139 I.geometry.structure = 1; % 0 for icosahedron, 1 for hexakis ...
```

```
    icosahedron, 2 for celestial
I.geometry.r = hex_radius*.0254; % icosahedron radius, m; 0.1524 m = ...
    1/2 ft (input is inches)
I.geometry.hexir = 3*sqrt(5*(5+2*sqrt(5)))/5;
%     I.geometry.hexirn = ...
    (I.geometry.hexir/I.geometry.hexir)*I.geometry.r; %why the fraction?
I.geometry.hexirn = I.geometry.r;
I.geometry.rays = 0; % rays off(0), rays on(1)
I.geometry.stiff = 0; % rays off(0), rays on(1)
I.section.hollow_profile_rays = 1; % Rays beam profile: ...
    hollow(1),solid(0); beam thickness ignored if (0)
I.section.hollow_profile_stiff= 1; % Stiff beam profile: ...
    hollow(1),solid(0); beam thickness ignored if (0)
I.section.hollow_profile      = 1; % Frame beam profile: ...
    hollow(1),solid(0); beam thickness ignored if (0)
% c1 = jobs{1,4}; % frame     : if hollow circular beam, t = c*r_beam
% c2 = jobs{1,4}; % rays      : if hollow circular beam, t = c*r_beam
% c3 = jobs{1,4}; % stiffners : if hollow circular beam, t = c*r_beam
I.geometry.numpl = 3; % number of planes for the celestial configuration
I.geometry.numh = ((I.geometry.numpl+2)*2)-1;

% Assume hexakis icosahedron, hollow everything
se = (sqrt(15*(85-31*sqrt(5)))/11)*(I.geometry.hexirn/I.geometry.hexir);
me = ...
    (3*sqrt(15*(65+19*sqrt(5)))/55)*(I.geometry.hexirn/I.geometry.hexir);
le = (2*sqrt(15*(5-sqrt(5)))/5)*(I.geometry.hexirn/I.geometry.hexir);
s = .5*(se+me+le);
ta = sqrt(s*(s-se)*(s-me)*(s-le));
hexV = (180*(5+4*sqrt(5))/11)*(I.geometry.hexirn/I.geometry.hexir)^3;
I.geometry.initial_volume = hexV;
I.geometry.skin_thickness = ts;
I.geometry.skin_volume = 120*ta*I.geometry.skin_thickness;
```

```
165
166 I.geometry.frame_beam_radius    = rb; % meters
167 I.geometry.frame_beam_thickness = tb; % input
168 % I.geometry.frame_beam_radius    = ...
       sqrt((I.W_B.frame*I.W_B.rho*hexV)/...
169 %     (((pi*60*(2*c1-c1^2))*(le+me+se))*I.materials.frame_density)); ...
       % meters
170 % I.geometry.frame_beam_thickness = c1*I.geometry.frame_beam_radius; ...
       % input
171 % initialize thicknesses for first run, will need to skip after MADS ...
       takes
172 % over
173
174 %need to change how the volume is calculated if individual beams can be
175 %changed
176 I.geometry.frame_volume = ...
       (pi*60*(2*I.geometry.frame_beam_thickness*I.geometry.frame_beam_radius...
177     -I.geometry.frame_beam_thickness^2))*(le+me+se);
178
179 % I.geometry.rays_beam_radius    = ...
       I.geometry.r*sqrt(I.W_B.rays*I.W_B.rho/...
180 %     (19.82*(2*c2-c2^2)*I.materials.rays_density)); % meters
181 % I.geometry.rays_beam_thickness = c2*I.geometry.rays_beam_radius; % ...
       input
182 I.geometry.rays_beam_radius    = 0; % meters
183 I.geometry.rays_beam_thickness = 0; % input
184
185 % I.geometry.stiff_beam_radius    = ...
       I.geometry.r*sqrt(I.W_B.stiff*I.W_B.rho/...
186 %     (45.34*(2*c3-c3^2)*I.materials.stiff_density)); % meters
187 % I.geometry.stiff_beam_thickness = c3*I.geometry.stiff_beam_radius; ...
       % input
```

```
188 I.geometry.stiff_beam_radius    = 0; % meters
189 I.geometry.stiff_beam_thickness = 0; % input
190
191 % Prints set W/B
192 str1 = 'icosahedron_properties_';
193 str2 = int2str(incr_num);
194 str3 = '.txt';
195 strT = strcat(str1,str2,str3);
196 f = fopen(strT,'w');
197 % fprintf(f,'W/B skin  = %f\r\n',I.W_B.skin);
198 % fprintf(f,'W/B frame = %f\r\n',I.W_B.frame);
199 % fprintf(f,'W/B rays = %f\r\n',I.W_B.rays);
200 % fprintf(f,'W/B stiffners = %f\r\n\r\n',I.W_B.stiff);
201
202 % Prints Icosahedron Properties
203 fprintf(f,'\r\nIcosahedron\r\n');
204 fprintf(f,'-----------------------------------------------------------------\r\n\r\n');
205 fprintf(f,'Geometry:\r\n*************************************************\r\n');
206 fprintf(f,'Icosahedron Radius  : %.4f (m)\r\n',I.geometry.r);
207 fprintf(f,'Skin Thickness      : %.4e ...
       (m)\r\n',I.geometry.skin_thickness);
208 fprintf(f,'Beam radius         : %.4e ...
       (m)\r\n',I.geometry.frame_beam_radius);
209 fprintf(f,'Beam thickness      : %.4e ...
       (m)\r\n',I.geometry.frame_beam_thickness);
210 fprintf(f,'Rays radius         : %.4e ...
       (m)\r\n',I.geometry.rays_beam_radius);
211 fprintf(f,'Rays thickness      : %.4e ...
       (m)\r\n',I.geometry.rays_beam_thickness);
212 fprintf(f,'Stiffners radius    : %.4e ...
       (m)\r\n',I.geometry.stiff_beam_radius);
213 fprintf(f,'Stiffners thickness : %.4e ...
```

```
    (m)\r\n',I.geometry.stiff_beam_thickness);
fprintf(f,'Other:\r\n*********************************************************\r\n');
fprintf(f,'Payload             : %.4e (kg)\r\n',I.payload);
fprintf(f,'Altitude            : %.4e (ft)\r\n',hex_alt);

% Prints Materials Properties
fprintf(f,'\r\nFrame Material ...
    Properties:\r\n*****************************************************\r\n');
fprintf(f,'Density           : %.1f (kg/m^3)\r\n',matf(1));
fprintf(f,'Poisson ratio     : %.2f (-)\r\n' ,matf(2));
fprintf(f,'Modulus           : %.4e (Pa)\r\n',matf(3));
fprintf(f,'Yield             : %.4e (Pa)\r\n',matf(4));
fprintf(f,'\r\nSkin Material ...
    Properties:\r\n*****************************************************\r\n');
fprintf(f,'Density           : %.1f (kg/m^3)\r\n',mats(1));
fprintf(f,'Poisson ratio     : %.2f (-)\r\n' ,mats(2));
fprintf(f,'Modulus           : %.4e (Pa)\r\n',mats(3));
fprintf(f,'Yield             : %.4e (Pa)\r\n',mats(4));
% fprintf(f,'\r\nRays Material ...
    Properties:\r\n*****************************************************\r\n');
% fprintf(f,'Density           : %.1f (kg/m^3)\r\n',matr(1));
% fprintf(f,'Poisson ratio     : %.2f (-)\r\n' ,matr(2));
% fprintf(f,'Modulus           : %.4e (Pa)\r\n',matr(3));
% fprintf(f,'Yield             : %.4e (Pa)\r\n',matr(4));
% fprintf(f,'\r\nStiffners Material ...
    Properties:\r\n*****************************************************\r\n');
% fprintf(f,'Density           : %.1f (kg/m^3)\r\n',matst(1));
% fprintf(f,'Poisson ratio     : %.2f (-)\r\n' ,matst(2));
% fprintf(f,'Modulus           : %.4e (Pa)\r\n',matst(3));
% fprintf(f,'Yield             : %.4e (Pa)\r\n',matst(4));
fclose(f);

```

```
241 %% FEA Analysis
242 I.step.buckle = 0; % ON(1) / OFF(0), ON disables others
243 [~, output_abaqus]  = icosahedron_fea(I);
244 % output
245 %     .system
246 %         .status: 0 if succesful, nonzero otherwise
247 %         .cmdout: detailed message
248 %     .geometry
249 %         .vertices  : icosahedron vertices
250 %         .midpoints : edge midpoints
251 %         .facecenters: face centers
252 %     .mesh
253 %         nodes   : total # of nodes
254 %         elements: total # of elements
255 %     if buckle == 1
256 %        .buckling: frame #,eigen value:Pcrit = Po*eigen(i)
257 %     else
258 %       .inc: column of increments or load factors
259 %       .frame/skin: for each increment or load factor(i),
260 %            .U : node #, x, y, z, U1, U2, U3 (displacement)
261 %            .NF: node #, x, y, z, NF1, NF2, NF3, NF4, NF5, NF6 ...
    (nodal forces)
262 %            .S : elem #, S1, S2, S3, Mises (stresses)
263 %       .strain_energy: increment(s) or load factor, strain energy(J)
264
265 % Select Increment:
266 %i = length(O1.inc); % last increment
267
268 end
269 ================================================================================
270 % By Adorno-Rodriguez, Ruben
271 % Last updated: Jan 15, 2014
```

```
272 % Function: runs the icosahedorn FEA model
273 function [output]=icosahedron_fea_inner(I)
274 %% Input
275 % Filename
276 index = num2str(I.index);
277 filename = ['icosahedron',index]; % I.filename; % .py filename
278 filename2 = 'icosahedron';
279 model_name = [filename,'-Model'];
280 job_name = [filename,'-Job'];
281 job_name_odb = [filename,'-Job.odb'];
282 scratch_folder = I.scratch_folder; % used to create the scratch ...
       folder and the enviroment .env file
283
284 % Job Info (Parallel Processing, memory allocation, use of GPUs)
285 num_cores = I.job.num_cores; % # of cores used in the analysis
286 memory_usage = I.job.memory_usage; %  amount of allocated memory, MB
287 num_GPUs = I.job.num_GPUs; % number of GPUs (graphics processing ...
       units) used, 0 for none
288
289 % Static Step Information
290 increment_method = I.step.increment_method; % Increments (arc length ...
       if Riks) method: 'FIXED' or 'AUTOMATIC'
291 nonlinear_effects = I.step.nonlinear_effects; % ON or OFF
292 buckle = I.step.buckle; % ON(1) / OFF(0), ON disables others
293 step_type = I.step.step_type; % use Riks(1), use General(0)
294 stabilization = I.step.stabilization; % strain energy stabilization ...
       ON(1) / OFF(0), ON w/membrane section
295 % Static Riks
296 initial_ArcInc = I.step.initial_ArcInc; % initial arc length
297 min_ArcInc = I.step.min_ArcInc; % minimum arc length
298 max_ArcInc = I.step.max_ArcInc; % maximum arc length
299 max_LPF = I.step.max_LPF; % max load proportionality factor
```

```
300 % Static General
301 initial_inc = I.step.initial_inc; % starting time increment
302 max_inc = I.step.max_inc; % max time increment
303 min_inc = I.step.min_inc; % min time increment
304 maxnuminc = I.step.maxnuminc; % max number of increments
305 stabilization_ratio = I.step.stabilization_ratio; % w/membrane only ...
       - adaptive stabilization: max stabilization/strain energy ratio, ...
       default = 0.05
306 stabilization_magn = I.step.stabilization_magn; % w/membrane only - ...
       dissipated energy fraction, default = 0.0002
307 % Buckle
308 buck_num_Eigen   = I.step.buck_num_Eigen;
309 buck_max_Iter    = I.step.buck_max_Iter;
310 buck_num_vectors = I.step.buck_num_vectors;
311 if buckle == 1
312     stepname = 'Buckle';
313 elseif strcmp(nonlinear_effects,'ON') && step_type == 1
314     stepname = 'Nonlinear-Riks';
315     stabilization = 0;
316 elseif strcmp(nonlinear_effects,'ON') && step_type == 0 && ...
       stabilization == 1
317     stepname = 'Nonlinear-Static,General-wStabi';
318 elseif strcmp(nonlinear_effects,'ON') && step_type == 0 && ...
       stabilization == 0
319     stepname = 'Nonlinear-Static,General';
320 elseif strcmp(nonlinear_effects,'OFF') && step_type == 1
321     stepname = 'Linear-Riks';
322     stabilization = 0;
323 else
324     stepname = 'Linear-Static,General';
325 end
326
```

```
% Geometry
r = I.geometry.r; % icosahedron radius, meters
nr = I.geometry.hexirn/I.geometry.hexir; %meters
skin_thickness = I.geometry.skin_thickness; % meters
frame_beam_radius = I.geometry.frame_beam_radius ; % meters
frame_beam_thickness = I.geometry.frame_beam_thickness; % meters
rays_select = I.geometry.rays; % rays off(0), rays on(1)
rays_beam_radius = I.geometry.rays_beam_radius ; % meters
rays_beam_thickness = I.geometry.rays_beam_thickness; % meters
stiff_select = I.geometry.stiff; % stiffners off(0), rays on(1)
stiff_beam_radius = I.geometry.stiff_beam_radius ; % meters
stiff_beam_thickness = I.geometry.stiff_beam_thickness; % meters
%numpl = I.geometry.numpl;

% Material
frame_density = I.materials.frame_density; % kg/m^3
frame_poisson = I.materials.frame_poisson;
frame_modulus = I.materials.frame_modulus; % Pa
frame_yield   = I.materials.frame_yield; %Pa
skin_density  = I.materials.skin_density; % kg/m^3
skin_poisson  = I.materials.skin_poisson;
skin_modulus  = I.materials.skin_modulus; % Pa
skin_yield    = I.materials.skin_yield; %Pa
rays_density  = I.materials.rays_density; % kg/m^3
rays_poisson  = I.materials.rays_poisson;
rays_modulus  = I.materials.rays_modulus; % Pa
rays_yield    = I.materials.rays_yield; %Pa
stiff_density  = I.materials.stiff_density; % kg/m^3
stiff_poisson  = I.materials.stiff_poisson;
stiff_modulus  = I.materials.stiff_modulus; % Pa
stiff_yield    = I.materials.stiff_yield; %Pa

```

```
359 % Load
360 disp_control = I.load.disp_control; % displacement(1), load(0) controls
361 d = I.load.d; % m, displacement control BC
362 P = -I.load.P; % Pa, sea level pressure
363
364
365 % Frame Profile
366 hollow_profile = I.section.hollow_profile; % hollow(1),solid(0); ...
       beam thickness ignored if (0)
367 hollow_profile_rays = I.section.hollow_profile_rays; % ...
       hollow(1),solid(0); beam thickness ignored if (0)
368 hollow_profile_stiff = I.section.hollow_profile_stiff; % ...
       hollow(1),solid(0); beam thickness ignored if (0)
369
370 % Skin Sections
371 no_stiffness_skin = I.section.no_stiffness_skin;% 0(no) or 1(yes); ...
       rigid skin, use surface elements
372 membrane = I.section.membrane; % membrane section (1), shell section (0)
373 skin_section_idealization = I.section.skin_section_idealization; % ...
       MEMBRANE, BENDING or NO_IDEALIZATION
374 skin_section_location = I.section.skin_section_location; % ...
       'MIDDLE_SURFACE', 'TOP_SURFACE' or 'BOTTOM_SURFACE'
375
376 % Tie Constraint
377 rotations = I.tie.rotations; % tie rotations between skin/frame
378
379 % Mesh
380 skin_seed_number   = I.mesh.skin_seed_number  ; % size seeding
381 skin_element_type1 = I.mesh.skin_element_type1; % See 'Shell and ...
       Membrane Element Library Info.txt'
382 skin_element_type2 = I.mesh.skin_element_type2;
383 skin_element_shape = I.mesh.skin_element_shape; % Element shape: ...
```

```
    rectangular or triangular
384 frame_element_type = I.mesh.frame_element_type; % need to use beam ...
    element type: B31, B32, etc.
385 frame_seed_number  = I.mesh.frame_seed_number ; % # of ...
    elements/edge, 30 edges in total
386 rays_element_type  = I.mesh.rays_element_type; % need to use beam ...
    element type: B31, B32, etc.
387 rays_seed_number   = I.mesh.rays_seed_number ; % # of elements/edge, ...
    20 edges in total
388 stiff_element_type  = I.mesh.stiff_element_type; % need to use beam ...
    element type: B31, B32, etc.
389 stiff_seed_number   = I.mesh.stiff_seed_number ; % # of ...
    elements/edge, 60 edges in total
390
391 %% Geometry Calculations
392 % Calculates the icosahedron vertices
393 if I.geometry.structure == 0
394     p=icosahedron_coordinates(r,1);
395     c=[1 1 2,1 1 3,1 1 4,1 1 5,1 1 6,12 12 7,12 12 8,12 12 9 ,12 12 ...
        11,12 12 7 ,...
396         2  2 7 ,11 11 2,6  6  10,10 10 5,5 5  9 ,9 9 4,4 4 8,8 8 3,3 ...
            3 7,7 7 2;
397         2 3 3,3 4 4,4 5 5,5 6 6,6 2 2,7  8  8,8  9  9,9  10 10,11 10 ...
            10,7  11 11,...
398         11 7 11,2  6  6,10 11 11,5  6  6,9 10 10,4 5 5,8 9 9,3 4 4,7 ...
            8 8,2 3 3]; %connectivity array
399     %Calculates center of each face
400     k=[1 1 1 1 1 12 12 12 12 12 7 3 8 4 9 5  10 6  11 2 ;
401         2 3 4 5 6 7  8  9  10 11 2 7 3 8 4 9  5  10 2  7 ;
402         3 4 5 6 2 8  9  10 11 7  3 8 4 9 5 10 6  11 6  11];
403 elseif I.geometry.structure == 1
404     [p,c,k,c_bar2]= hexakis_coordinates(nr);
```

```
405 elseif I.geometry.structure == 2
406     [p,pl,sketch_name] = celestial_coordinates(r,numpl);
407 end
408 % Calculates the vertices in cartesian coordinates
409 if I.geometry.structure == 0 || 1
410     t=0.5; % used to select midpoint
411     for i=1:length(c) %calculates the midpoint
412         mp(i,:)=[p(c(1,i),1)+t*(p(c(2,i),1)-p(c(1,i),1)),...
413             p(c(1,i),2)+t*(p(c(2,i),2)-p(c(1,i),2)),...
414             p(c(1,i),3)+t*(p(c(2,i),3)-p(c(1,i),3))];
415     end
416
417     for i=1:length(k)
418         fc(i,:)=[mean([p(k(1,i),1) p(k(2,i),1) p(k(3,i),1)])...
419             mean([p(k(1,i),2) p(k(2,i),2) p(k(3,i),2)])...
420             mean([p(k(1,i),3) p(k(2,i),3) p(k(3,i),3)])];
421     end
422     % Calculates center between each face and each vertex
423     g = 1;
424     for j=1:length(k)
425         for i = 1:3
426             np(g,:)=[p(k(i,j),1)+t*(fc(j,1)-p(k(i,j),1)),...
427                 p(k(i,j),2)+t*(fc(j,2)-p(k(i,j),2)),...
428                 p(k(i,j),3)+t*(fc(j,3)-p(k(i,j),3))];
429             g = g + 1;
430         end
431     end
432     %Calculates the distance of each edge (to confirm coordinates ...
        accuracy)
433     for i=1:length(c)
434         edge_length(i)=sqrt((p(c(2,i),1)-p(c(1,i),1))^2+...
435             (p(c(2,i),2)-p(c(1,i),2))^2+...
```

```
436             (p(c(2,i),3)-p(c(1,i),3))^2);
437     end
438 end
439 %% Writes variables into Var.py file,which will be read by the main ...
    .py file
440 fid = fopen(['Var_',filename,'.py'],'w');
441 % Arrays
442 fprintf(fid,'p = ['); % writes vertices in a array
443 for i=1:length(p)
444     fprintf(fid,'(%0.6f,%0.6f,%0.6f),',p(i,1),p(i,2),p(i,3));
445 end
446 fprintf(fid,']');
447 fprintf(fid,'\r\n\r\n');
448 if I.geometry.structure == 0 || 1
449     fprintf(fid,'mp = ['); % writes vertices in a array
450     for i=1:length(mp)
451         fprintf(fid,'(%0.6f,%0.6f,%0.6f),',mp(i,1),mp(i,2),mp(i,3));
452     end
453     fprintf(fid,']');
454     fprintf(fid,'\r\n\r\n');
455
456     fprintf(fid,'mps = ('); % writes vertices in a array
457     for i=1:length(mp)
458         fprintf(fid,'(%0.6f,%0.6f,%0.6f,),',mp(i,1),mp(i,2),mp(i,3));
459     end
460     fprintf(fid,')');
461     fprintf(fid,'\r\n\r\n');
462
463     fprintf(fid,'c = ['); % writes wire connectivity array for the faces
464     for i=1:length(c)
465         fprintf(fid,'(%d,%d),',c(1,i),c(2,i));
466     end
```

```
467     fprintf(fid,']');
468     fprintf(fid,'\r\n\r\n');
469     if I.geometry.structure == 1
470         fprintf(fid,'c_bar2 = ['); % writes wire connectivity array
471         for i=1:length(c_bar2)
472             fprintf(fid,'(%d,%d),',c_bar2(i,1),c_bar2(i,2));
473         end
474         fprintf(fid,']');
475         fprintf(fid,'\r\n\r\n');
476     end
477     fprintf(fid,'k = ['); % writes faces connectivity array
478     for i=1:length(k)
479         fprintf(fid,'(%d,%d,%d),',k(1,i),k(2,i),k(3,i));
480     end
481     fprintf(fid,']');
482     fprintf(fid,'\r\n\r\n');
483
484     fprintf(fid,'fc = ['); % writes face center array
485     for i=1:length(k)
486         fprintf(fid,'(%0.6f,%0.6f,%0.6f),',fc(i,1),fc(i,2),fc(i,3));
487     end
488     fprintf(fid,']');
489     fprintf(fid,'\r\n\r\n');
490
491     fprintf(fid,'np = ['); % writes center between each face and ...
        each vertex
492     for i=1:length(np(:,1))
493         fprintf(fid,'(%0.6f,%0.6f,%0.6f),',np(i,1),np(i,2),np(i,3));
494     end
495     fprintf(fid,']');
496     fprintf(fid,'\r\n\r\n');
497 end
```

```
498 for i=1:length(p) %writes the vertices
499     fprintf(fid,'p%d=(%0.6f,%0.6f,%0.6f)\r\n',i,p(i,1),p(i,2),p(i,3));
500 end
501 fprintf(fid,'\r\n');
502 if I.geometry.structure == 0 || 1
503     for i=1:length(c) % writes the midpoints
504         fprintf(fid,'mp%d%d=(%0.6f,%0.6f,%0.6f)\r\n',c(1,i),c(2,i),mp(i,1),mp(i,2),mp(i,
505     end
506     if I.geometry.structure == 1
507         fprintf(fid,'mpss = ');
508         for i=1:length(c_bar2) % writes the midpoints in terms of ...
              geometric sequence
509             fprintf(fid,'(mp%d%d,),',c_bar2(i,1),c_bar2(i,2));
510         end
511     end
512     fprintf(fid,'\r\n');
513     for i=1:length(k) % writes the faces centers
514         fprintf(fid,'fc%d%d%d=(%0.6f,%0.6f,%0.6f)\r\n',k(1,i),k(2,i),k(3,i),fc(i,1),fc(
515     end
516     fprintf(fid,'\r\n');
517     fprintf(fid,'fcs = ');
518     for i=1:length(k) % writes the face centers in terms of ...
          geometric sequence
519         fprintf(fid,'(fc%d%d%d,),',k(1,i),k(2,i),k(3,i));
520     end
521 end
522 if I.geometry.structure == 2
523     fprintf(fid,'pl = ['); % writes plane angles in a array
524     for i=1:length(pl)
525         fprintf(fid,'(%0.6f),',pl(i,1));
526     end
527     fprintf(fid,']');
```

```
528     fprintf(fid,'\r\n\r\n');
529
530     fprintf(fid,'sketch_name = ['); % writes sketch name variables ...
            in a array
531     for i=1:length(sketch_name)
532         fprintf(fid,'(s%d),',sketch_name(i,1));
533     end
534     fprintf(fid,']');
535     fprintf(fid,'\r\n\r\n');
536 end
537 fprintf(fid,'\r\n');
538 fprintf(fid,'disp_control = %d\r\n',disp_control);
539 fprintf(fid,'P=%0.6f\r\n',P); % writes the pressure
540 fprintf(fid,'d=%0.6e',d); % writes the displacement control BC
541 fprintf(fid,'\r\n\r\n');
542 % Frame
543 fprintf(fid,'hollow_profile = %d\r\n',hollow_profile);
544 fprintf(fid,'frame_beam_radius = %0.6e\r\n',frame_beam_radius);
545 fprintf(fid,'frame_beam_thickness = %0.6e\r\n',frame_beam_thickness);
546 fprintf(fid,'frame_density = %0.6f\r\n',frame_density);
547 fprintf(fid,'frame_poisson = %0.6f\r\n',frame_poisson);
548 fprintf(fid,'frame_modulus = %0.6e\r\n',frame_modulus);
549 fprintf(fid,'frame_seed_number = %d\r\n',frame_seed_number);
550 fprintf(fid,'frame_element_type = %s\r\n \r\n',frame_element_type);
551 % Skin
552 fprintf(fid,'skin_thickness = %0.6e\r\n',skin_thickness);
553 fprintf(fid,'skin_density = %0.6f\r\n',skin_density);
554 fprintf(fid,'skin_poisson = %0.6f\r\n',skin_poisson);
555 fprintf(fid,'skin_modulus = %0.6e\r\n',skin_modulus);
556 fprintf(fid,'skin_seed_number = %d\r\n',skin_seed_number);
557 fprintf(fid,'skin_element_type1 = %s\r\n',skin_element_type1);
558 fprintf(fid,'skin_element_type2 = %s\r\n',skin_element_type2);
```

```
559 fprintf(fid,'skin_element_shape = %s\r\n \r\n',skin_element_shape);
560 fprintf(fid,'skin_section_idealization = ...
       %s\r\n',skin_section_idealization);
561 fprintf(fid,'skin_section_location = %s\r\n',skin_section_location);
562 fprintf(fid,'membrane = %d\r\n',membrane);
563 fprintf(fid,'no_stiffness_skin = %d\r\n \r\n',no_stiffness_skin);
564 % Rays
565 fprintf(fid,'rays_select = %d\r\n',rays_select);
566 fprintf(fid,'hollow_profile_rays = %d\r\n',hollow_profile_rays);
567 fprintf(fid,'rays_beam_radius = %0.6e\r\n',rays_beam_radius);
568 fprintf(fid,'rays_beam_thickness = %0.6e\r\n',rays_beam_thickness);
569 fprintf(fid,'rays_density = %0.6f\r\n',rays_density);
570 fprintf(fid,'rays_poisson = %0.6f\r\n',rays_poisson);
571 fprintf(fid,'rays_modulus = %0.6e\r\n',rays_modulus);
572 fprintf(fid,'rays_seed_number = %d\r\n',rays_seed_number);
573 fprintf(fid,'rays_element_type = %s\r\n \r\n',rays_element_type);
574 % Stiffners
575 fprintf(fid,'stiff_select = %d\r\n',stiff_select);
576 fprintf(fid,'hollow_profile_stiff = %d\r\n',hollow_profile_stiff);
577 fprintf(fid,'stiff_beam_radius = %0.6e\r\n',stiff_beam_radius);
578 fprintf(fid,'stiff_beam_thickness = %0.6e\r\n',stiff_beam_thickness);
579 fprintf(fid,'stiff_density = %0.6f\r\n',stiff_density);
580 fprintf(fid,'stiff_poisson = %0.6f\r\n',stiff_poisson);
581 fprintf(fid,'stiff_modulus = %0.6e\r\n',stiff_modulus);
582 fprintf(fid,'stiff_seed_number = %d\r\n',stiff_seed_number);
583 fprintf(fid,'stiff_element_type = %s\r\n \r\n',stiff_element_type);
584 % Tie Constraint
585 fprintf(fid,'rotations = %s\r\n \r\n',rotations);
586 % Model names
587 fprintf(fid,'model_name = ''%s''\r\n',model_name);
588 fprintf(fid,'job_name = ''%s''\r\n',job_name);
589 fprintf(fid,'job_name_odb = ''%s''\r\n \r\n',job_name_odb);
```

```
% Step Information
fprintf(fid,'# Step Information\r\n');
fprintf(fid,'buckle = %d\r\n',buckle);
fprintf(fid,'stabilization = %d\r\n',stabilization);
fprintf(fid,'step_type = %d\r\n',step_type);
fprintf(fid,'nonlinear_effects = %s\r\n',nonlinear_effects);
fprintf(fid,'increment_method = %s\r\n',increment_method);
fprintf(fid,'stepname = ''%s''\r\n',stepname);
fprintf(fid,'\r\n# If Buckle\r\n');
fprintf(fid,'buck_num_Eigen = %d\r\n',buck_num_Eigen);
fprintf(fid,'buck_max_Iter = %d\r\n',buck_max_Iter);
fprintf(fid,'buck_num_vectors = %d\r\n',buck_num_vectors);
fprintf(fid,'\r\n# If General\r\n');
fprintf(fid,'initial_inc = %e\r\n',initial_inc);
fprintf(fid,'max_inc = %e\r\n',max_inc);
fprintf(fid,'min_inc = %e\r\n',min_inc);
fprintf(fid,'stabilization_ratio = %0.10f\r\n',stabilization_ratio);
fprintf(fid,'stabilization_magn = %0.10f\r\n',stabilization_magn);
fprintf(fid,'\r\n# If Riks\r\n');
fprintf(fid,'initial_ArcInc = %e\r\n',initial_ArcInc);
fprintf(fid,'min_ArcInc = %e\r\n',min_ArcInc);
fprintf(fid,'max_ArcInc = %e\r\n',max_ArcInc);
fprintf(fid,'maxnuminc = %d\r\n',maxnuminc);
fprintf(fid,'max_LPF = %e\r\n \r\n',max_LPF);
% Job information
fprintf(fid,'num_cores = %d\r\n',num_cores);
fprintf(fid,'memory_usage = %d\r\n',memory_usage);
fprintf(fid,'num_GPUs = %d\r\n',num_GPUs);
% Add the path to the python code to be evaluated
f = fopen([filename2,'.py'],'r'); A = fread(f); fclose(f);
f = fopen(['python2abaqus_',filename,'.py'],'w');
fprintf(f,'path = r''%s''\r\n \r\n',pwd); % writes the current directory
```

```
622 fprintf(f,'var = ''Var_%s.py''\r\n \r\n',filename);
623 fwrite(f,A); fclose(f);
624 % Writes the environment file w/the scratch folder's directory
625 f = fopen('environment.env','r'); A = fread(f); fclose(f);
626 f = fopen('abaqus_v6.env','w');
627 fprintf(f,['scratch=''%s\\',scratch_folder,'''\r\n \r\n'],pwd); % ...
       writes the scratch directory
628 fwrite(f,A); fclose(f);
629
630 %% Runs the Adjusted Script in Abaqus
631 % warning('off','all');
632 % delete('*.inp','*.com','*.log','*.ipm','*.sim','*.msg',...
633 %        '*.rec','*.rpy','*.dat','*.sta','*.prt','*.lck','*.log'); ...
       clear f
634  warning('on','all');
635  Rmo = 'noGUI'; % No GUI, analysis runs in the background
636  mo = 'script'; % W/GUI, analysis runs with Abaqus GUI
637  [status,cmdout] = system(['abaqus cae ...
        ',Rmo,'=python2abaqus_',filename,'.py']); % runs the main script
638 %
639 fclose('all');
640 %% Output
641  output.system.status = status; % 0 if succesful, nonzero otherwise
642  output.system.cmdout = cmdout; % detailed message
643 output.geometry.vertices    = p;  % vertices
644 output.geometry.midpoints   = mp; % edge midpoints
645 output.geometry.facecenters = fc; % face centers
646 end
647 ================================================================================
648 function [XYZ,c,k,c_bar2] = hexakis_coordinates(r)
649 %Calculates the vertices of the Hexakis Icosahedron using a given ...
       radius of
```

```
650 %the structure
651 %Disdyakis Triacontahedron
652 %r = 1;
653 C0 = 3 * (15 + sqrt(5)) / 44;
654 C1 = (5 - sqrt(5)) / 2;
655 C2 = 3 * (5 + 4 * sqrt(5)) / 22;
656 C3 = 3 * (5 + sqrt(5)) / 10;
657 C4 = sqrt(5);
658 C5 = (75 + 27 * sqrt(5)) / 44;
659 C6 = (15 + 9 * sqrt(5)) / 10;
660 C7 = (5 + sqrt(5)) / 2;
661 C8 = 3 * (5 + 4 * sqrt(5)) / 11;
662
663 V0  = [0.0, 0.0,  C8];
664 V1  = [0.0, 0.0, -C8];
665 V2  = [ C8, 0.0, 0.0];
666 V3  = [-C8, 0.0, 0.0];
667 V4  = [0.0,  C8, 0.0];
668 V5  = [0.0, -C8, 0.0];
669 V6  = [0.0,  C1,  C7];
670 V7  = [0.0,  C1, -C7];
671 V8  = [0.0, -C1,  C7];
672 V9  = [0.0, -C1, -C7];
673 V10 = [ C7, 0.0,  C1];
674 V11 = [ C7, 0.0, -C1];
675 V12 = [-C7, 0.0,  C1];
676 V13 = [-C7, 0.0, -C1];
677 V14 = [ C1,  C7, 0.0];
678 V15 = [ C1, -C7, 0.0];
679 V16 = [-C1,  C7, 0.0];
680 V17 = [-C1, -C7, 0.0];
681 V18 = [ C3, 0.0,  C6];
```

```
682 V19 = [ C3, 0.0, -C6];
683 V20 = [-C3, 0.0,  C6];
684 V21 = [-C3, 0.0, -C6];
685 V22 = [ C6,  C3, 0.0];
686 V23 = [ C6, -C3, 0.0];
687 V24 = [-C6,  C3, 0.0];
688 V25 = [-C6, -C3, 0.0];
689 V26 = [0.0,  C6,  C3];
690 V27 = [0.0,  C6, -C3];
691 V28 = [0.0, -C6,  C3];
692 V29 = [0.0, -C6, -C3];
693 V30 = [ C0,  C2,  C5];
694 V31 = [ C0,  C2, -C5];
695 V32 = [ C0, -C2,  C5];
696 V33 = [ C0, -C2, -C5];
697 V34 = [-C0,  C2,  C5];
698 V35 = [-C0,  C2, -C5];
699 V36 = [-C0, -C2,  C5];
700 V37 = [-C0, -C2, -C5];
701 V38 = [ C5,  C0,  C2];
702 V39 = [ C5,  C0, -C2];
703 V40 = [ C5, -C0,  C2];
704 V41 = [ C5, -C0, -C2];
705 V42 = [-C5,  C0,  C2];
706 V43 = [-C5,  C0, -C2];
707 V44 = [-C5, -C0,  C2];
708 V45 = [-C5, -C0, -C2];
709 V46 = [ C2,  C5,  C0];
710 V47 = [ C2,  C5, -C0];
711 V48 = [ C2, -C5,  C0];
712 V49 = [ C2, -C5, -C0];
713 V50 = [-C2,  C5,  C0];
```

```
714 V51 = [-C2,  C5, -C0];
715 V52 = [-C2, -C5,  C0];
716 V53 = [-C2, -C5, -C0];
717 V54 = [ C4,  C4,  C4];
718 V55 = [ C4,  C4, -C4];
719 V56 = [ C4, -C4,  C4];
720 V57 = [ C4, -C4, -C4];
721 V58 = [-C4,  C4,  C4];
722 V59 = [-C4,  C4, -C4];
723 V60 = [-C4, -C4,  C4];
724 V61 = [-C4, -C4, -C4];
725
726 for i = 0:61
727     j = i +1;
728     p(j,:)=r.*eval(['V' num2str(i)]);
729 end
730 XYZ = p;
731
732 f = [18,  0,  8 ...,
733     18,  8, 32 ...,
734     18, 32, 56 ...,
735     18, 56, 40 ...,
736     18, 40, 10 ...,
737     18, 10, 38 ...,
738     18, 38, 54 ...,
739     18, 54, 30 ...,
740     18, 30,  6 ...,
741     18,  6,  0 ...,
742     19,  1,  7 ...,
743     19,  7, 31 ...,
744     19, 31, 55 ...,
745     19, 55, 39 ...,
```

```
746      19, 39, 11 ...,
747      19, 11, 41 ...,
748      19, 41, 57 ...,
749      19, 57, 33 ...,
750      19, 33,  9 ...,
751      19,  9,  1 ...,
752      20,  0,  6 ...,
753      20,  6, 34 ...,
754      20, 34, 58 ...,
755      20, 58, 42 ...,
756      20, 42, 12 ...,
757      20, 12, 44 ...,
758      20, 44, 60 ...,
759      20, 60, 36 ...,
760      20, 36,  8 ...,
761      20,  8,  0 ...,
762      21,  1,  9 ...,
763      21,  9, 37 ...,
764      21, 37, 61 ...,
765      21, 61, 45 ...,
766      21, 45, 13 ...,
767      21, 13, 43 ...,
768      21, 43, 59 ...,
769      21, 59, 35 ...,
770      21, 35,  7 ...,
771      21,  7,  1 ...,
772      22,  2, 11 ...,
773      22, 11, 39 ...,
774      22, 39, 55 ...,
775      22, 55, 47 ...,
776      22, 47, 14 ...,
777      22, 14, 46 ...,
```

```
778      22, 46, 54 ...,
779      22, 54, 38 ...,
780      22, 38, 10 ...,
781      22, 10,  2 ...,
782      23,  2, 10 ...,
783      23, 10, 40 ...,
784      23, 40, 56 ...,
785      23, 56, 48 ...,
786      23, 48, 15 ...,
787      23, 15, 49 ...,
788      23, 49, 57 ...,
789      23, 57, 41 ...,
790      23, 41, 11 ...,
791      23, 11,  2 ...,
792      24,  3, 12 ...,
793      24, 12, 42 ...,
794      24, 42, 58 ...,
795      24, 58, 50 ...,
796      24, 50, 16 ...,
797      24, 16, 51 ...,
798      24, 51, 59 ...,
799      24, 59, 43 ...,
800      24, 43, 13 ...,
801      24, 13,  3 ...,
802      25,  3, 13 ...,
803      25, 13, 45 ...,
804      25, 45, 61 ...,
805      25, 61, 53 ...,
806      25, 53, 17 ...,
807      25, 17, 52 ...,
808      25, 52, 60 ...,
809      25, 60, 44 ...,
```

```
      25, 44, 12 ...,
      25, 12,  3 ...,
      26,  4, 16 ...,
      26, 16, 50 ...,
      26, 50, 58 ...,
      26, 58, 34 ...,
      26, 34,  6 ...,
      26,  6, 30 ...,
      26, 30, 54 ...,
      26, 54, 46 ...,
      26, 46, 14 ...,
      26, 14,  4 ...,
      27,  4, 14 ...,
      27, 14, 47 ...,
      27, 47, 55 ...,
      27, 55, 31 ...,
      27, 31,  7 ...,
      27,  7, 35 ...,
      27, 35, 59 ...,
      27, 59, 51 ...,
      27, 51, 16 ...,
      27, 16,  4 ...,
      28,  5, 15 ...,
      28, 15, 48 ...,
      28, 48, 56 ...,
      28, 56, 32 ...,
      28, 32,  8 ...,
      28,  8, 36 ...,
      28, 36, 60 ...,
      28, 60, 52 ...,
      28, 52, 17 ...,
      28, 17,  5 ...,
```

```
842      29,  5, 17 ...,
843      29, 17, 53 ...,
844      29, 53, 61 ...,
845      29, 61, 37 ...,
846      29, 37,  9 ...,
847      29,  9, 33 ...,
848      29, 33, 57 ...,
849      29, 57, 49 ...,
850      29, 49, 15 ...,
851      29, 15,  5];
852 f = f+1;
853 j = 1;
854 for i = 1:length(f)/3
855     c(j:j+2,:) = [f(j),f(j+1);f(j),f(j+2);f(j+1),f(j+2)];
856     j = j+3;
857 end
858 c = c';
859 c_bar2 = unique(c','rows');
860 %c_bar = unique(c','rows','stable');
861 j = 170;
862 for i = 1:24
863     remove(i) = j;
864     j = j+2;
865 end
866 c_bar2([1:12,14:15,17:18,20:21,23:24,26:27,29:30,32:33,35:36,38:39,41:42,44:45,47:48,re
       = [];
867 j = 1;
868 for i = 1:120
869     k(i,:) = [f(j),f(j+1),f(j+2)];
870     j = j+3;
871 end
872 k = k';
```

```
873 end
```

Appendix C. Abaqus CAE Tutorials

Figure C.1 demonstrates the application of the coupling constraint to the reference point and the triangular face.

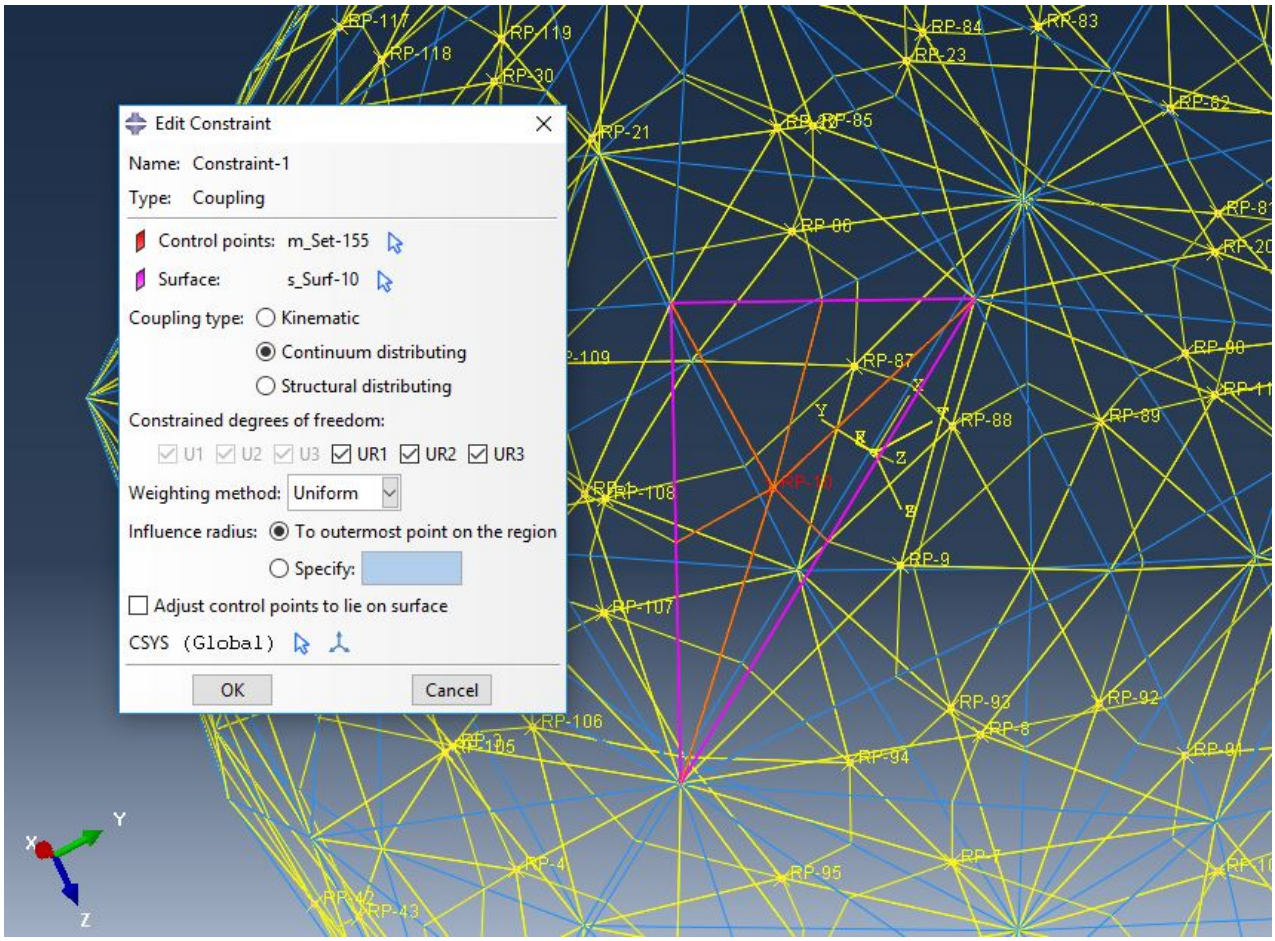

Figure C.1. Reference point technique coupling constraint options in Abaqus CAE

Figure C.2 demonstrates the method for applying the concentrated load in the reference point technique towards the center of the structure by using a spherical coordinate system with the origin at the center.

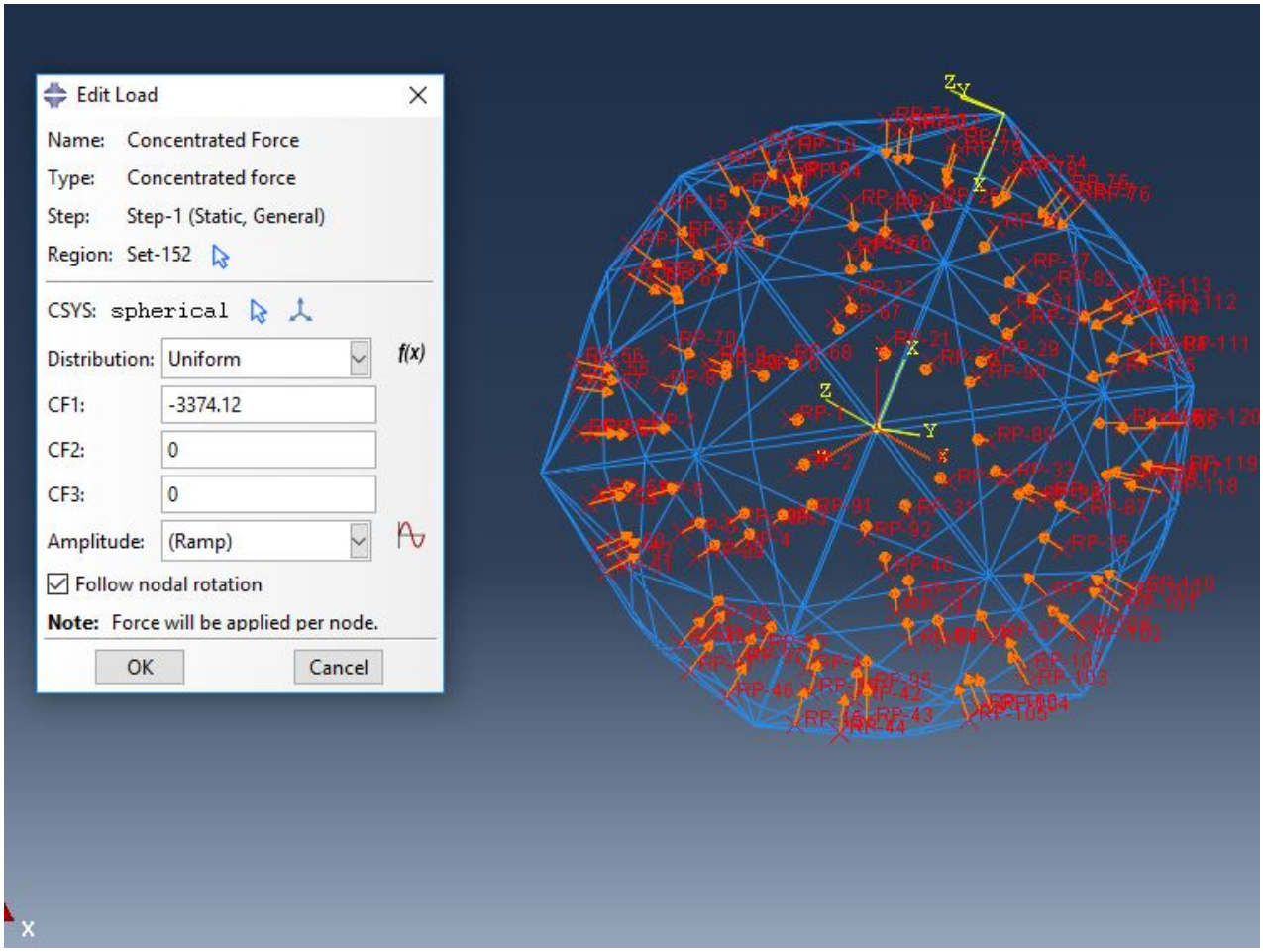

Figure C.2. Reference point technique applying concentrated load towards center of the structure, options in Abaqus CAE

Figure C.3 depicts the Abaqus CAE menu for applying the non-linear geometry analysis and the energy dissipation fraction parameters.

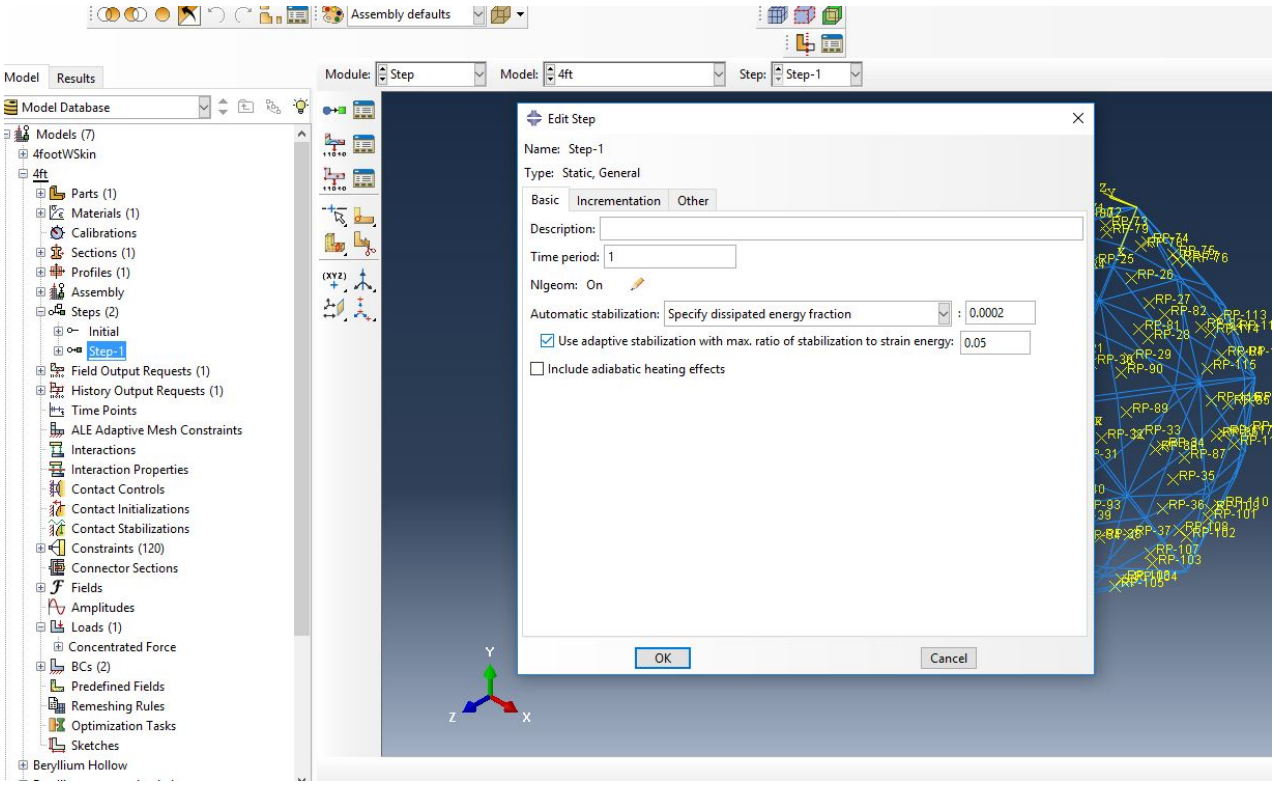

Figure C.3. Utilizing non-linear geometry options in Abaqus CAE

Figure C.4 depicts the options required to utilize the total force option when applying a pressure load to a 3D model in the Abaqus CAE.

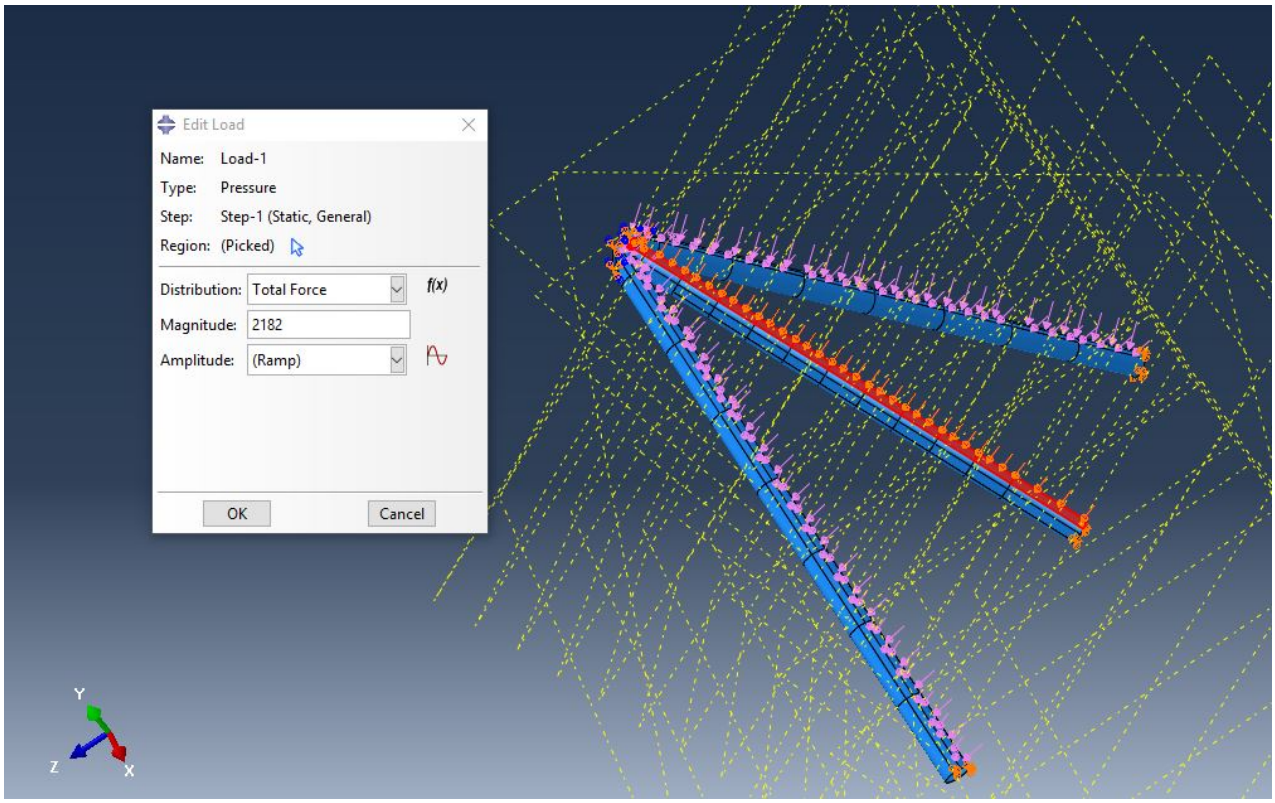

Figure C.4. Applying pressure load in 3D model with total force options in Abaqus CAE

Bibliography

[1] Archimedes principle and buoyancy. [Online]. Available: https://sites.google.com/site/physicsofdiving/diving-gas-laws/buoyancy-and-archimedes-principle

[2] B. Cranston, M. AlGhofaily, and A. Palazotto, "Design and structural analysis of unique structures under an internal vacuum," *Aerospace Science and Technology*, vol. 68, pp. 68–76, 2017.

[3] H. Soffar, "Steady flow, turbulent flow and applications on the continuity equation," Nov 2017. [Online]. Available: https://www.online-sciences.com/physics/steady-flow-turbulent-flow-and-applications-on-the-continuity-equation/

[4] A. Castello and A. Palazotto, "Structural analysis of the hexakis icosahedron lighter than air vehicle and the air evacuation system," *2018 AIAA/ASCE/AHS/ASC Structures, Structural Dynamics, and Materials Conference*, Jan 2018. [Online]. Available: https://doi.org/10.2514/6.2018-1994

[5] R. Adorno-Rodriguez, "Nonlinear structural analysis of an icosahedron and its application to lighter than air vehicles under a vacuum," Master's thesis, Air Force Institute of Technology, Wright Patterson AFB, Ohio, 2014.

[6] L. W. Just, "Dynamic response analysis of an icosahedron shaped lighter than air vehicle," Master's thesis, Air Force Institute of Technology, Wright Patterson AFB, Ohio, 2015.

[7] B. C. Cranston, "Conceptual design, structural analysis, and design space exploration of a vacuum lighter than air vehicle," PhD Dissertation, Air Force Institute of Technology, 2950 Hobson Way, WPAFB, OH 45433-7765, Mar 2016.

[8] J. W. Snyder, "A study of quasi-static and dynamic analyses of a hexakis icosahedron frame for use in a vacuum lighter-than-air vehicle," Master's thesis, Air Force Institute of Technology, Wright Patterson AFB, Ohio, 2017.

[9] J. R. Schwemmer, "Optimal design of a hexakis icosahedron vacuum based lighter than air vehicle," Master's thesis, Air Force Institute of Technology, Wright Patterson AFB, Ohio, 2017.

[10] X. W. et al, "Ultra strong, stiff and multi functional carbon nanotube composites," *Materials Research Letters*, pp. 19–25, 2013.

[11] C. Lee, X. Wei, J. W. Kysar, and J. Hone, "Measurement of the Elastic Properties and Intrinsic Strength of Monolayer Graphene," *Science*, vol. 321, no. July, pp. 385–388, 2008.

[12] Y. Deng and P. Wang, "Ancient chinese inventions," *China Intercontinental Press*, p. 113, 2005.

[13] L. Winter and G. Degner, *Minute Epics of Flight*. New York, NY: Grosset and Dunlap, 1933.

[14] L. Ege, *Balloons and airships*. Macmillan, 1974.

[15] Archimedes' principle. [Online]. Available: http://hyperphysics.phy-astr.gsu.edu/hbase/pbuoy.html

[16] Hindenburg: The untold story. [Online]. Available: http://www.smithsonianchannel.com/shows/hindenburg-the-untold-story

[17] A. Akhmeteli and A. Gavrilin, "Layered shell vacuum balloons," Feb. 23 2006, uS Patent App. 11/127,613. [Online]. Available: http://www.google.com/patents/US20060038062

[18] T. T. Metlen, "Design of a lighter than air vehicle that achieves positive buoyancy in air using a vacuum," Master's thesis, Air Force Institute of Technology, Wright Patterson AFB, Ohio, 2012.

[19] T. Metlen and A. N. Palazotto, "Design of a structure that achieves positive buoyancy in air using a vacuum," *57th AIAA/ASCE/AHS/ASC Structures, Structural Dynamics and Materials Conference*, 2013. [Online]. Available: https://www.researchgate.net/publication/268458130_Design_of_a_Structure_that_Achieves_Positive_Buoyancy_in_Air_Using_a_Vacuum

[20] Global hawk. [Online]. Available: http://www.northropgrumman.com/Capabilities/GlobalHawk/Pages/default.aspx

[21] *Abaqus Analysis User's Manual*, Dassault Systémes, 2014.

[22] J. J. Anderson, *Fundamentals of Aerodynamics*. New York, NY: McGraw-Hill, 2011.

[23] K. Avila, D. Moxey, A. de Lozar, and M. Avila, "The onset of turbulence in pipe flow," *Science*, vol. 333, pp. 192–196, 2011.

[24] R. Cook, D. Malkus, M. Plesha, and R. Witt, *Concepts and Applications of Finite Element Analysis*. Danvers, MA: John Wiley and Sons, 2002.

[25] A. S. Saada, *Elasticity: Theory and Applications*. Fort Lauderdale, FL: J. Ross Publishing, Inc., 2009.

[26] E. H. Dowell and R. N. Clark, *A Modern Course in Aeroelasticity*. Kluwer Academic Publishers, 2004.

[27] R. Adorno-Rodriguez and A. N. Palazotto, "Nonlinear structural analysis of an icosahedron under an internal vacuum," *57th AIAA/ASCE/AHS/ASC*

Structures, Structural Dynamics and Materials Conference, pp. 878–883, 2015. [Online]. Available: http://dx.doi.org/10.2514/1.C033284

[28] L. Just and A. N. Palazotto, "The evaluation of an icosahedron' eigenvalue," *57th AIAA/ASCE/AHS/ASC Structures, Structural Dynamics and Materials Conference*, 2016. [Online]. Available: http://dx.doi.org/10.2514/6.2016-0202

[29] E. Catalan, "MÃľmoire sur la thÃľorie des polyÃĺdres," *Journal de l'ÃĽcole polytechnique*, vol. 41, pp. 1–71, 1865.

[30] J. Snyder and A. N. Palazotto, "A study of quasi-static and dynamic analyses of a hexakis icosahedron frame for use in a vacuum lighter-than-air vehicle," *58th AIAA/ASCE/AHS/ASC Structures, Structural Dynamics and Materials Conference*, pp. 1–12, 2017. [Online]. Available: https://doi.org/10.2514/6.2017-1596

[31] "Optimal design of a hexakis icosahedron vacuum based lighter than air vehicle," *2018 AIAA/ASCE/AHS/ASC Structures, Structural Dynamics, and Materials Conference*, 2018.

[32] W. D. Pilkey, *Formulas for Stress, Strain, and Structural Matricies*. John Wiley & Sons, Inc., 1994.

[33] R. Fitzpatrick, "Flow through an orifice," Jan 2016. [Online]. Available: https://farside.ph.utexas.edu/teaching/336L/Fluid/node55.html

[34] McNally, "Approximate flow through an orifice," Nov 2017. [Online]. Available: http://www.mcnallyinstitute.com/13-html/13-12.htm

[35] S. Ghoshal, "Polymer/carbon nanotubes (cnt) nanocomposites processing using additive manufacturing (three-dimensional printing) technique: An overview," *fibers*, vol. 40, pp. 1–15, 2017.

REPORT DOCUMENTATION PAGE

Form Approved
OMB No. 0704–0188

1. REPORT DATE *(DD–MM–YYYY)*	2. REPORT TYPE	3. DATES COVERED *(From — To)*
22 Mar 2018	Master's Thesis	August 2017 — March 2018

4. TITLE AND SUBTITLE

A STUDY OF THE HEXAKIS ICOSAHEDRON VACUUM LIGHTER THAN AIR VEHICLE AND THE EFFECTS OF AIR EVACUATION ON THE STRUCTURAL INTEGRITY

5a. CONTRACT NUMBER

5b. GRANT NUMBER

5c. PROGRAM ELEMENT NUMBER

6. AUTHOR(S)

Castello, Anthony, A. , Captain

5d. PROJECT NUMBER

JON 18Y246

5e. TASK NUMBER

5f. WORK UNIT NUMBER

7. PERFORMING ORGANIZATION NAME(S) AND ADDRESS(ES)

Air Force Institute of Technology
Graduate School of Engineering and Management (AFIT/EN)
2950 Hobson Way
WPAFB OH 45433-7765

8. PERFORMING ORGANIZATION REPORT NUMBER

AFIT-ENY-MS-18-M-246

9. SPONSORING / MONITORING AGENCY NAME(S) AND ADDRESS(ES)

AFOSR/RTA
Att: Dr. Jaimie Tiley
875 N. Randolph Street
Suite 325, Room 3112
Arlington VA, 22203-1768
703-588-8316

10. SPONSOR/MONITOR'S ACRONYM(S)

AFOSR/RTA

11. SPONSOR/MONITOR'S REPORT NUMBER(S)

12. DISTRIBUTION / AVAILABILITY STATEMENT

DISTRIBUTION STATEMENT A:
APPROVED FOR PUBLIC RELEASE; DISTRIBUTION UNLIMITED.

13. SUPPLEMENTARY NOTES

14. ABSTRACT

This research continued the work of Lt. Schwemmer and Lt. Snyder studying the potential use of an internal frame to manufacture a lighter than air vehicle, which utilizes an internal vacuum to produce buoyancy. In specific, this thesis researches the hexakis icosahedron under a quasi-static load at sea level pressure in order to design, model, and evaluate an air evacuation system. The hexakis icosahedron was first compared to the icosahedron to fully understand the benefits of the two systems, at which point the hexakis icosahedron was modeled in a finite element analysis software to conduct an in-depth study of the stress fields, and finally two separate finite element models were built to analyze different air evacuation methods and their effects on the structure.

15. SUBJECT TERMS

Structures, Lighter Than Air Vehicles

16. SECURITY CLASSIFICATION OF:			17. LIMITATION OF ABSTRACT	18. NUMBER OF PAGES	19a. NAME OF RESPONSIBLE PERSON
a. REPORT	b. ABSTRACT	c. THIS PAGE			Dr. A. Palazotto, AFIT/ENY
U	U	U	UU	175	19b. TELEPHONE NUMBER *(include area code)* (937) 255-3636 x4599; anthony.palazotto@afit.edu